

## ABSTRACT

Title of Dissertation: DEVELOPMENT OF THE COLD ATOM  
VACUUM STANDARD

Julia Scherschligt, Doctor of Philosophy, 2023

Dissertation directed by: Adjunct Professor Trey Porto, Physics

We describe the inception, design, development, and initial results of The Cold Atom Vacuum Standard (CAVS). It has been known for many years that vacuum level limits the lifetime of a cold atom cloud; we invert this to create a vacuum pressure measurement tool based on the trapped cloud lifetime. The difference between a standard and a sensor is of great concern to metrologists: a primary standard defines a unit, and a sensor transduces it. To have a device capable of both functions is to have a calibration-free measurement tool, which is of interest to many stakeholders in academia, industry, and defense. We describe all aspects of construction of the CAVS, including a lengthy investigation of vacuum technology. We ultimately demonstrate that the device is traceable to pressure through the fundamental physics of collision cross sections, thereby elevating it to status as not just a sensor, but a standard.

# DEVELOPMENT OF THE COLD ATOM VACUUM STANDARD

by

Julia Scherschligt

Dissertation submitted to the Faculty of the Graduate School of the  
University of Maryland, College Park, in partial fulfillment  
of the requirements for the degree of  
Doctor of Philosophy  
2023

Professor Steven Rolston, Chair  
Adjunct Professor Trey Porto  
Professor Amy Mullin  
Professor Christopher Lobb  
Dr. David Baxter

Not subject to U.S. Copyright  
Julia Scherschligt  
National Institute of Standards and Technology  
2023

## Preface

Measurement science, or metrology, is concerned with the realization and dissemination of measurement units, specifically those of the *Système International* (SI). This has been a crucial element of organized economies since the beginning, dating all the way back to the development of monetary systems in ancient Sumer. If one were to exchange say, wheat for a goat, one would need an impartial way to verify the trade was fair, that the goat was of sufficient size, and that the quantity of wheat was up to standard. And so metrology was born. In modern times we face the same challenges, but these have become progressively more nuanced and sophisticated. As recently as a hundred years ago, all measurements were traced through successive comparisons back to a single artifact that served to define a unit. For instance, the singular standard meter and the standard kilogram were a bar and a cylinder, respectively, of platinum iridium housed in vaults at the International Bureau of Weights and Measures (BIPM) just outside Paris. This artifact-based metrology had a number of serious shortcomings, chiefly aggregation of uncertainty. In practice, an end user of some measuring device performs verification against a laboratory standard, which is in turn calibrated by comparison to secondary standard artifact at a commercial lab, which is compared to a so-called transfer standard by that same calibration lab. That transfer standard would be calibrated by a National Metrology Institute (NMI) against a working artifact standard, that is compared to a primary artifact standard, which would be compared to a working standard at the BIPM, which would ultimately be compared against the singular artifact that defines the unit. This is called the traceability chain, and though the details can vary widely, at each step

in the chain some new uncertainty is accumulated. This aggregated calibration uncertainty can be hundreds of times larger than the theoretical uncertainty possible for a device. Moreover, this process represents significant time and expense. But artifact-based metrology has an even more insidious problem – the singular defining artifact can itself change. This doesn't have as many consequences for the industrial user, because the changes tend to be very small, but it has dire consequences for science at the cutting edge.

With the advent of modern physics, a new approach to metrology began to take shape. It was now possible to define the units in the SI through physical properties of materials or fundamental constants of nature. Now, instead of a bar of platinum iridium, the meter is defined by the speed of light in vacuum. This of course depends on a robust definition of the second, which is now defined by transitions in the cesium atom. With the exception of Avogadro's number, all of the fundamental units are interdependent in this way. The last of the artifact standards was the International Prototype Kilogram, officially replaced by the Kibble Balance in 2019 which defines mass in terms of electrical current and voltage. This shift in paradigm, away from artifact-based standards toward physics-based standards, solves the problem of artifact drift, but does not by itself solve the problems inherent in a long traceability chain. Now NMIs and some secondary calibration labs have direct access to the SI through devices like the Kibble balance, but for the most part their customers still compare artifacts. There is one notable exception to this general trend, the SI unit of time. The technology to realize the second through clock transitions in the cesium atom has been sufficiently developed that industrial end-users can realistically have their own atomic clocks. These deployable commercial atomic

clocks don't match the performance of the best laboratory-based standards, but they're more than adequate for all but the most demanding applications.

The National Institute of Standards and Technology (NIST) and other NMIs around the world have undertaken a commitment to develop similar deployable physics-based standards for all of the fundamental and derived SI units, this has been dubbed the "Quantum-SI." Key elements to this vision correlate with the redefinition of the SI in 2019. Under the redefined SI, the base units are tied to fundamental physical constants rather than an artifact or specific method of realization. Therefore, primary standards may be created using a variety of techniques. NMIs or other calibration labs may create primary standards suited to their financial and uncertainty budget requirements.

In practice, a laboratory-based system is built and optimized to have the lowest uncertainty. It is permanently installed and used for the calibration of transfer standards. But the advantages of the Quantum-SI are not confined to the NMI. Portable devices have clear advantages over traditional transfer standards. First, such devices never need to be returned to an NMI for recalibration. Second, though the physics that underpins a Quantum-SI device is absolute, its interrogation will still have some associated uncertainty, but these uncertainties will be well defined and quantitatively understood.

The purpose of this thesis is to describe a new technique that we have developed for pressure metrology in the vacuum. Indeed the measurement science in realizing and disseminating the SI unit for pressure the pascal (Pa), has been the subject of much interest at NIST for decades, so we begin with a review of this research. Modern optical-based techniques for pascal metrology have been investigated, including multi-photon ionization and cavity ringdown spectroscopy. And more recently of course, the work to

recast the pascal in terms of quantum properties and fundamental constants and in so doing, make vacuum metrology consistent with the global trend toward quantum-based metrology. NIST has ongoing projects that interrogate the index of refraction of a gas using an optical cavity for low vacuum, and count background particles in high vacuum to extreme high vacuum using trapped laser-cooled atoms in the Cold Atom Vacuum Standard (CAVS), the latter is the main subject of this thesis.

As a final note, it is essential that I discuss my role in the overall project. A thesis usually emphasizes the particular contributions of its author, and this one is no different. The nature of those contributions, however, is quite unusual compared to an ordinary graduate student. As a mid-career physicist, with an established program and reputation as a vacuum metrologist, I am the PI of this project. As a result, this thesis necessarily documents the work done by a team under my leadership. My early contributions included a deep review of existing technology (see Chapter 3: developing the idea for the CAVS and seriously examining its feasibility (see Chapter 5:), writing proposals, and delivering pitches for funding. Ultimately successful, I recruited the core members of the team to develop the atomic, molecular, and optical (AMO) physics side of the experiment. I make no claim to any expertise in the realm of AMO physics, and indeed my naiveté was an asset in certain cases, most notably to put a hole in the pCAVS chip for back-loading. In addition to my management role, I helped build the AMO side of the experiment, and helped collecting and analyzing cross section data. The bulk of my original technical contributions were on the vacuum side of the experiment (all of Chapter 4: and parts of Chapter 6:). Parts of this project in which I played a lesser role are

shorter in reflection of this fact (the exception to this is the rather short results chapter), and technical detail that was developed by others is either omitted or noted as such.



## Acknowledgements

Thanks to Jim Fedchak for being the colleague and mentor I so badly needed, Steve Eckel and Dan Barker for their patient teaching, Jerry Fraser, Steve Rolston, and Gretchen Campbell for going along with this harebrained idea, and Trey Porto for advice, support, and encouragement, of which I required no small amount. Thanks to Amy Mullin and Chris Lobb who had the grace to serve as committee members without ever having so much as heard of me. Thanks to Dave Baxter for not giving up on me after all these years. Most of all, thanks to Dan Hussey without whom I would never have gone back.

## Table of Contents

Preface.....	ii
Acknowledgements.....	vii
Table of Contents.....	viii
List of Tables .....	x
List of Figures .....	xii
List of Abbreviations .....	xviii
Chapter 1: Introduction.....	1
Chapter 2: Traditional Pressure Metrology .....	7
Chapter 3: Overview of Modern Approaches to Pressure Metrology .....	12
3.1 Resonant-enhanced multi-photon ionization .....	12
3.2 Cavity ring-down spectroscopy .....	13
3.3 SiN Ring-Down Membrane Gauge (the “brane” gauge) .....	15
3.4 Spectroscopic Technique for Measurement of Transient Pressure.....	18
3.5 Refractometry for Pressure Metrology .....	20
3.6 Practical use of refractometers as pressure standards .....	22
3.7 Making refractometry-based vacuum standards primary .....	26
3.8 Introduction to the Cold Atom Vacuum Standard .....	30
Chapter 4: Vacuum Preparation.....	32
4.1 Principles of outgassing .....	32
4.2 Baking in air versus vacuum.....	37
4.3 Experiment details – chambers and treatments.....	39
4.4 Experiment details – measurement apparatus and method.....	41
4.5 Experiment details – determining the volumes.....	43
4.6 Baking in air versus vacuum – results .....	44
4.7 Vacuum oven for baking.....	46
4.8 Construction of the Vacuum oven .....	47
4.9 Operating the oven.....	54
4.10 Investigation of materials in conjunction with heat treatments for vacuum .....	55
4.11 Materials for Vacuum: Experiment .....	58

4.11.1 Materials for Vacuum: Outgassing Apparatus.....	60
4.11.2 Materials for Vacuum: Results for water outgassing.....	67
4.11.3 Materials for Vacuum: Results for Hydrogen Outgassing.....	70
4.11.4 Materials for Vacuum: Summary.....	73
Chapter 5: Overview of the CAVS.....	75
5.1 Fundamentals of Laser Cooling and Trapping.....	76
5.2 Estimating the loss rate coefficient.....	79
5.3 Other loss mechanisms and error sources in the CAVS .....	81
Chapter 6: CAVS Experimental Design Details.....	86
6.1 CAVS Design.....	86
6.2 Magnetic Field System .....	89
6.3 Atom Loading .....	94
6.4 Atom Loading via a 3D printed effusive source .....	95
6.5 Atom Loading via Light-Induced Atomic Desorption.....	100
6.6 Dynamic Expansion Chamber to produce known pressure .....	104
6.7 Flowmeter for Gas Injection .....	115
6.8 Stability of Bakeable CDGs.....	119
Chapter 7: Beyond the laboratory-scale CAVS.....	128
7.1 Advantages and challenges of a portable CAVS .....	128
7.2 A closer look at systematics.....	131
7.3 Fast Operation – the MOT as pressure sensor .....	133
7.4 Accurate Operation – the magnetic trap as pressure sensor .....	136
7.5 Direct comparison of two prototype pCAVS.....	138
Chapter 8: Measurement of loss rate coefficient and comparison to theory .....	146
8.1 Brief Review of Analysis.....	146
8.2 Procedure and results .....	148
8.3 Closing remarks .....	153
Bibliography .....	156

## List of Tables

Table I: Consensus values for best-possible calibration uncertainties for traditional gauges covering all accessible vacuum pressures.....	10
Table II: The calculated time needed to reduce the hydrogen concentration in 304 stainless steel by 99%. Various thicknesses of steel are given in the table, corresponding to those commonly used in vacuum chamber construction. The flange designations are defined in the standard document ISO 3669 (International Organization for Standardization). .....	36
Table III. The measured volumes of the apparatus and sample chamber. ....	44
Table IV: Outgassing rates of the four sample chambers. Prior to the outgassing measurements, all of the sample chambers were exposed to laboratory air, evacuated, and then baked at 150°C for 72 hours. Outgassing rates were measured for chamber temperatures between 20°C and 21°C. ....	44
Table V: Fit parameters $Q_0$ and $\alpha$ from Eq. 4.12. Given the fit parameters, the specific outgassing rate for water $Q_{H_2O}(t)$ is calculated at three times: $t_3 = 2 \times 10^3$ s, $t_4 = 10^4$ s, and $t_5 = 10^5$ s. The $Q_{H_2O}(t)$ at these three times are also normalized to those of the 304L chamber. ....	69
Table VI: Specific hydrogen outgassing rates $Q_{H_2}$ at 298.15 K. For Ti, $Q_{H_2}$ is taken as the average of all the Ti data. For the others, $Q_{H_2}$ is determined from the fitting parameters $A_0$ and $E_D$ from Eq 4.13. ....	72
Table VII. Estimated C6 coefficients in atomic units. Entries without references were calculated using the Casimir-Polder integral, for which we estimate a 10% uncertainty for the values. The coefficients do not depend on isotope to the accuracy given. Reproduced from Eckel et. al. <sup>115</sup> .....	80
Table VIII Measured pressure ratios in the XHV dynamic expansion system for selected gas species.....	110
Table IX - Calculated transmission probabilities and total conductance for a near-spherical orifice with 2 cm diameter in a ~2 mm thick plate. See Figure 6-14 for geometry. ....	114
Table X Published elastic loss rate coefficients, errors are reported at the $k = 1$ level. .	148
Table XI: Theoretical and experimentally determined first order loss rate coefficient for $^7\text{Li} \times \text{He}$ .....	152



## List of Figures

Figure 3-1: A schematic diagram of a cavity ring-down spectroscopy apparatus. Reproduced from van Zee et. al. (1999). .....	14
Figure 3-2: A plot of the lowest number density measurable during a one second measurement interval as a function of cross section for three sensitivities as demonstrated in van Zee et. al. (1999). .....	15
Figure 3-3: Silicon nitride mechanical damping gauge. The ringdown time for a 2 mm square by 50 nm thick, high-tensile-stress membrane is measure via piezoelectric actuation and optical detection. Inset shows fundamental out-of-plane vibrational mode. ....	18
Figure 3-4: Sample dynamic pressure data. The blue trace was recorded from a piezo electric transducer mounted perpendicular to the shock front. The Mach speed of the shock was measured to be 1.8. The initial conditions were 1.9 MPa and atmospheric pressure using Nitrogen on respective sides of the dual diaphragm. ....	20
Figure 3-5: Dual FP cavity refractometer shown with the thermal/vacuum apparatus removed: the upper channel is open to sense pressure, and the reference cavity is ion-pumped to high vacuum. ....	24
Figure 3-6: Disagreement in pressure as measured by two separate laser refractometers (pFP) and mercury ultrasonic manometer (pUIM). The dashed lines are the manometer uncertainty. The figure is reproduced from P. F. Egan, J. A. Stone, J. E. Ricker, and J. H. Hendricks, Rev. Sci. Instrum. 87, (2016). ....	25
Figure 3-7: Correcting FLOC distortion via finite-element analysis and an inspection of the mode position on the mirror. Pane (a) is an image of the mirror showing the bond interface. Through edge-detection, an estimate can be made of the area upon which the pressure acts. In (b), another image is taken with a laser beam aligned to the cavity resonance. By combining these two images, an estimate of the location of the beam on the mirror surface is made. The result of a finite-element analysis is shown in (c) datasheet values were used for elastic properties of ULE glass, and the geometry was estimated by the bond line in image (a). The difference in mirror bending calculated by finite-element is extracted as a profile, shown in pane (d). ....	27
Figure 3-8: (a) MIRE apparatus and (b) Refractometry cells of three different lengths but which are otherwise nominally identical. Each borehole has a gas inlet and outlet. (Left to right, the cell lengths are 18 mm, 134 mm, 254 mm.) Figure is adapted from P. Egan, J. Stone, J. Hendricks, J. Ricker, G. Strouse, Optics Letters 42, No. 15, 2944 (2017). .....	29

Figure 4-1: (a) standard vacuum components used to construct four identical chambers (b). The nominal dimensions are shown in (c). .....	39
Figure 4-2: (a) Schematic of measurement apparatus used to determine outgassing rates of the sample chambers. Two identical sample chambers $V_1$ and $V_2$ can be mounted simultaneously. Pane (b) shows the same apparatus, but with known volume $V_c$ attached to the measurement chamber. ....	42
Figure 4-3: Vacuum furnace system showing cutaway view of oven shell. (a) Hot zone main chamber, (b) snout, (c) low-temperature pumping stage, (d) turbo pump, (e) supporting plate and pedestals, (f) insulating boards, (g) table support, (h) table top, (i) main heaters $\times 4$ , (j) heavy aluminum screen, (k) four-inch thick insulation, (l) foil outer shell, (m) bottom heater, (n) screen disk for bottom heater, (o) pedestal heater. ....	50
Figure 4-4 Pumping system. (a) Main chamber and snout, (b) turbo pump, (c) dry scroll-type backing pump, (d) feedthrough for internal thermocouples, (e) cold-cathode high vacuum gauge, (f) thermocouple-type low vacuum gauge, (g) vent. ....	51
Figure 4-5: Schematic diagram of a single temperature control unit used to drive a 120 V heater tape. ....	53
Figure 4-6: Pressure vs time in the vacuum oven during one of our operations. The furnace was operated at 425 °C from day 0 until day 30, after which it was cooled to room temperature. ....	54
Figure 4-7: (a) Photograph of all sample chambers used in this study. These are (A) 304L, (B) 316L, (C) 316L-XHV, (D) 316LN, (E) 316LN-XHV, (F) Al, and (G) Ti. (b) cross section model view of a sample chamber. ....	58
Figure 4-8: Schematic of the apparatus used to determine the outgassing rates for the sample chambers. The water outgassing rates are determined using the throughput method and the hydrogen outgassing rates use the rate-of-rise method. ....	59
Figure 4-9: An example of the rate-of-rise data used to determine the specific outgassing rate of the 304L chamber. ....	62
Figure 4-10: The measured specific outgassing rates for water, $Q_{H_2O}$ , for all seven sample chambers, including repeats for 316L and 316L-XHV. (a) The present results for 304L compared to the results of Li and Dylla for chambers vented with air; (b) the present results for 304L compared to those of 316L, 316LN, 316L-XHV, and 316LN-XHV; (c) The present results for 304L compared to those of Ti and Al. ....	67
Figure 4-11: Arrhenius plots of the measured specific outgassing rate for $H_2$ , $Q_{H_2}$ for six chambers. ....	69

Figure 4-12: Plots of the measured specific outgassing rate for $H_2$ $Q_{H_2}$ for Ti as a function of relative time. ....	70
Figure 5-1: Schematic diagram of energy levels in a two-state atom, resonant photons $\lambda_0$ , and a red-detuned photon $\lambda$ . ....	77
Figure 5-2 Principles of the magneto optical trap. (Top) Atomic energy levels as a function of position $z$ in an applied magnetic field gradient with $B = 0$ at $z = 0$ . (Bottom) This results in a position-dependent force. ....	79
Figure 5-3: “First light” data. (a) Atom number decay in a magneto-optical trap (CAVS-MOT) data (circles) are fit to decay curves (solid curves) which are solutions to Eq. 14 and include single-body and two-body interactions. Panel (b): Pressure in the CAVS-MOT as determined by the data in panel (a) converted to pressure using semi-classical cross section estimates plotted versus an uncalibrated ion gauge.....	84
Figure 6-1 Cutaway view of CAVS chamber showing the pumping region, the source stage, and the sensing stage. The alkali-metal atoms are injected by the (1) source which is angled to minimize contamination in the sensing stage while giving the atoms some initial momentum in the axial direction. A differential pumping tube (2) allows for lower pressures in the sensing chamber. The cooling shroud (3) increases the surface sticking coefficient and thus decreases stray alkali contamination. The vacuum under test attaches at (4). Red beams indicate lasers, magnetic field coils not shown. ....	88
Figure 6-2 Rendering of Bitter coil assembly. The 3D-printed water distribution manifold is white, a section has been cut away to reveal the geometries of the supply and collection reservoirs. The four leaves of the clover coil sit directly on this distribution manifold (one is hidden to allow the manifold interior to be seen). The inset shows an exploded view of the coil stack with insulating spacers (green and white) that create flow channels between conductive layers (brown). Pink arrows mark the flow of electric current, blue arrows mark the flow of cooling water. ....	91
Figure 6-3 Rendering of one of the two CAVS RF antenna PCBs. The RF current source driving the loop antenna is located bottom middle. The loop antenna itself is patterned on an internal PCB layer and not visible. The RF current sources for the linked-quadrant antennas are on the left and right. White silkscreen markings within each quadrant antenna show the local direction of the RF magnetic field.....	93
Figure 6-4: 3D printed titanium tube and plug. ....	96
Figure 6-5 Background-subtracted (i.e., source on minus source off) mass spectrum of gas composition with $T = 330^\circ\text{C}$ . The total pressure including background is $3.3(6) \times 10^{-7}$ Pa.....	98
Figure 6-6, reproduced from Norrgard et. al. Loading rate $R$ (black squares) and steady-state atom number $N$ (red circles) as a function of temperature $T$ . The inset shows a typical MOT loading curve with $T = 330^\circ\text{C}$ . Black squares are measurements and the red line is a prediction, for detail see Norrgard et. al. ....	99



Figure 6-7 MOT loading with 490 mW of light from the 385 nm LED. (a) The atom number as a function of time in green and fits to the data in purple, with solid lines indicating loading and dashed lines indicating decay. The vacuum pressure measured by an ion gauge is shown in (b). The solid (dashed) black line in the bottom subplot indicates a double exponential growth (decay) fit to the pressure data. The vertical dotted lines denote the beginning and end of MOT loading..... 102

Figure 6-8 - Saturated atom number (a) and loading rate (b) for the  $^7\text{Li}$  MOT as a function of LIAD power. Data are for LIAD sources operating at 385 nm (lavender circles), 405 nm (purple triangles), and 445 nm (blue squares). The solid lines in (b) are linear fits to the measured loading rate. Error bars are one standard deviation..... 104

Figure 6-9: Basic schematic of a simple Dynamic Expansion chamber..... 105

Figure 6-10 View of XHV DE lower chamber, showing UHV getter pumps above the top of the turbomolecular pump..... 107

Figure 6-11 Cartoon schematic depicting the XHV-DE as a three-chamber system. .... 108

Figure 6-12: Full system schematic of the XHV-DE, similar to Figure 6-3 but showing the flow splitter and getters, as well as indicating outgassing. Flow splitter orifices are shown in red..... 106

Figure 6-13: (a) bottom-view of nominal 2 cm orifice being installed onto orifice plate. The researcher is tightening the indium seal to close all alternate gas pathways. (b) top-view of orifice immediately following installation..... 111

Figure 6-14: Cross section of slab (blue) with partial-spherical orifice, which can be thought of as a spherical bubble with radius  $R$  that extends a distance  $x_a$  ( $x_b$ ) above (below) the upper (lower) face of the slab. The circular hole in the upper face of the slab has radius  $r_a$ .  $Q_a$  and  $Q_b$  are the pieces of the spherical bubble that extend beyond the slab, useful for characterizing the transmission probability of the orifice. Short cylindrical section not pictured here. .... 111

Figure 6-15. An orifice with near partial-spherical cross section. In order to be machinable, there must be a small cylindrical “land” or tube (a truly spherical cross section would have an infinitely sharp edge). The diameter of the tube is  $2r_b$  and its length is  $L_T$ ..... 113

Figure 6-16 Schematic of the core of the Flowmeter, the volume of the variable volume is adjusted by compressing the bellows. This is controlled via feedback to the differential gauge  $\Delta p$ , keeping the pressures in the reference and variable volumes equal. .... 116

Figure 6-17: Bakeable CDGs (pink) inside a temperature controlled box with plumbing manifold. .... 119

Figure 6-18: The offset  $c_0$  fit coefficients versus run number for the 1-torr gauge with gain X1 (top); 10-torr gauge with gain X1 (middle); and 1000 torr gauge with gain X0.1 (bottom)..... 122

Figure 6-19 Linear sensitivity  $c_1$  coefficients versus run number for the 1-torr gauge with gain X1 (top); the 10-torr gauge with gain X1 (middle); and the 1000-torr gauge with gain X0.1 (bottom)..... 122

Figure 6-20 (a) example of global fit function for the 1-torr gauge, dots show experimental data, and the black line is the fit. Panes (b), (c), and (d) show residuals of the fit vs. pressure reading  $R$  for the 1-torr, 10-torr, and 1000-torr gauges, respectively. Colored curves indicate the difference of the single-run fit and the global one, and dashed black curves show the estimated  $2\text{-}\sigma$  width of the residuals..... 125

Figure 6-21 Absolute (top) and relative (bottom) uncertainties for the 1-torr (blue), 10-torr (orange), and 1000-torr (green) gauges vs. pressure  $P$ . The thick solid lines indicate the total uncertainty  $u_p$ , the dashed curves indicate the uncertainty in the transfer standard  $u_{\text{trans}}$ , the dashed-dot curves show the uncertainty in the long-term stability  $u_{\text{lts}}$ , the dotted curves show the uncertainty in the fit  $u_{\text{fit}}$ , and the thin solid curves show the average uncertainty due to random fluctuations  $u_{\text{rdm}}$  during a single calibration run. All uncertainties are at the  $k = 2$  level. .... 127

Figure 7-1: A 3D model of a possible commercial pCAVS device, including a model of the triangular grating chip. Reprinted from S. Eckel, D. Barker, J. Fedchak, N. Klimov, E. Norrgard and J. Scherschligt, *Metrologia* (2018). .... 128

Figure 7-2: Photograph of the prototype CCT triangular grating chip, with ruler. .... 131

Figure 7-3 Glancing collision-corrected loss rate coefficient for ground state  ${}^6\text{Li}(^2\text{S})$ , pane (a), and  ${}^{85}\text{Rb}(^2\text{S})$ , pane (b) as a function of trap depth for various background gases at  $T = 293\text{ K}$ . The result to first-order only is shown for  $\text{H}_2$  (thin-dashed curve), indicating the range over which it is applicable. The red-striped (blue) shaded regions highlight the accessible range of trap depths with a magnetic (magneto-optical) trap. .... 132

Figure 7-4 Geometry of the pCAVS grating. A single laser beam (large red arrow) is diffracted into six beams (small red arrows) by three reflective gold diffraction gratings whose lines form superimposed triangles and diffract light at  $\theta_d = \pi/4$  with respect to the normal of the grating ( $-\hat{z}$ ). Grating lines are not to scale. .... 134

Figure 7-5 Trap depth for a typical three-beam grating MOT for Li. (a) angularly-resolved  $W(\Delta, \phi)$  for an incident beam at saturation intensity and with detuning  $\Delta/\gamma = -1$  and  $dB_z/dz = 0.5\text{ T/m}$ . (b) Average trap depth as a function of incident beam intensity for detunings  $\Delta/\gamma = -3.0$  (solid blue),  $-2.0$  (dashed orange), and  $-1.0$  (dashed-dot green) with  $dB_z/dz = 0.5\text{ T/m}$ . (c) Average trap depth as a function of magnetic field gradient at saturation intensity and with detuning  $\Delta/\gamma = -1$ . .... 135

Figure 7-6 Energy of the magnetic sublevels as a function of magnetic field for  $6\text{Li}$  (pane a),  $7\text{Li}$  (pane b) and  $85\text{Rb}$  (pane c). Blue solid curves correspond to states that are magnetically trappable, Red dashed curves depict states that have negative slope and thus are not magnetically trappable. .... 137

Figure 7-7 CAD rendering of a prototype pCAVS. The total vertical size is about 10 cm. The atomic shutter is not shown, it fits snugly between the dispenser and the differential pumping tube. .... 139

Figure 7-8 Recaptured atom number vs time  $t$ . The blue points are for pCAVS #1 and the orange are for pCAVS #2. These example decays were captured before (a) and after (b) repairing a leak. .... 141

Figure 7-9 Pressure measured by pCAVS #2 as functions of power  $P$  dissipated in pCAVS #1 with its shutter open (purple) or closed (green). .... 143

Figure 8-1 Example Background data. The decay is approximately exponential (straight line), but some curvature on this plot indicates two-body processes are present. .... 150

Figure 8-2 decay curves for  $7\text{Li} \times \text{He}$  at a number of different helium pressures. Color encodes fill pressure which scales with chamber pressure, higher slopes are higher pressures. From left to right, fill pressures in torr are 7.50 (blue), 5.62 (teal), 4.22 (peridot), 3.16 (gray), 2.37 (pink), 1.78 (brown), 1.33 (violet), 1.00 (red), 0.75 (green), 0.56 (orange), 0.42 (navy). .... 151

Figure 8-3 Loss rate coefficient  $K$  vs Pressure in the pCAVS for the  $7\text{Li} \times \text{He}$  system. Error bars are calculated as described in the text. The solid horizontal line shows the weighted mean of these experimental values, dashed lines are at one standard deviation of the mean. The gold band is the  $k = 1$  confidence interval for the theoretical value. .... 152

## List of Abbreviations

Abbreviation	Meaning
AMD	Alkali Metal Dispenser
AMO	Atomic, Molecular, and Optical physics
BIPM	International Bureau of Measures
CAD	Computer-Assisted Design
CAVS	Cold Atom Vacuum Standard
CCT	Cold Core Technology
CDG	Capacitance Diaphragm Gauge
CF	ConFlat (flange type)
CIPM	International Committee for Weights and Measures
CRDS	Cavity Ring-Down Spectroscopy
DE	Dynamic Expansion
DN	Nominal Diameter
EMRP	European Metrology Research Programme
EOM	Electro-Optic Modulator
ESD	Electron Stimulated Discharge
EURAMET	European Association of National Metrology Institutes
FLOC	Fixed-Length Optical Cavity
FP	Fabry-Perot
IG	Ion Gauge
IP	Ioffe-Pritchard
ISO	International Standards Organization
LED	Light Emitting Diode
LIAD	Light-Induced Atomic Desorption
MEMS	Microelectromechanical systems
MIRE	Monolithic Interferometer for Refractometry
MOT	Magneto-Optical Trap
MPI	Multi-Phonon Ionization
NBS	National Bureau of Standards
NEG	Non-Evaporable Getter
NIST	National Institute of Standards and Technology
NMI	National Metrology Institute
OD	Outer Diameter
pCAVS	Portable Cold Atom Vacuum Standard
PCB	Printed Circuit Board
PDMS	polydimethylsiloxane
PRT	Platinum Resistance Thermometer
PTB	Physikalisch-Technische Bundesanstalt (German NMI)
QED	Quantum Electrodynamics
REMPI	Resonant-Enhanced Multi-Photon Ionization

Ra	Roughness average
RF	Radio Frequency
RGA	Residual Gas Analyzer
SCE	Standard Conductance Element
SI	International System of Units
SRG	Spinning Rotor Gauge
TEC	Thermoelectric Cooler
TOF	Time of Flight
UHV	Ultra High Vacuum
UIM	Ultrasonic Interferometer Manometer
ULE	Ultra-Low Expansion
UV	Ultraviolet
VIM	International Vocabulary of Metrology
VLOC	Variable Length Optical Cavity
VOC	Volatile Organic Compounds
XHV	Extreme High Vacuum
XHVFM	Extreme High Vacuum Flowmeter

## Chapter 1: Introduction

As the national metrology institute of the United States, NIST has responsibility to maintain and disseminate the unit of pressure, the pascal (Pa). Since its inception as the National Bureau of Standards (NBS) in 1901, NIST has advanced the science of pressure metrology, investigating new techniques and technologies, as well as developing the science underpinning what it means to measure the pascal. Pressure metrology is particularly challenging in the vacuum, and especially in high vacuum ( $<10^{-4}$  Pa) where the mean-free-path of molecules are longer than the dimensions of typical laboratory apparatuses. Moreover, in the ultra-high vacuum (UHV,  $<10^{-6}$  Pa)—a pressure regime critical to advanced research and technology<sup>1</sup>—there has not existed an absolute pressure sensor. Recently, NIST has launched two initiatives to realize the pascal for vacuum pressures in a fundamentally modern way, by interrogations of quantum mechanical systems that directly relate to the particle density and therefore pressure in the vacuum. The *Fixed-Length Optical Cavity* (FLOC) is an index of refraction-based measurement. The CAVS uses cold trapped atoms to sense vacuum. The FLOC will be discussed briefly, and the CAVS will be discussed in great detail. Both efforts are consistent with the Quantum-SI. Another nascent effort at NIST is the SiN ring-down membrane gauge, which we dub the “brane gauge.” Based on optomechanics, the brane gauge also has the prospective to be a Quantum-SI sensor in the vacuum, though at the moment the project is in very early stages. Past efforts at NIST have explored using resonant-enhanced multi-photon ionization (REMPI) and cavity ring-down spectroscopy (CRDS) techniques as

tools for partial pressure analysis in the UHV and below, as well as spectroscopic techniques for measuring transient pressure.

Traditionally pressure is defined as a force per unit area, but as pressures extend further and further below an atmosphere (deeper into the vacuum) this definition becomes increasingly inconvenient and impractical. Instead, at low pressures the pascal is realized through the ideal gas law,

$$p = \rho_N k_B T = \rho_V R T \quad 1.1$$

where  $\rho_N$  is the number density of particles and  $\rho_V$  is the molar density,  $R$  is the gas constant, and  $T$  is the temperature. In this formulation, pressure metrology becomes a counting problem, specifically, counting particles in the vacuum by any available technique. This reflects the applications as well: in the high-vacuum and below, most users are concerned with the amount of gas in the vacuum, e.g. as a contaminant, rather than the force it produces. Eq. (1) fundamentally relates pressure to the Boltzmann constant  $k_B$ , which is now a fixed constant following the redefinition of the SI in 2019.<sup>2-4</sup> With modern techniques and the trend away from artifact-based metrology, NIST and other institutes are developing the Quantum-SI, in which the units are tied to defined physical constants, e.g. Plank's constant or the speed of light in vacuum. Furthermore, there is an accompanying shift away from electronic to photonic measurements. Measuring photons instead of electrons has several inherent benefits: optical signals are generally less prone to pick-up noise from stray signals than are electrical signals, especially for long transmission distances. Photonic signals are high-fidelity and can travel farther without regeneration. Additionally, optical fiber is lighter and has a larger bandwidth per cross-sectional area than copper wire, and can better handle harsh

conditions, and so it has practical advantage, especially for use in aircraft or launch vehicles. Photonic measurements can be readily multiplexed and allow remote interrogation. Furthermore, photons can be used to directly probe the electronic states of atoms or molecules, and to prepare quantum states, making them the tool of choice for fundamental quantum measurements.

At pressures from about an atmosphere to the high vacuum, classical metrology technologies are mature and can deliver uncertainties at the level of a few parts in  $10^6$ , generally adequate for users and stakeholders. In consideration of this, the NIST efforts to recast the SI in terms of quantum effects are not necessarily an attempt to further reduce uncertainties—though we hope that as the technologies occur this will become possible. Rather, by developing quantum-SI based techniques at these higher ranges, our goal is to enable stakeholders to have their own standards that are of the highest metrological integrity that never need calibration. Furthermore, these new technologies may enable the user to use the same device as a primary standard and a sensor, or as calibration-free sensors. Another advantage of pressure standard based on the FLOC technique is that it has the perspective to replace traditional mercury manometers, which are often used in the vacuum range of  $10^{-3}$  Pa to  $10^5$  Pa, thus removing large quantities of toxic mercury from the calibration lab. The primary high-accuracy manometers used in this pressure range also tend to be rather large, expensive, and require a high level of expertise to operate, and are thus usually owned and operated by national metrology institutes or sophisticated calibration laboratories. The FLOC and the other Quantum-SI techniques (such as the CAVS) presented in this introduction, all have the potential to be portable primary standards.



In the UHV and below, using photons to probe pressure is very appealing compared to the traditional ionization gauges and quadrupole mass spectrometers. These have been the subject of many reviews.<sup>5–12</sup> In these traditional gas sensing techniques, ions are created via impact with electrons emitted from a hot-filament or, as is the case for a cold-cathode gauge, in a high-potential cathodic discharge. These ions are then detected by generating a current on an electrode or by an electron multiplier. Although these techniques have been the mainstay for UHV detection for several decades and many improvements have been made to make them more stable or to detect lower vacuum levels,<sup>13–17</sup> they have not been completely satisfying for measuring total or partial pressures in the UHV or extreme-high vacuum (XHV  $<10^{-9}$  Pa) for several reasons. First, the heat generated by these gauges cause sufficient outgassing to change the pressure in a vacuum system, second, the electron impact can “crack” molecules into fragments thus changing the chemical composition of the gas (a particular problem in partial pressure analysis), third, the chemical composition can also be altered by chemical reactions on the hot filaments or other surfaces within the ionizer, fourth, the ionization technique does not produce a primary sensor, i.e., an absolute sensor that does not require calibration. Additionally, electron-stimulated desorption (ESD) of ions from surfaces and the generation of X-rays due to electron impact on surfaces cause false signals. Photonic and Quantum-SI methods have the potential to create absolute sensors without these problems. The heat-load on the vacuum system generated by photons is anticipated to be many orders of magnitude less than in ionization techniques. This reduces the possibility of changing the chemical composition of the gas and outgassing in the system. Most stakeholders for UHV or XHV metrology require uncertainties merely on the order of

parts per hundred, but as discussed above, presently there is no primary sensor of any kind in this vacuum range.

NIST has supported vacuum metrology through its calibration services and by developing and maintaining vacuum standards. Presently these cover the vacuum range down to  $10^{-7}$  Pa. These efforts support a wide variety of industries and research, such as semiconductor manufacturing, quantum information, particle physics facilities, space sciences, and nanotechnology. Developing Quantum-SI standards to cover the present range of NIST's capabilities, as well as pushing standards to cover vacuum to  $10^{-10}$  Pa or below (XHV), is a high priority. We are particularly motivated to develop Quantum-SI sensors to cover the entire UHV range and below. We visualize a new era of high metrological quality Quantum-SI sensors based on cold atoms that measure quantities such as time (which is already based on ultra-cold atoms), inertia, magnetic fields, gravity, and, of course, vacuum pressure. All such devices, and ultra-cold atom research in general, require UHV pressures or below to operate. Similarly, UHV quality is a concern in the field of quantum information. Building practical sensors and devices from cold atoms will require that UHV pressure be maintained over the lifetime of the device. One suggested metric for this is  $10^{-8}$  Pa for 1000 days.<sup>18</sup> The vacuum requirements are a technical challenge in creating such devices. We are presently developing a portable metrology device for deep vacuum that is simultaneously a Quantum-SI standard and a sensor. The portable CAVS or pCAVS will address these technical challenges and be a tool for quantum research and development.

In early chapters we review the current state of the art. Chapter 2: is a brief overview of traditional vacuum metrology, then in Chapter 3: we discuss early work to

move beyond artifact-based measurements: multiphoton ionization and cavity ringdown spectroscopy. Next, we will describe a new research effort to develop the brane-gauge, followed by a discussion of NIST's work on spectroscopic techniques for measuring transient pressure. Special attention will be paid to the lower pressure limits anticipated in these new standards and sensors. We then cover in more detail the FLOC which operates at pressures from 1 Pa to  $\gtrsim 100$  kPa, CAVS which operates from ultra-high vacuum to extreme-high vacuum (UHV to XHV, or from about  $10^{-6}$  Pa to  $< 10^{-9}$  Pa). Included is a discussion on how these new approaches will enable the next generation of practical, deployable sensor technologies for vacuum.

## Chapter 2: Traditional Pressure Metrology

The concept of metrology coevolved with the that of commerce as early as 3100 BCE in Mesopotamia, and was the precursor to the development of both western mathematics and written language.<sup>19</sup> For thousands of years until the last century, the science of measurement relied entirely upon comparisons between objects of interest and standard artifacts, but since the advent of modern physics, new ways to realize units of measure have begun to take hold that are based on immutable properties of nature, particularly for length (based on the speed of light) and time (based on quantum properties of atoms). Pressure is traditionally defined as force per unit area,  $P = F / A$ , and has units of pascal ( $1 \text{ Pa} = 1 \text{ N m}^{-2}$ ). Therefore, to generate or realize the pascal, the most obvious method is to apply a known force to a known area. This is the operating principle behind the piston gauge, the workhorse primary pressure standard for pressures around an atmosphere (100 kPa) to a few hundred megapascal. Piston gauges consist of a piston and cylinder assembly with well-characterized dimensions—for proper primary standards, the area of the piston gauge is measured using primary dimensional metrology and corrected for distortion effects with careful numerical modeling. The gauge is then loaded with mass units that have been independently characterized using standard techniques in mass metrology. The combination of known mass and known area gives pressure. Though the details of operation have been modernized and refined, the underlying concept of the technique is ancient.<sup>20,21</sup>

For measurements at atmospheric pressures and into the low vacuum, manometry is the traditional technique. The manometer is generally considered to be invented by Torricelli in the seventeenth century,<sup>22</sup> and though it has been incrementally refined and

improved over the centuries, it has remained the state-of-the-art until now. Manometers operate on the principle that a fluid in a column sealed at the top will create a vacuum in the sealed end of the column when it experiences the downward force due to its own weight. The pressure on the other end of the column (the pressure of interest, often atmosphere) exerts a force that must balance the gravitational force, for the fluid to be in equilibrium. The pressure in pascal is then  $P = \rho_f g h$  where  $\rho_f$  is the fluid density,  $g$  is the local acceleration due to gravity, and  $h$  is the column height. NIST operates Ultrasonic Interferometer Manometers (UIMs), with mercury as the fluid (with a full-scale range of 360 kPa) and with oil as the fluid (with a range of 0.1 Pa to 120 Pa). The determination of column height is done using an ultrasonic technique, and care is taken to minimize uncertainty from other sources including temperature. These instruments can claim relative standard uncertainties as low as  $3 \times 10^{-6}$  as demonstrated in an international key comparison.<sup>23,24</sup>

At lower pressures, it becomes much more convenient to formulate the pascal as the translational kinetic energy density of particles in a volume ( $1 \text{ Pa} = 1 \text{ J m}^{-3}$ ), rather than a force applied to an area as defined above. To generate pressures in the high vacuum and ultra-high vacuum, a commonly used method is to use a flowmeter with dynamic expansion technique. In this technique, a known flow of gas  $\dot{n}$  is injected into a vacuum chamber upstream of a flow constrictor (usually an orifice) with a known conductance  $C$ . In the molecular flow regime (where the mean-free path is larger than the vacuum vessel or flow constrictor), the pressure difference across the flow limiter is given by the pressure analogy to Ohm's law,

$$p_{upper} - p_{lower} = \dot{n}RT/C \quad 2.1$$

which tells us that the pressure difference across an orifice is the flow of particles  $\dot{n}$  across the orifice divided by the conductance. The upstream pressure,  $p_{\text{upper}}$  is the pressure above the flow constrictor (typically an upper chamber in a vacuum system), and  $p_{\text{lower}}$  is the pressure downstream of the flow constrictor (typically a lower chamber in a vacuum system). A high pumping-speed vacuum pump is connected to the lower chamber such that  $p_{\text{upper}} > p_{\text{lower}}$ . If the ratio  $p_{\text{upper}} / p_{\text{lower}}$  is known from a separate measurement, or  $p_{\text{upper}} \gg p_{\text{lower}}$  and  $p_{\text{lower}}$  can be neglected, then a standard pressure  $p_{\text{upper}}$  may be determined from the known  $C$  and  $\dot{n}$ . To produce a known flow of gas  $\dot{n}$  with low uncertainty, a constant pressure flowmeter may be employed whereby a known flow,  $\dot{n}$ , from a leak in a volume  $V(t)$  is determined by inducing a volume change  $\dot{V}$  to hold the pressure  $p$  within the volume constant.<sup>25–27</sup> We see from Eq. 2.1 that the gas flow can be written  $\dot{n} = p\dot{V} / N_A k_B T$ , where  $N_A$  is Avogadro’s constant and the gas flow  $\dot{n}$  has units of mol/s. The flowmeter plus dynamic expansion apparatus together constitutes the present state-of-the-art standard for high vacuum and ultra-high vacuum. However, it should be noted that this system fails to meet the technical definition of primary (for pressure) according to the International Vocabulary of Metrology (VIM) because the flowmeter relies on a calibrated pressure gauge.<sup>28</sup> Still, it is *functionally* primary<sup>\*29</sup>—many national metrology institutes (NMIs) which operate these standards calibrate these pressure gauges using primary methods—, and is used extensively at NIST, the metrology institute of Germany (Physikalisch-Technische Bundesanstalt or PTB), and other NMIs for

---

\* By functionally-primary, we mean a measurement method that relies on a one-time measurement of some physical quantity of like kind, thereby making it fail the strictest interpretation of the definition of primary set forth in the VIM,<sup>24</sup> but which is otherwise consistent with the concept of primary standards, and can be used to realize and disseminate the quantity at the NMI level, as described in Quinn<sup>29</sup>.

calibrations of vacuum gauges, notably ionization gauges and spinning rotor gauges.<sup>25,30–</sup>

34

*Table I: Consensus values for best-possible calibration uncertainties for traditional gauges covering all accessible vacuum pressures.*

Gauge Type	Range minimum (Pa)	Range maximum (Pa)	Best uncertainty ( $1\sigma$ )
piston gauge	1400	$7 \times 10^5$	$0.015 \text{ Pa} + (1.6 \times 10^{-7})P$
resonance- or resistance-based pressure transducer	5000	$3.5 \times 10^5$	$0.1 \text{ Pa} + (2.5 \times 10^{-6})P$
capacitance diaphragm gauge	0.1	$1.30 \times 10^5$	$5 \times 10^{-7} \times (\text{full scale}) + (5 \times 10^{-6})P$ , but not less than $5 \times 10^{-5} \text{ Pa}$
non-rotating piston gauge	1	$1.5 \times 10^4$	$0.004 \text{ Pa} + (8 \times 10^{-6})P$
spinning rotor gauge	$1 \times 10^{-4}$	1	$7 \times 10^{-7} \text{ Pa} + (5 \times 10^{-4})P$
metal-envelope ionization vacuum gauge	$1 \times 10^{-7}$	$1 \times 10^{-3}$	$1 \times 10^{-9} \text{ Pa} + (1 \times 10^{-3})P$
extractor gauge with electrometer	$1 \times 10^{-9}$	$1 \times 10^{-3}$	$1 \times 10^{-10} \text{ Pa} + (1 \times 10^{-3})P$

This author served as the chair of a task group of the International Committee for Weights and Measures (CIPM) to reach international consensus values for what constitute the lowest possible calibration uncertainties across all possible pressure ranges for the device considered to be of highest quality at that range. This work was completed in 2022, and the results for the vacuum range (absolute pressure around or below an atmosphere, or  $\sim 100 \text{ kPa}$ ) are presented in Table I. These values help contextualize the work described in this thesis, which is partly an attempt to improve these uncertainties especially at the lowest ranges. There are no consensus values for partial pressures, which remain an outstanding concern in the community.

In 2019 the values of physical constants were fixed by the CIPM, with profound consequences on metrology in general and pressure metrology in particular. With fixed values of the Boltzmann constant and Avogadro's number, direct measurement of  $\rho_N$  or  $\rho_V$  gives pressure absolutely (assuming that temperature uncertainty can be suppressed sufficiently low as to be negligible.) So (ignoring for the moment a few complicating details) because the FLOC and the CAVS assess number density  $\rho$ , they have become *de facto* primary pressure standards following the redefinition of the SI. Before discussing these projects in more detail, we turn to pioneering efforts at NIST to measure vacuum using photonic-based spectroscopic techniques.



## Chapter 3: Overview of Modern Approaches to Pressure Metrology

This chapter is reproduced from Scherschligt et. al. Review Article: Quantum-based vacuum metrology at the National Institute of Standards and Technology. *J. Vac. Sci. Technol. A* **36**, 040801(2018).<sup>35</sup>

### 3.1 Resonant-enhanced multi-photon ionization

Multi-photon ionization (MPI) can be used to ionize molecules which can be subsequently detected using traditional techniques such as by electron multipliers or multichannel plates. It has advantages over electron-impact ionization techniques based on, for example, hot filaments, which tend to outgas, promote chemical reactions, and produce indiscriminate fragmentation of gases. In the 1990's, Looney and coworkers made quantitative partial pressure measurements of CO using the laser-based technique of resonant-enhanced multi-photon ionization (REMPI) techniques.<sup>36,37</sup> They found it possible to detect CO partial pressures as small as  $10^{-10}$  Pa, and demonstrated the ability to measure partial pressures of  $10^{-9}$  Pa with an uncertainty of 20 to 30%. In REMPI, a molecule is excited by one or more photons to an electronic intermediate state, and subsequently ionized by absorbing one or more photons from the intermediate excited state. CO is ionized via a three-photon process: a two-photon excitation using 230 nm laser light promotes the molecule from a  $X^1\Sigma^+$  state to the  $B^1\Sigma^+$  state, where the molecule is subsequently photo-ionized by another 230 nm photon. Resonant ionization techniques have the advantage over non-resonant techniques in that it is selective in gas species, making it very sensitive detection technique for specific gases. Previous to the NIST work, REMPI had already shown promise as a sensitive detection technique,<sup>38</sup> and continues to be an active field today. The work done at NIST by Looney and coworkers

demonstrated the first quantitative REMPI measurements. They used a time-of-flight (TOF) mass spectrometer to detect ionized CO. The TOF spectrometer was capable of resolving CO from N<sub>2</sub>, but no ionized N<sub>2</sub> was detected, thus demonstrating the excellent species selectivity of the REMPI technique. The TOF mass spectrometer signal was calibrated against a spinning rotor gauge using a split-flow technique, thus enabling quantitative partial pressure detection of CO. The REMPI technique is an excellent way to detect specific gases in the UHV and XHV, and is particularly useful for chemically active gases. In order for the REMPI technique to be used for absolute measurements of partial pressure, the accurate cross-sections for multi-photon ionization must first be determined, which is a difficult task and remains outstanding for many molecules.

### 3.2 Cavity ring-down spectroscopy

Another highly sensitive optical detection technique is that of cavity ring-down spectroscopy (CRDS) shown schematically in Figure 3-1. NIST began a program to develop CRDS into a highly sensitive quantitative tool for the detection of molecules the 1990s.<sup>39,40</sup> A laser pulse is injected into a high-finesse optical cavity defined by two highly reflective mirrors of reflectivity  $R$  separated by the cavity length  $l$ . The output intensity will have a “ring-down” time given by the expression<sup>41</sup>

$$\tau(\omega) = \frac{l}{c[(1-R) + \alpha(\omega)l]} \quad 3.1$$

where  $\alpha(\omega)$  is the absorption coefficient of the gas within the optical cavity.  $\alpha(\omega)$  can be determined from the difference between the cavity ring-down time for an empty cavity and that containing the gas of interest. In fact, the CRDS technique is a powerful tool for measuring absorption coefficients,<sup>42</sup> particularly those for weak transitions. The

absorption coefficient is related to the number density of the gas  $\rho_N$ , the line strength of the absorption transition  $S$ , and the normalized line-shape function  $f(\omega)$ :

$$\alpha(\omega) = 2\pi c \rho_N S f(\omega) \quad 3.2$$

Thus if  $S$  and  $f(\omega)$  are known, the number density  $\rho_N$  and hence gas pressure can be determined from the ring-down time.

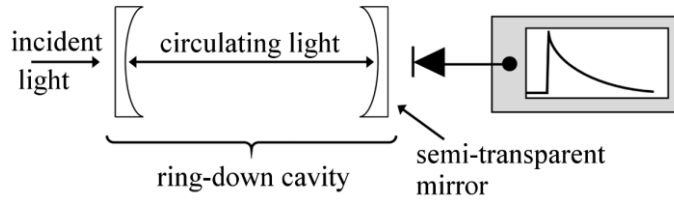


*Figure 3-1: A schematic diagram of a cavity ring-down spectroscopy apparatus. Reproduced from van Zee et. al. (1999).*

Like the REMPI technique, the CRDS method is most useful for sensing specific gases. In principle, it can be used to sense virtually any molecule, with the practical caveat that the molecule must have an absorption transition which is both strong enough to do CRDS, and whose energy corresponds to wavelength accessible by available lasers. The CRDS method has been shown to be capable of sensing  $\text{CO}_2$  concentrations at the level of 43 parts in  $10^{15}$ .<sup>43</sup> As pointed out in Jousten *et al.*,<sup>44</sup> this corresponds to a partial pressure of  $4.3 \times 10^{-9}$  Pa; however, it is not clear that the CRDS method can be used to detect UHV or XHV partial pressures for an arbitrary gas. As discussed in van Zee *et al.*,<sup>41</sup> there is a minimum detectable absorptivity which depends inversely on  $\tau^2$  and inversely on the square root of the number of measurements. This means that UHV or XHV measurements require a minimum absorption strength  $\alpha$  for a given cavity length and data acquisition time. From the examples given in van Zee et al. (see Figure 3-2),

using CRDS to detect UHV partial pressures for molecules like CO or CO<sub>2</sub> may be possible, but it may not be practical for molecules such as H<sub>2</sub>O or C<sub>2</sub>H<sub>2</sub>. For partial pressure measurement, much of the NIST program has focused on detecting concentrations of gas in nominally atmospheric pressures, such as O<sub>2</sub> or H<sub>2</sub>O in N<sub>2</sub>. The NIST program has been successful in performing highly accurate measurements of water vapor pressure;<sup>45,46</sup> molar fractions of water vapor equal to  $7 \times 10^{-8}$  have been determined.<sup>47</sup>

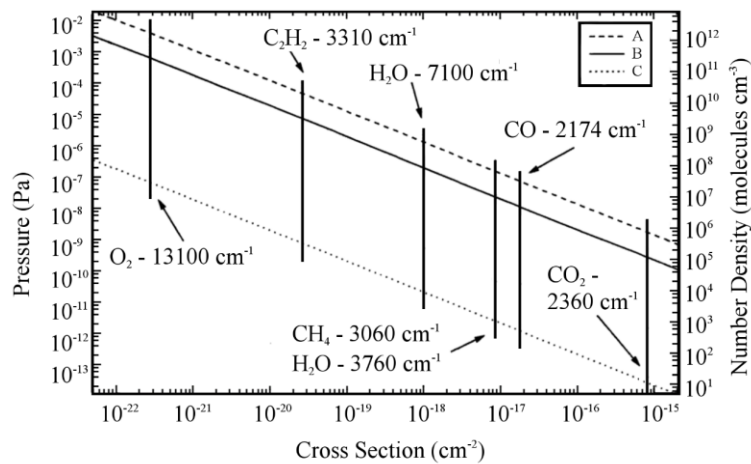


Figure 3-2: A plot of the lowest number density measurable during a one second measurement interval as a function of cross section for three sensitivities as demonstrated in van Zee et. al. (1999).

### 3.3 SiN Ring-Down Membrane Gauge (the “brane” gauge)

Mechanical damping by drag forces on many types of structures has been used for a wide range of vacuum pressure sensors.<sup>48</sup> Broadly two classes of devices exist, levitated spinning rotors (or spinning rotor gauges),<sup>49</sup> which notably have been employed as stable transfer standards for high vacuum<sup>50</sup> and oscillating mechanical resonators, ranging from MEMS devices to macroscopic pendula and torsional oscillators. Generally, these gauges are desirable because they act as absolute pressure sensors with high linearity, operate at high frequencies away from DC to minimize low frequency noise and drift,

often allow for direct computation of pressure dependence from first principles, and do not generate large amounts of heat. The linear dynamic range is limited by intrinsic mechanical dissipation at low pressure, and the transition from molecular flow to viscous damping at high pressure. So the ideal properties of such gauges include low intrinsic mechanical dissipation and a mechanical element that is smaller than the mean free path of the gas being measured at the highest pressures of interest. A larger mechanical element would still exhibit pressure-dependent damping, but it would not be characteristically linear.<sup>50-52</sup>

We are interested in developing a mechanical damping gauge for high vacuum in range of  $10^{-6}$  to  $10^{-2}$  Pa, which is simple, robust, and sufficiently stable to operate as a sensor and transfer standard. The successful combination of this device with the FLOC and the CAVS will constitute a suite of instruments that covers the entire pressure range from a few atmospheres to the lowest achievable laboratory vacuums. Recent experimental progress in the field of quantum optomechanics has led to the development of optically detected and actuated mechanical resonators, well suited for gas damping pressure sensing. The mechanical sensing element consists of an ultralow intrinsic damping rate,  $\Gamma_i$ , silicon nitride membrane, whose out-of-plane drumhead modes (Figure 3-3, inset) have ultrahigh intrinsic mechanical quality factor ( $Q = \omega_m/\Gamma_i$ ), approaching 1 billion. With millimeter scale transverse extent and thickness,  $h$ , less than 30 nm, these mechanical resonators are readily damped by surrounding gas, while retaining resonance frequencies,  $\omega_m/2\pi$ , in the hundreds of kilohertz. These devices allow for simple optical readout, are insensitive to low frequency vibration, magnetic fields, and sensor tilt, and

do not require active stabilization. The total mechanical damping rate, the inverse of the mechanical ringdown time,  $\tau_{rd}$ , in the molecular flow regime is approximated by<sup>50</sup>

$$\frac{1}{\tau_{rd}} = \Gamma_{tot} = \Gamma_i + p \sqrt{\frac{32}{\pi} \frac{m_m}{k_B T}} \frac{1}{\rho h} \quad 3.3$$

where  $m_m$  is the molecular mass of the gas at pressure  $p$ , and  $\rho$  is the density of silicon nitride. Recent devices have demonstrated that sub-mHz intrinsic damping rates are achievable,<sup>53–55</sup> equivalent to the damping from air pressure in the  $10^{-5}$  Pa range. For such devices, we estimate the transition region to the viscous flow regime lies above 1 Pa, implying large dynamic range gauges should be possible.

Figure 3-3 shows preliminary results for a silicon nitride membrane mechanical damping gauge. We mechanically excite the membrane with a piezoelectric actuator and measure the energy ringdown time with a simple optical interferometer. We demonstrate a linear dynamic range of over two orders of magnitude, limited by excess dissipation of mechanical energy into the membrane mounting structure. Devices with optimized geometry and mounting should extent the dynamic range by several more orders of magnitude, as well by employing higher order mechanical modes of the membrane.<sup>52–55</sup> We find the slope sensitivity in the linear region of Figure 3-3 agrees with the prediction of Eq. 3.3 at the approximately 10% level, limited by our uncertainty in the membrane thickness and density.

### 3.4 Spectroscopic Technique for Measurement of Transient Pressure

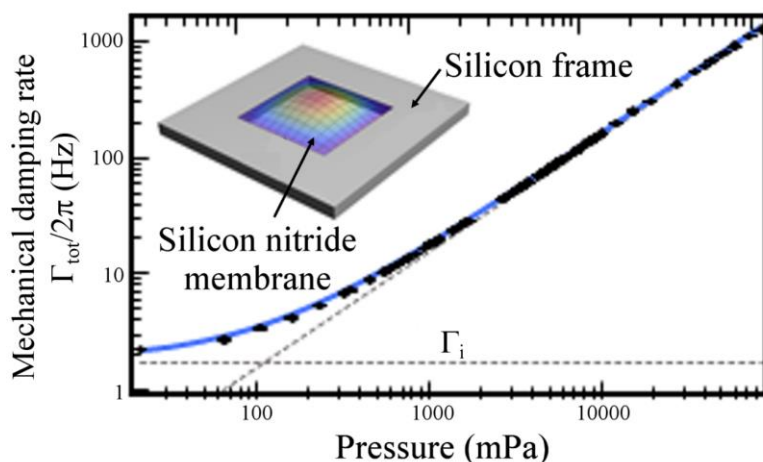


Figure 3-3: Silicon nitride mechanical damping gauge. The ringdown time for a 2 mm square by 50 nm thick, high-tensile-stress membrane is measure via piezoelectric actuation and optical detection. Inset shows fundamental out-of-plane vibrational mode.

As discussed throughout this manuscript, we are pursuing several methods to accurately measure static pressure from XHV to tens of MPa. However, there are no commercially available traceable calibration methods for the measurement of transient pressure. The measurement of transient pressure is important for many applications, perhaps chief among them is to understand the effect on the human brain of explosions or rapid accelerations such as in an automobile crash, which are expected to lead to better safety standards and equipment design. In our method, we rely on the traceability method outlined above, the unique quantum mechanical characteristics of the molecules are themselves the standard for pressure, making it consistent with the Quantum-SI.

The goal of recent European NMI's via EURAMET EMRP IND09 is to achieve traceable measurement of transient pressure using quantitative modeling of shock tube dynamics.<sup>56,57</sup> In contrast, our approach is to use independent molecular spectroscopy as a dynamic measurement of pressure, where the pressure itself is ascertained by measuring

time-resolved pressure-broadened spectra of CO molecules.<sup>58,59</sup> For our application, the shock tube is only used to produce a step change in pressure, i.e. act as a transient pressure source. From the linewidth and intensities of ro-vibrational transitions, pressure and temperature can be determined. For transient pressure measurement, our goal is to achieve an absolute uncertainty of 5% with a measurement rate of 100 kHz.

We have recently constructed and characterized a dual diaphragm shock tube that allows us to achieve shock amplitude reproducibility of approximately 2.3% for shocks with Mach speeds ranging from 1.26 to 1.5.<sup>60</sup> The agreement to 1-D modeling over this limited range is within a few percent and we believe a limiting factor in assessing the 1-D model is the inherent limitation of the piezo electric sensors used to determine Mach speed of the propagating shockwave. The large area sensors have spatial averaging effects which limit the accuracy in determining the time of the shock. Additionally, acceleration effects, temperature dependence, low resonant frequency, and over/under-shoot in these devices dominate the noise as one moves to high amplitude shocks. Figure 3-4 illustrates the piezo electric sensors response to a shock wave traveling at Mach 1.8. To overcome these challenges, we are developing phonic sensors that have extremely fast rise times (ns) and very small sensing area (100  $\mu\text{m}$ ).

In a proof-of-concept study we used our shock tube to characterize the dynamic response of photonic sensors embedded in polydimethylsiloxane (PDMS), a material of choice for constructing physical models of soft tissue. Our results indicate that the PDMS-embedded photonic sensors response to shock evolves over tens to hundreds of



microseconds time scale making it a useful system for studying transient pressures in soft tissue.

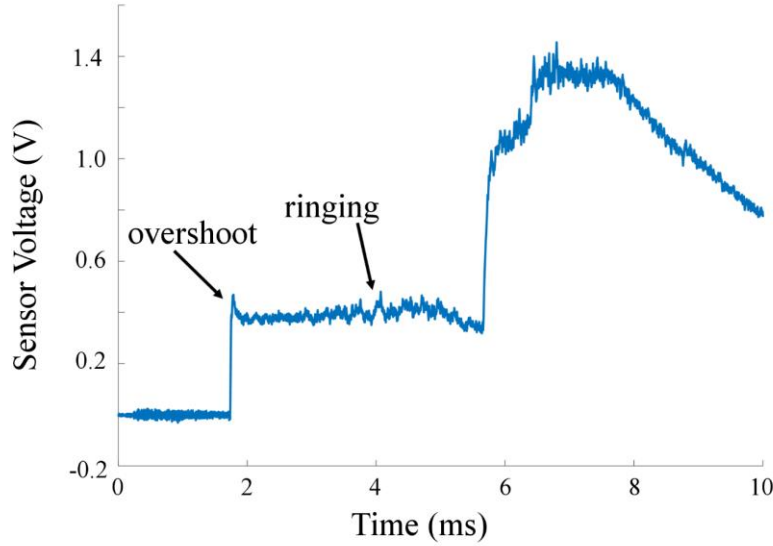


*Figure 3-4: Sample dynamic pressure data. The blue trace was recorded from a piezo electric transducer mounted perpendicular to the shock front. The Mach speed of the shock was measured to be 1.8. The initial conditions were 1.9 MPa and atmospheric pressure using Nitrogen on respective sides of the dual diaphragm.*

### 3.5 Refractometry for Pressure Metrology

We now turn our attention to the first of our active research projects in vacuum metrology at NIST. Several laser-based interferometer techniques are under study to interrogate the refractivity  $n - 1$  of a gas ( $n$  is index of refraction) which is a proxy for the gas density  $\rho_N$ , and ultimately the pressure  $p$  through the equation of state:<sup>61</sup>

$$p = k_B T \rho_N (1 + B_\rho \rho_N + C_\rho \rho_N^2 + \dots) \quad 3.4$$

where  $k_B$  is the Boltzmann constant,  $T$  is thermodynamic temperature, and the deviations from the ideal gas law arising from two- and three-body interactions are taken into account by density virial coefficients  $B_\rho$  and  $C_\rho$ . For helium gas, the virial coefficients in 3.4 are calculable through statistical mechanics at a level that contributes less than one part in  $2 \times 10^7$  to the uncertainty of pressures below 1 MPa.<sup>62</sup> Current state-of-the-art

thermodynamic thermometry implies that the thermal energy  $k_B T$  can be measured better than one part in  $10^6$ .<sup>63</sup> Therefore, with the highest accuracy measurements of helium refractivity, uncertainties from theory and thermodynamic temperature imply that the pascal can be realized with uncertainty at the one part in  $10^6$  level, which would place it competitive with state-of-the-art piston gauges at 1 MPa, and better than state-of-the-art mercury manometers at 100 kPa and below.

Depending on the details of these approaches, the techniques described herein result in a device that is considered alternately functionally-primary, primary, or a transfer standard. In all cases, two major obstacles must be overcome which are discussed below: The pressure-dependent index of refraction must be known to high accuracy, and any distortions in the measurement device must be accounted for. We begin with a brief discussion of the underlying physics before turning to a description of several experimental devices. The speed of light with frequency  $\nu$  in a gas,  $c$ , is reduced from that in an ideal vacuum  $c_0$  by a coefficient  $n$ , that is,

$$c = c_0 / n \tag{3.5}$$

The mechanism by which this happens concerns the polarizability of the particles constituting the gas. Such polarizabilities are the quantum basis of the method, and our ability to calculate the polarizability of helium and thus its refractivity is ultimately what makes the technique described herein a fundamental standard, consistent with the Quantum-SI. Theoretic determinations of these fundamental atomic properties were performed at relativistic and quantum electrodynamics (QED) levels.<sup>64</sup> Extending the method to gases other than helium is done in a ratiometric way that preserves the fundamental nature of the method.

The relation of  $n$  to  $\rho_N$  for an isotropic homogeneous medium is obtained by the Lorentz-Lorenz equation,<sup>65</sup>

$$\frac{n^2 - 1}{n^2 + 2} = \frac{1}{3\varepsilon_0} \rho_N \alpha = A_R \rho_V \quad 3.6$$

where  $\alpha$  is the dynamic polarizability of an individual molecule of gas in the volume,  $A_R$  is a virial coefficient, the molar dynamic polarizability, and  $\varepsilon_0$  is a fixed physical constant, the vacuum dielectric permittivity. Thus by determining index refraction, we can realize the molar density  $\rho_V$ . To calculate polarizability from first principles requires taking into account relativistic, QED, and finite mass effects<sup>64</sup> and this has been done for both the polarizability and refractive index of helium to an uncertainty of below one part in  $10^6$ . (note that for accuracy on the order of one part in  $10^6$ , it is also necessary to include the effect of magnetic susceptibility, which is omitted in Eq. 3.6 for simplicity.

Pressure sensors based on refractometry can in principle be based on any gas and He has the advantage that its pressure dependent index of refraction has been calculated to high accuracy, making such a device intrinsically absolute. However, in a practical device made of ultra-low expansion (ULE) glass, helium has the disadvantage that it is absorbed into the glass.<sup>64</sup> And so a refractometer using gases other than helium, such as  $N_2$ , may be a more useful method of pascal dissemination, but first the index of refraction of that measurement gas must be determined.

### 3.6 Practical use of refractometers as pressure standards

In this section, we will discuss how refractometers have been demonstrated to serve as pressure standards before finally discussing them as *primary* pressure standards. The concept of index of refraction is that a photon with a fixed wavelength will have a different frequency in the presence of gas than in a vacuum as described in Pendrill.<sup>66</sup>

This suggests an experiment in which one directs a laser down each of two channels, one filled with gas and the other evacuated, and measures the frequency change. This is done in the NIST FLOC. More precisely, a laser is wavelength-locked in resonance to a Fabry-Perot cavity, if gas density (i.e. pressure) changes, the servo adjusts the frequency  $f$  to maintain resonance with the cavity. Changes in  $f$  then give the index of refraction according to:

$$n - 1 \approx \frac{-\Delta f + \Delta m \left( \frac{c_0}{2L} \right)}{f} \quad 3.7$$

where  $\Delta f = f - f_0$  ( $f_0$  is the laser frequency in vacuum, and  $f$  is the frequency in the gas medium,)  $\Delta m$  is the change in mode order, and  $L$  is the length of the cavity. In practice, the laser frequency in Eq. 3.7 is never measured directly but is determined by measuring the difference in frequency between the measurement laser and a reference laser locked to the vacuum channel. Both the reference and vacuum channel deform under pressure. Much of the deformation is an overall compression due to finite bulk modulus, which is common to both the reference and measurement channels so that the effect largely cancels out. Another important effect is bending of the mirror surfaces in the reference channel due to the pressure differential across these mirrors. The measurement equation for pressure determined by the FLOC is then:<sup>67</sup>

$$p = \frac{1}{\left( \frac{3}{2k_B T} \right) A_R - d_m - d_r} \left( \frac{f_{vac} - f_{gas}}{f_{gas}} \right) \quad 3.8$$

where  $f_{\text{vac}}$  ( $f_{\text{gas}}$ ) is the frequency in the evacuated (gas-filled) cavity. The distortion term  $d_r$  is essentially the fractional change in length of the reference cavity when gas is added to the cavity (a negative number). Similarly,  $d_m$  is the negative of the fractional change in the measurement cavity length (a positive number, where the sign is an artifact of the derivation). For simplicity, in Eq. 3.8 we have only retained terms of order  $\Delta f/f$ . The correction for the distortion terms are approximately  $d_m \approx -d_r \approx 1.1 \times 10^{-11} \text{ Pa}^{-1}$ , whereas the index  $n$  varies with  $p$  by  $3.2 \times 10^{-10} \text{ Pa}^{-1}$  for helium at 303 K. Note that the two

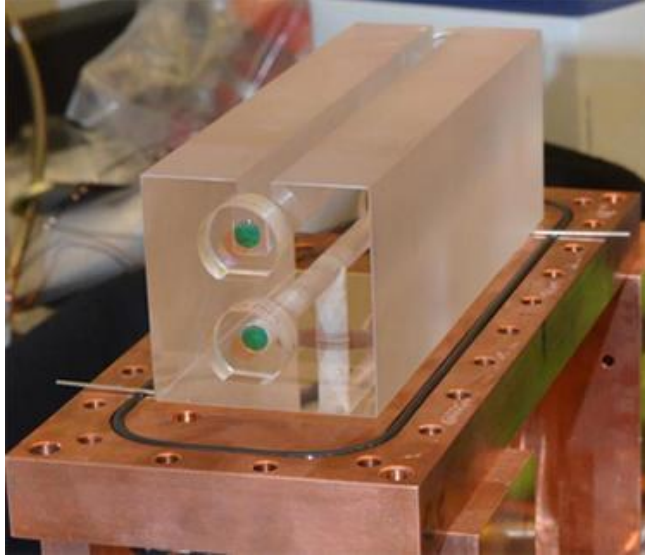


*Figure 3-5: Dual FP cavity refractometer shown with the thermal/vacuum apparatus removed: the upper channel is open to sense pressure, and the reference cavity is ion-pumped to high vacuum.*

correction factors cancel each other within 10%. Therefore, without any correction for the distortion, the FLOC is a primary standard for pressure to about 0.3%.

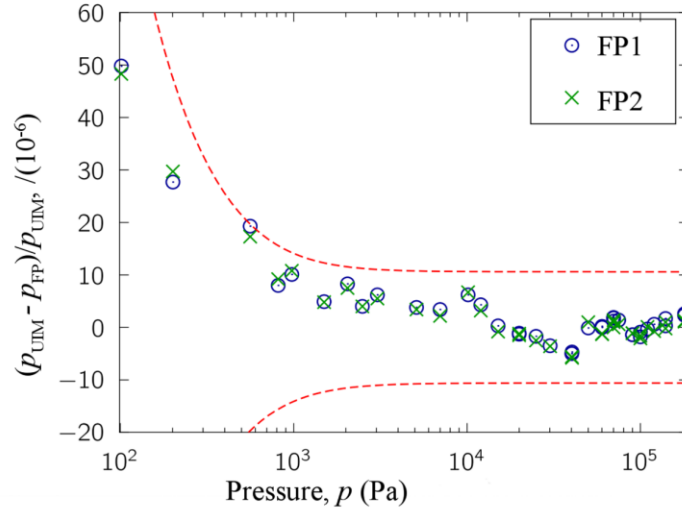


*Figure 3-6: Disagreement in pressure as measured by two separate laser refractometers (pFP) and mercury ultrasonic manometer (pUIM). The dashed lines are the manometer uncertainty. The figure is reproduced from P. F. Egan, J. A. Stone, J. E. Ricker, and J. H. Hendricks, Rev. Sci. Instrum. 87, (2016).*

Much improved performance can be achieved by measuring two or more different gases of known refractivity at a certain pressure. Both the cavity distortion and the absolute pressure can be determined, since measurements of two gasses provide two equations in the two unknowns. Helium refractivity is known as a function of pressure by calculation; at present, nitrogen refractivity has been measured.<sup>68</sup> When a measurement is made using two gasses, the FLOC provides traceability to primary methods and becomes functionally primary in the important sense that it never needs to be calibrated against a pressure standard. Thus, the invariant atomic/molecular properties of the gasses (i.e., refractivity) will serve as a practical functional standard for universal dissemination of the Pascal. In past work, the FLOC demonstrated

$((2 \text{ mPa})^2 + (8.8 \times 10^{-2} p)^2)^{1/2}$  expanded uncertainty as a transfer of the pascal, and so the

FLOC as a transfer standard of the pascal outperforms the manometer at pressure below about 1 kPa.<sup>67</sup>

### 3.7 Making refractometry-based vacuum standards primary

As described earlier, the FLOC is already a primary pressure standard when used with helium gas, but distortion of the optical cavity and mirrors, including dynamic effects caused by diffusion of helium into the ULE glass, limits the uncertainty to a level that is too high for many applications. Even if the measurement gas is nitrogen or some other species that doesn't diffuse into the glass, distortion still needs to be accounted for. What this means from a practical standpoint, is that to use a refractometer as a primary standard, we need to perform an excellent characterization of the distortion. At present, correcting for the distortion error in the FLOC device is being pursued by several different methods that are not first-order dependent on a measurement of pressure (and which thus preserve the primary-ness of the technique). These are outlined in turn in this section.

One early effort is shown in Figure 3-7, in which an optical technique is employed to find the laser beam location on the mirror surface, and the shape is calculated through a finite-element analysis. From this, a bending profile is extracted. By combining the bending profile with knowledge of the beam location, an estimate can be made of the distortion error in the FLOC. We have performed this procedure on two separate FLOC devices and found agreement within a relative uncertainty of  $7 \times 10^{-5}$  when compared with distortion determined by two-gas measurements (previous section). The approach appeared equally limited by how accurately the geometry and beam

location can be determined by the described imaging technique, and the 2% uncertainty in the elastic properties of ULE.

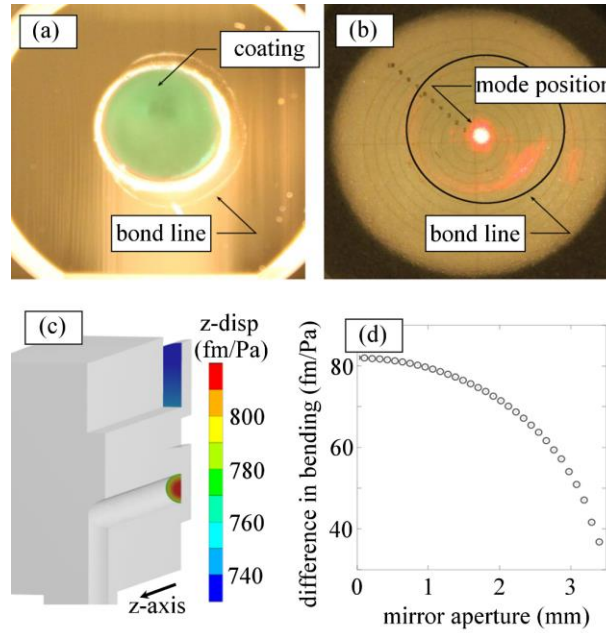


*Figure 3-7: Correcting FLOC distortion via finite-element analysis and an inspection of the mode position on the mirror. Pane (a) is an image of the mirror showing the bond interface. Through edge-detection, an estimate can be made of the area upon which the pressure acts. In (b), another image is taken with a laser beam aligned to the cavity resonance. By combining these two images, an estimate of the location of the beam on the mirror surface is made. The result of a finite-element analysis is shown in (c) datasheet values were used for elastic properties of ULE glass, and the geometry was estimated by the bond line in image (a). The difference in mirror bending calculated by finite-element is extracted as a profile, shown in pane (d).*

Another possibility would be to determine the elastic properties of the glass directly by mechanical means, using resonant ultrasound spectroscopy like that described in Schmidt et al.<sup>69</sup> Achieving relative uncertainty lower than one part in  $10^5$  in helium refractivity would require determination of the bulk modulus within 0.03%, which to our knowledge has not previously been demonstrated with glass. Additionally, doping inhomogeneities in ULE (i.e., giving rise to variations in the coefficient of thermal expansion) are a concern, in the sense that a sample of material whose elastic properties



are measured by mechanical means may not be an accurate reflection of the elastic properties of the FP cavity itself, even if taken from the same bulk piece of glass. (High-purity fused silica may be the better choice; our experience with sub-milikelvin thermal stabilization suggests that the higher thermal expansion of fused silica will not adversely affect low pressure performance.)

A further possibility is to use multi-wavelength interferometry and calculated dispersion of helium to determine the FLOC distortion. This can be accomplished by interrogating the FLOC with two laser frequencies  $\nu_1$  and  $\nu_2$  locked to the optical cavity, which has the advantage that it can be done *in-situ*. The measurement equation for pressure determined by the FLOC under these conditions to first order is:

$$p = \frac{1}{\delta\alpha} \frac{k_B T}{2\pi} \left[ \frac{\delta\nu_1}{\nu_1} - \frac{\delta\nu_2}{\nu_2} \right] \quad 3.9$$

Here  $\delta\alpha$  is the change in the atomic polarizability between the two laser frequencies at the same gas pressure  $p$ . Again, the atomic polarizability  $\alpha(\lambda)$ , where  $\lambda=c/\nu$ , is known for He from fundamental theoretical calculations. We see in Eq. 3.9 that the distortion terms that were present in Eq. 3.8 have cancelled and thus, using two lasers, we now have a primary FLOC. The main disadvantage to the two-laser method is that dispersion is a small effect compared to refractivity, particularly for Helium. For two practical laser frequencies, say 633 nm (HeNe laser) and 1550 nm (standard telecom wavelength), the difference in  $n-1$  is approximately  $1.6 \times 10^{-7}$  (at atmospheric pressure), which is more than 200 times smaller than the value of  $n - 1$ . Some sources of noise and systematic uncertainties will increase, and the current state of theory and calculation of helium dispersion would limit the approach to 5 parts in  $10^6$ . Efforts are presently underway at NIST to create a primary FLOC using this multi-color technique.

The last approach we discuss to solving the distortion problem, and thus making the refractometry technique fully primary, is perhaps the most obvious. The distortions which currently limit FLOC performance as a primary pressure standard can be avoided and/or corrected in refractometers of alternate design. One such design is the Monolithic Interferometer for REfractometry (MIRE).<sup>70</sup> One key feature of the apparatus is three interchangeable triple-cells of different length as shown in Figure 3-8: (a) MIRE apparatus and (b) Refractometry cells of three different lengths but which are otherwise nominally identical. Each borehole has a gas inlet and outlet. (Left to right, the cell lengths are 18 mm, 134 mm, 254 mm.) Figure is adapted from P. Egan, J. Stone, J. Hendricks, J. Ricker, G. Strouse, *Optics Letters* 42, No. 15, 2944 (2017)., but nominally identical geometries, material properties, and location of the laser beams through all windows. This feature is designed to make the window distortion common-mode in measurements of helium refractivity performed in cells of different lengths, and allowed us to cancel the error to 1.8%, which resulted in a 9.8 ppm relative uncertainty in the

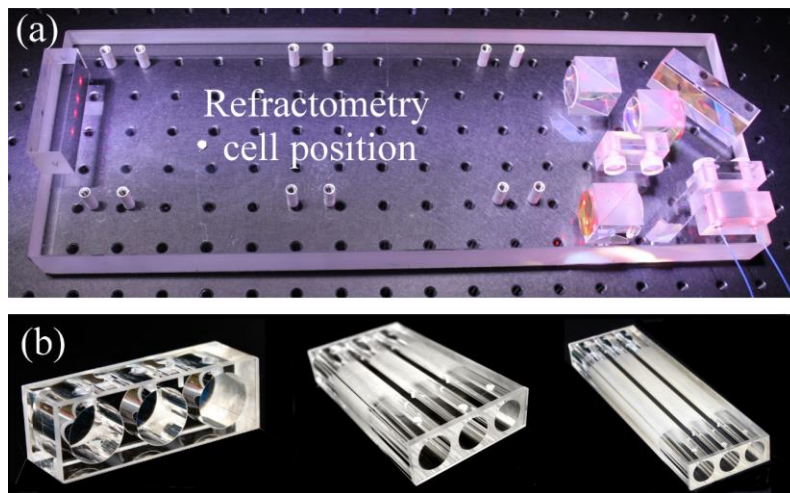


*Figure 3-8: (a) MIRE apparatus and (b) Refractometry cells of three different lengths but which are otherwise nominally identical. Each borehole has a gas inlet and outlet. (Left to right, the cell lengths are 18 mm, 134 mm, 254 mm.) Figure is adapted from P. Egan, J. Stone, J. Hendricks, J. Ricker, G. Strouse, *Optics Letters* 42, No. 15, 2944 (2017).*

refractometer. When the uncertainty in the refractometer was combined with the

uncertainties in the thermodynamic temperature of helium, gas purity, and the Boltzmann constant, our total standard uncertainty in this primary realization of the pascal was 11.7 ppm.

Another alternative refractometer design is a variable length optical cavity (VLOC).<sup>71</sup> The VLOC differs from the FLOC in that it measures a pathlength  $n \times \Delta L$  instead of  $\Delta n \times L$ ; which is to say, that one changes the geometric length of a FP cavity filled with gas at a constant refractive index of helium by about 15 cm instead of changing the refractive index inside a FP cavity of 15 cm constant length. The concept of translating a mirror to avoid pressure-induced distortion is not necessarily immune from spring-induced distortions, and the complications of motion and geometry errors are an engineering challenge. Some effort has been made to build a VLOC device, but since it is inherently difficult and other methods exist to solve the problem, this has been suspended.

### 3.8 Introduction to the Cold Atom Vacuum Standard

NIST is developing new a method for measuring and disseminating the pascal at the lowest pressures, the Cold-Atom Vacuum Standard (CAVS) which uses a cold atom trap to sense pressure.<sup>72</sup> Since the earliest days of neutral atom trapping, it has been known that the background gas in the vacuum limits the trap lifetime (the characteristic time that atoms remain trapped). We are inverting this problem to create a device that is both standard and sensor in the Quantum-SI paradigm. Because the measured loss-rate of ultra-cold atoms from the trap depends on a fundamental atomic property (the loss-rate coefficient, related to the thermalized cross section) such atoms can be used as an *absolute* sensor and primary vacuum standard. Researchers have often observed that the

relationship between the trap lifetime and background gas can be an indication of the vacuum level, and several research groups have pursued using cold atom traps as vacuum sensors.<sup>73–78</sup> However, an absolute vacuum standard, sufficient for use as an international quality standard, has not been realized before. To do this requires rigorous attention to all potential error sources, from both the atomic perspective and the vacuum perspective. Moreover, a primary CAVS requires the collision cross section between trapped ultra-cold atoms and the background gas, discussed below, to be traceable to an *ab initio* theoretical determination. This work is ongoing at NIST, and much progress has already been made, particularly for collisions of light sensor atoms and molecules. The topic of the CAVS is the main subject of this thesis, but before turning to it in detail, we need to discuss vacuum in more detail, not just how to measure it, but how to produce it.

## Chapter 4: Vacuum Preparation

In the previous chapter we discussed measurement techniques across all pressure ranges, with the promise of a deeper dive into the CAVS which operates at deepest vacuum. In this chapter, we discuss important considerations for achieving the excellent vacuum that the CAVS can measure. The ultimate (lowest) pressure of a high vacuum, ultra-high vacuum (UHV) or extreme-high vacuum (XHV) system results from a balance between the system pumping speed and gas input. In a well-built system free from leaks or permeation, the gas input is still nonzero, because gas is emitted from materials that comprise the vacuum chamber and system components. This is called outgassing. Practically speaking, achieving XHV pressures means using the biggest and best pumps available, and understanding and controlling outgassing. In this section we discuss the principles of hydrogen outgassing and how it can be mitigated through heat treatment (baking), and then describe three related projects: one in which we compared types of heat treatments, another in which we develop a method for performing heat treatments, and a third in which we investigate materials in conjunction with heat treatments.

### *4.1 Principles of outgassing*

During the production process of stainless steel—a commonly used material for vacuum hardware—a large amount of atomic hydrogen is dissolved in the bulk. This is important to consider since it is known to diffuse through the steel, eventually make its way to the surface, and release back into the vacuum as outgassing. So a post-process treatment must be performed to reduce the hydrogen concentration, depending on the ultimate pressure needed in the particular experiment.<sup>79,80</sup> For the UHV and XHV, outgassing rates in the range of  $10^{-10}$  to  $10^{-12}$  Pa L s<sup>-1</sup> are generally required. For untreated 300 series

stainless steel, the atomic hydrogen concentration is on the order of  $2 \times 10^{19} \text{ cm}^{-3}$ , corresponding to an  $\text{H}_2$  equivalent pressure of roughly  $4.1 \times 10^4 \text{ Pa}$  at  $23^\circ\text{C}$  (approximately 4/10 of an atmosphere).<sup>81</sup> This diffuses through the body of the steel and into the vacuum. Take an unbaked DN-40 flange, 13mm thick, made of 304 stainless steel. A typical diffusion constant for hydrogen in 304 stainless steel at room temperature is  $D = 3.24 \times 10^{-12} \text{ cm}^2/\text{s}$ , which results in a worst-case outgassing rate of  $1 \times 10^{-4} \text{ Pa L s}^{-1}$ , many orders of magnitude too high. Luckily, surface effects prevent the entirety of this gas load from reaching the vacuum, and the reservoir of H is eventually depleted as discussed below.

Water is a common contaminant as well, and is introduced to any system the moment it's exposed to air. In fact, during the evacuation of a stainless-steel chamber initially containing air at atmospheric pressure, the most abundant outgassing product is  $\text{H}_2\text{O}$  desorbing from the stainless-steel surface. Over time, the water outgassing rate in an evacuated system will decrease as the water desorbs from the stainless-steel surface and is pumped away. In a typical laboratory size vacuum system, outgassing fluxes of  $10^{-8} \text{ Pa L cm}^{-2} \text{ s}^{-1}$  are possible after several days of pumping,<sup>82</sup> corresponding to a base pressure of  $10^{-6} \text{ Pa}$  in a vacuum system with  $1000 \text{ cm}^2$  of surface area and evacuated with a  $10 \text{ L/s}$  pump. As the water outgassing rate reduces over time (typically as a power law), desorption becomes slower. To achieve lower water outgassing rates and lower base pressures, a vacuum bake for at least 1 day to 3 days in the temperature range of  $120^\circ\text{C}$  to  $150^\circ\text{C}$  is typically performed. This effectively removes most of the water on the surface of the stainless steel, and a total outgassing flux in the range of  $10^{-10} \text{ Pa L cm}^{-2} \text{ s}^{-1}$

to  $10^{-9} \text{ Pa L cm}^{-2} \text{ s}^{-1}$  can be expected.<sup>83</sup> Once reduced to this level, the predominant outgassing species in  $\text{H}_2$ .

Hydrogen atoms dissolved in the bulk stainless steel diffuse to the surface, recombine to form  $\text{H}_2$ , and subsequently desorb from the surface. They may also diffuse back into the stainless-steel bulk. If the hydrogen concentration in the bulk is high, the surface concentration of hydrogen will be high as well. In this case, nearly every H atom diffusing to the surface will recombine with another H atom, and the outgassing rate is thus governed by hydrogen diffusion through the bulk with no dependence on the surface reaction rate. The flux  $j_{\text{diff}}$  of hydrogen through the stainless-steel due to a concentration gradient is given by Fick's first law of diffusion:

$$j_{\text{diff}} = D(T) \frac{dc}{dx} \quad 4.1$$

The density of hydrogen in the steel is given by the concentration  $c$ , and the temperature dependent diffusion coefficient  $D(T) = D_0 e^{-E_D/k_B T}$ , where  $E_D$  is an activation energy. The reduction of the hydrogen concentration over time is given by Fick's second law of diffusion:

$$\frac{\partial c}{\partial t} = D(T) \frac{\partial^2 c}{\partial x^2} \quad 4.2$$

For stainless steel parts loaded into a vacuum furnace, we consider a slab of thickness  $d$  with vacuum on both sides ( $c = 0$ ). The solution of this equation with these boundary conditions has been discussed in many fundamental texts and papers on vacuum technology.<sup>79,81,84</sup> It yields an exponential time constant called the characteristic time  $t_d$  given by

$$t_d = \frac{d^2}{\pi^2 D(T)} \quad 4.3$$

This formula is only valid for diffusion-limited outgassing, it ignores surface recombination and assumes that all hydrogen reaching the walls will desorb. This assumption does not typically hold for real systems which tend to be dominated by surface effects, and for which pump down curves typically have a power-law dependence with time. Still, the formula can be used to predict the time required to reduce the bulk hydrogen concentration; a bake time of  $5t_d$  reduces the concentration by 99% in the diffusion-limited outgassing regime. Table II gives the characteristic time for 304 stainless steel of various thickness commonly found in vacuum components. These are calculated using Eq. 4.3 and the diffusion coefficient  $D(T)$  determined using  $D_0 = 1.22 \times 10^{-6} \text{ m}^2/\text{s}$  and  $E_D = 0.57 \text{ eV}$  from Grant *et al.*<sup>85</sup> Unsurprisingly, it is easily seen from Table II that thinner components degas much more quickly than thicker ones, and that increasing the temperature greatly reduces the time to degas components. Similar degas times are found for 316 stainless steel. Hydrogen can also permeate into the stainless steel from the  $\text{H}_2$  partial pressure in the background. As outlined in the appendix in Berg,<sup>86</sup> we use the diffusion and permeation coefficients from Grant *et al* to estimate that at a temperature of  $400^\circ\text{C}$  and a  $\text{H}_2$  partial pressure of  $1 \times 10^{-3} \text{ Pa}$ , the equilibrium hydrogen concentration is reduced by more than a factor of 5000 from that of typical unbaked stainless steel (3ppm as a fraction of weight).<sup>81</sup>



Table II: The calculated time needed to reduce the hydrogen concentration in 304 stainless steel by 99%. Various thicknesses of steel are given in the table, corresponding to those commonly used in vacuum chamber construction. The flange designations are defined in the standard document ISO 3669 (International Organization for Standardization).

Description	5t <sub>d</sub> (Days)			
	150 °C	375 °C	400 °C	425 °C
1.6 mm (1/16 in) plate	72	0.30	0.20	0.20
3.2 mm (1/8 in) plate	290	1.3	0.90	0.60
DN 16 (CF 1.33") Flange, 0.76 cm (0.3") thick	1700	7.4	5.1	3.6
DN 40 (CF 2.75") Flange, 1.3 cm (0.5") thick	4600	21	14	9.9
DN 63 (CF 4.5") Flange, 1.7 cm (0.68") thick	8500	38	26	18
DN 100 (CF 6") Flange, 2 cm (0.78") thick	11000	50	34	24
DN150 (CF 8") Flange 2.24 cm (0.88") thick	14000	64	44	31
DN 200 (CF 10") Flange, 2.5 cm (1.0") thick	17000	77	53	37
DN 250 (CF13.25") Flange, 2.84 cm (1.12") thick	23000	100	71	50
DN 200 (CF 10") Flange, 2.5 cm (1.0") thick	17000	77	53	37
DN 250 (CF13.25") Flange, 2.84 cm (1.12") thick	23000	100	71	50

As the outgassing rate is further reduced, the surface concentration is also lower and hydrogen atoms diffusing from the bulk to the surface will no longer combine to form H<sub>2</sub> with unit probability. In that case, outgassing will be recombination-limited instead of diffusion-limited, and the characteristic time will be longer than predicted by Eq. 4.3. It is difficult to give an *a priori* estimate of the characteristic time in the recombination-limited regime because it depends on surface details, and indeed a rigorous investigation of outgassing yields many complicating factors that make these rates hard to predict. For our purposes, it is sufficient to use the values in Table II as a guide.

It is well known, then, that vacuum system preparation requires baking to remove water, hydrogen, or other contaminants. Because the details of chamber geometry, material, manufacturing process, and handling are so widely variable, the principles

outlined above only serve as a starting point for developing a recipe to bake out a particular system. Certainly heat treatment is needed, but a researcher's understanding of how long and under what conditions has likely been informed more by her mentor's habits—which were in turn passed down from her mentor's mentor and so on—than by any definitive, evidence-based prescription. A wide variety of outgassing rates and fluxes for stainless steel can be found in the literature, often making direct comparison among various techniques difficult. Many variables may account for these differences. Surface conditions, roughness, welds, contamination, oxide layers, etc. play a role because the hydrogen must recombine at the surface before desorbing, and the desorption energy and recombination rate will depend on the surface. The history and treatment of the steel can greatly affect surface roughness and conditions. Furthermore, the sensors used in other outgassing studies are not always of the highest quality, and the resulting data can be corrupted by gauge non-linearity. Even if this weren't the case, comparisons can be difficult because the chambers used for these studies are often totally different sizes and shapes, and the geometry is not always easy to cancel in the analysis.

In the following subsections, we describe a series of experiments that were undertaken to develop best-practices for vacuum preparation. Subsection 4.2 examines the relative benefits of baking in vacuum vs air, subsection 4.7 describes a vacuum oven we designed and built to carry out bakes on a large number of parts, and subsection 4.10 is an investigation of different materials.

#### *4.2 Baking in air versus vacuum*

To discern whether it is better to bake in vacuum or in air, we used off-the-shelf vacuum components, assembled them into identical chambers, and subjected them to

either a medium temperature ( $\sim 400^\circ\text{C}$ ) vacuum bake or a medium temperature air bake.

This subsection follows Sefa et. al.<sup>83</sup>

304 and 316 series stainless steel are the most commonly used materials for construction of vacuum systems. Three types of baking schemes are commonly employed to degas hydrogen from stainless steel: Vacuum firing, in which the entire vacuum chamber is placed in a vacuum furnace operating at  $> 950^\circ\text{C}$  and pressures below  $10^{-3}$  Pa,<sup>25,79,87-90</sup> Medium heat treatment, in which the vacuum chamber is evacuated and heated to  $400^\circ\text{C}$  to  $500^\circ\text{C}$  typically with the outside of the chamber in air at atmospheric pressure;<sup>91-94</sup> and Air-bake, in which the vacuum chamber is baked entirely in air at atmospheric pressure at a temperature of  $400^\circ\text{C}$  or higher.<sup>89,90,94,95</sup> Vacuum firing is typically done on the order of hours; medium temperature and air-bakes can take days to weeks, depending on the geometry of the chamber. This is due to the exponential temperature dependence of the diffusion coefficient for hydrogen, as discussed in the previous section.

During air bakes, visible oxide layers form on the steel surface. These are mostly iron oxide, compared to chromium oxide which dominates the surfaces of unbaked steel, and are thought to affect outgassing in a couple of ways. They have a different diffusion coefficient than bulk steel, and therefore may present a diffusion barrier to the atomic hydrogen migrating through the bulk toward the surface, trapping it inside.<sup>79,95,96</sup> The different surface chemistry is also thought to promote a different hydrogen recombination rate, which could make it easier or harder to form  $\text{H}_2$  which must occur before it can be pumped away.

Our overall objective with the CAVS is to achieve UHV or even XHV pressures, so for this outgassing study, the goal was to understand how to achieve outgassing fluxes (or specific outgassing rate) of  $10^{-11}$  Pa L s<sup>-1</sup>cm<sup>-2</sup> or better, typically required for XHV. We sought the simplest techniques to produce the best outgassing rates. In this section we discuss an experiment in which these various heat treatments were compared.

#### 4.3 *Experiment details – chambers and treatments*

In order to understand the effectiveness of various baking techniques, we tested nominally identical vacuum “chambers” subjected to different heat treatments. The vacuum chambers are simply constructed from readily available vacuum components of standard size and flange type, all made from 304 series stainless steel. We chose to test medium heat treatment and air-bake because these are most practical. (We investigate vacuum firing to a lesser extent in another experiment, described in section 4.10 .) We constructed an apparatus that allowed outgassing rates of nominally identical chambers

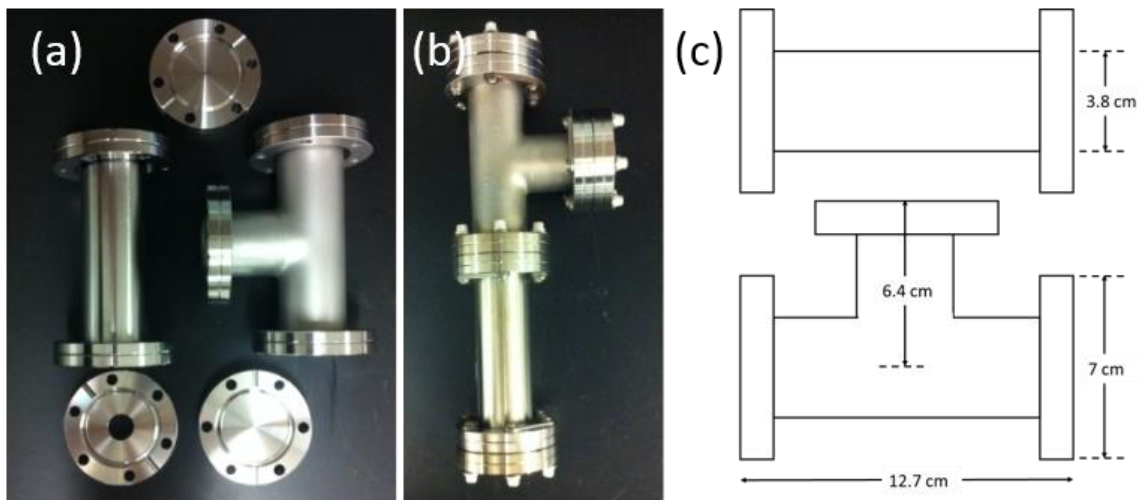


Figure 4-1: (a) standard vacuum components used to construct four identical chambers (b). The nominal dimensions are shown in (c).

with different heat treatments to be measured and compared under nominally identical conditions.

We constructed four simple, identical chambers like the one shown in Figure 4-1. The chambers have inner surface area of 350 cm<sup>2</sup> and a volume of 0.291 L (including a small volume associated with the valve, not shown). The chambers were cleaned with a neutral detergent solution in an ultrasonic bath (sonicator), rinsed and sonicated with deionized water, rinsed with isopropyl alcohol, and dried with nitrogen gas.

The chambers were designated as VAC1, LAIR2, DAIR3, and DAIR4, depending on their heat treatment. Chamber VAC1 was initially subjected to a medium heat treatment (under vacuum), chamber LAIR2 was subjected to an air-bake performed in the laboratory atmosphere, and chambers DAIR3 and DAIR4 were air- baked using clean dry volatile-organic-compound (VOC) free air. Chambers VAC1 and LAIR2 were initially prepared together: Chamber VAC1 was connected to an ultrahigh vacuum system and evacuated; chamber LAIR2 was placed next to the chamber VAC1 but was not evacuated and left exposed to the laboratory atmosphere. Both chambers were baked at 430°C for 15 days by surrounding both with a cylindrical oven. During the bake, chamber VAC1 was exposed to vacuum on the inside surface and to ambient air on the outside, whereas chamber LAIR2 was exposed to ambient laboratory air on both sides. After the bake, VAC1 was cooled and vented to air. The outgassing rates of both of these were measured before and after baking. Chamber VAC1 was then subjected to an air-bake using dry-air (explained below), for 24h at 430°C.

Chambers DAIR3 and DAIR4 were subjected to dry-air bakes only, for 48 h at 430 and 250°C, respectively. Both chambers were exposed to dry air on one side and to

ambient air on the other side during bake. Dry VOC-free air was continuously flowed into the two chambers during the bake, and continuously pumped by a rough pump throttled by a valve, thereby maintaining atmospheric pressure in the two chambers during the bake.

#### *4.4 Experiment details – measurement apparatus and method*

The experimental setup is shown schematically in Figure 4-2. Two sample chambers of volume  $V_1$  and  $V_2$  are connected to the apparatus measurement chamber of volume  $V_0$ , through valves X1 and X2, respectively. The volumes  $V_1$ ,  $V_2$ , and  $V_0$  were determined using an expansion method and are discussed in the next section. A spinning rotor gauge (SRG) attached to the measurement chamber was used to determine the outgassing rates by a rate-of-rise method. An isolation valve X0 separates the measurement chamber from a turbo-molecular pump, an ionization gauge (IG) and a residual gas analyzer (RGA). The apparatus is of all-metal construction, including the valve, with knife-edge seals and copper gaskets.

Before measuring the outgassing rate of a chamber, the system was continually pumped while baking at low temperature to remove water adsorbed on the system walls. The low-temperature bake was considered sufficient once the pressure as read by the ionization gauge was  $p < 1 \times 10^{-7}$  Pa, after which hydrogen outgassing measurements could commence.

First, we measured the outgassing from the isolated measurement chamber  $V_0$  (valves X1, X2, and X0 closed) by monitoring the pressure rate-of-rise on the SRG. The throughput of gas  $q_0$  due to outgassing is determined from:

$$q_0 = Q_0 A_0 = V_0 \frac{dp_0}{dt} \quad 4.4$$

where  $Q_0$  is the outgassing rate of the volume  $V_0$  with area  $A_0$  at temperature  $T$ .

After finding the background outgassing rate  $Q_0$  and throughput  $q_0$ , the entire system was again evacuated to a pressure  $p < 1 \times 10^{-7}$  Pa. Next, the outgassing throughput of the combination of the volumes  $V_1$  and  $V_0$  was measured using the rate-of-rise with the valve X0 and X2 closed. The outgassing throughput of the combined volumes  $q_{01}$  is given by:

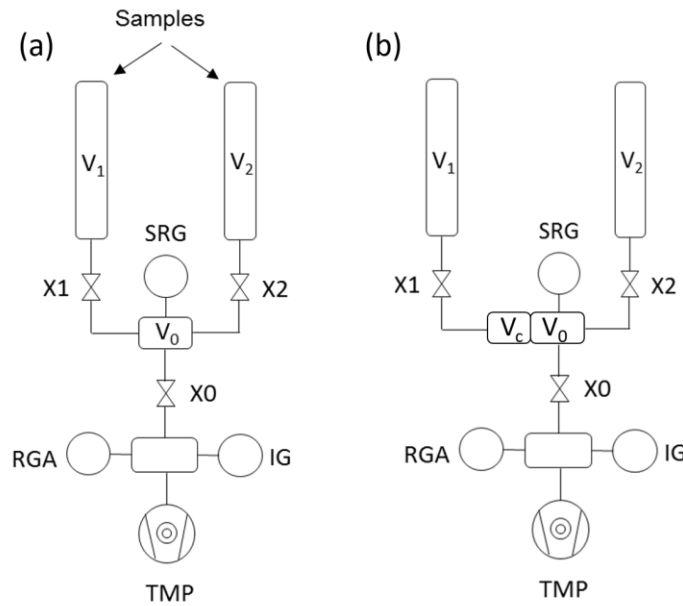


Figure 4-2: (a) Schematic of measurement apparatus used to determine outgassing rates of the sample chambers. Two identical sample chambers  $V_1$  and  $V_2$  can be mounted simultaneously. Pane (b) shows the same apparatus, but with known volume  $V_c$  attached to the measurement chamber.

$$q_{01} = Q_0 A_0 + Q_1 A_1 = (V_0 + V_1) \frac{dp_{01}}{dt} \quad 4.5$$

By combining equations 4.4 and 4.5, we can reduce the outgassing rate of volume  $V_1$  to:

$$Q_1 = \frac{1}{A_1} \left( (V_0 + V_1) \frac{dp_{01}}{dt} - q_0 \right) \quad 4.6$$

Note that the measured outgassing rate  $Q_1$  doesn't depend on the area  $A_0$ , it only depends on the volumes  $V_0$  and  $V_1$ , the measured rate of rise, and the area  $A_1$  of the sample

chamber. The combined type-B uncertainty of the outgassing rate is estimated to be 9% ( $k = 2$ ) with a reproducibility of 15%, so the total combined uncertainty of our measurements is 17% ( $k = 1$ ). The outgassing of the second sample chamber  $V_2$  is found the same way.

#### 4.5 Experiment details – determining the volumes

To find the volumes of  $V_0$ ,  $V_1$ , and  $V_2$ , we used a volume expansion method, in which the trapped gas in a known volume was allowed to expand into an unknown volume, allowing the unknown volume to be found ratiometrically. A nipple of known dimensions (found geometrically)  $V_C$  was attached to  $V_0$  and the combined volume was filled to a pressure with valve X1 closed and  $V_1$  evacuated. Valve X1 was subsequently opened so that the gas could expand into  $V_1$ , lowering the pressure. The ratio of initial to final pressures is then  $R_C = (V_0 + V_C)/(V_0 + V_1 + V_C)$ . The nipple  $V_C$  was then removed and the expansion repeated, this time allowing gas to expand from the volume  $V_0$  into  $V_0 + V_1$  resulting in pressure ratio  $R_0 = V_0/(V_0 + V_1)$ . Then we find the volumes  $V_0$  and  $V_1$  by:

$$V_0 = \frac{R_C - 1}{R_0 - R_C} V_C \quad 4.7$$

and

$$V_1 = \frac{(R_C - 1)(1 - R_0)}{R_0 - R_C} V_C \quad 4.8$$

We estimate that the determined volume uncertainty is 2% ( $k = 2$ ). All four chambers have equivalent volume  $V_1$ .



Table III. The measured volumes of the apparatus and sample chamber.

Chamber	Volume (L)
$V_C$	0.118
$V_0$	0.091
$V_1, V_2$	0.291

Table IV: Outgassing rates of the four sample chambers. Prior to the outgassing measurements, all of the sample chambers were exposed to laboratory air, evacuated, and then baked at 150°C for 72 hours. Outgassing rates were measured for chamber temperatures between 20°C and 21°C.

Sample Chamber	Heat Treatment	Treatment Temperature (°C)	Treatment Time (hours)	H <sub>2</sub> Outgassing Rate (Pa L/cm <sup>2</sup> /s)	Fourier Number $F_0$
VAC1	Before heat treatment	---	---	$1.65 \times 10^{-9}$	---
AIR2	Before heat treatment	---	---	$1.69 \times 10^{-9}$	---
VAC1	Vacuum bake	430	360	$1.77 \times 10^{-11}$	3.23
AIR2	Lab air bake	430	360	$1.19 \times 10^{-10}$	3.23
DAIR3	Dry air bake	415	48	$3.52 \times 10^{-10}$	0.35
DAIR4	Dry air bake	250	48	$7.33 \times 10^{-10}$	0.02
VAC1	Dry air bake	430	24	$1.04 \times 10^{-11}$	3.45

#### 4.6 Baking in air versus vacuum – results

Following the characterization of the volumes, outgassing measurements are simple with our setup. To gather rate-of-rise data, the SRG is monitored for a few hours or days. The pressure rise is expected to be linear, any deviations from linearity are taken as signs that something has gone wrong, such as a venting of the system that introduced water. The outgassing rate  $Q$  can then be computed using Eq. 4.6. Results are presented in Table IV,

along with the Fourier number, which predicts the relative reduction in hydrogen concentration in the bulk of the steel:<sup>97</sup>

$$F = \frac{4D(T)t}{d^2} \quad 4.9$$

where  $D$  is the diffusion constant given by  $D(T) = D_0 e^{(-E_D/k_B T)}$ ,  $d$  is the material thickness, and  $t$  is treatment time. We use values of  $D_0 = 0.0122 \text{ cm}^2/\text{s}$  and activation energy  $E_D = 0.57 \text{ eV}$  for 304 stainless steel from Grant et al.<sup>85</sup> The choice of  $d$  is somewhat arbitrary since it's common to all chambers and so doesn't affect a comparison, we choose flange thickness for  $d$ .

We measured outgassing rates before and after performing medium temperature heat treatments on two of the chambers, VAC1 and AIR2. The heat treatment improved the outgassing rate of chamber VAC1 by nearly 2 orders of magnitude whereas the laboratory air-bake only improved the outgassing rate of chamber AIR2 by about 1 order of magnitude. The outgassing rates we achieved using the medium heat treatment method are similar to the outgassing rate of  $2.4 \times 10^{-11} \text{ Pa L/cm}^2/\text{s}$  measured by Mamun et al. for a  $400^\circ \text{C}$  bake at 100 hours.<sup>93</sup> We estimate their Fourier number to be 0.06. Our longer bake time and thinner flanges did not produce a significantly better outgassing rate, suggesting that the reduction in the outgassing rate is not solely determined by a simple diffusion model. Hydrogen atoms must recombine to desorb from the surface, and for large values of  $F_0$ , the outgassing reduction may be limited by recombination and the presence of hydrogen traps.<sup>81,86</sup>

We then took VAC1 and performed an air-bake with the clean dry VOC-free air. The outgassing rate dropped by another factor of two. A Fourier number greater than 1

indicates that the outgassing rate is no longer in the diffusion-limited regime and the 24-hour bake was not long enough to significantly reduce the outgassing rate via diffusion through the stainless steel bulk. This suggests that the outgassing is recombination-limited, which is likely due to the oxide layer modifying the surface. Our result stands in contrast to Park et al.,<sup>92</sup> who did not see a significant difference between air bakes and medium temperature vacuum bakes. Bernardini et al. did a similar experiment, and found that most of the reduction of outgassing in an air-bake is due to hydrogen diffusion from the bulk.<sup>98</sup> Our result is not in conflict with theirs, but supports the complementary hypothesis that an oxide layer can reduce outgassing rates. We conclude that medium temperature vacuum bakes are required to achieve low outgassing rates, and that they can be further improved by a second bake in which one flows VOC-free bottled air through the chamber while baking. These air bakes can be difficult to set up and to control, and since medium temperature vacuum bake was sufficient to obtain the desired outgassing rate of  $10^{-11}$  Pa L/cm<sup>2</sup>/s, we will only do the latter on systems supporting the CAVS.

#### *4.7 Vacuum oven for baking*

Medium temperature bakes described in section 4.2 were deemed sufficient for our needs in developing the CAVS, so we now turn to the practical consideration of how to undertake these bakes at scale. To carry out low-temperature baking for water removal, one can usually get away with wrapping the apparatus in resistive heater tape and covering it with insulation and aluminum foil to help with uniformity. The heater tapes can be adjusted with a Variac, and temperature feedback can be as simple as a hand-held thermocouple reader. For achieving the lowest pressures, one must also address hydrogen removal, which requires elevated temperatures as described in section 4.1. It may be

possible purchase components made of low-outgassing materials (more on this in section 4.2 ) or to have a vendor perform high-temperature (400 °C or more) bakes in a vacuum furnace. The heater tape method is certainly feasible but has the disadvantage that flanges and seals are prone to leak at these temperatures. Additionally, temperature uniformity can be hard to achieve resulting in hot spots and cold spots (both of which may introduce problems), poorly insulated bakes can present danger to the user or nearby equipment, and in some cases, it's easily to accidentally overshoot the desired temperature, reaching temperatures in excess of 400 °C on some parts of an apparatus, potentially exceeding the component specifications. Sometimes it is desirable to bake components that will be placed into the system without necessarily baking the entire vacuum system every time. Because our apparatus is elaborate and consists of innumerable small parts, and to retain the ability to make design changes and iterations, our preference was to bake in-house but to avoid using the heater tape method, and to facilitate doing so, we designed a custom oven for this purpose.

This oven is separate from the vacuum system of interest, and was designed using a minimum number of seals, to reduce the probability of leaks. This section describes our custom oven, reproduced from Fedchak et. al.<sup>99</sup> We describe it's construction and operation (the interested reader is invited to consult the reference for outgassing measurements of the first component baked in this oven).

#### 4.8 Construction of the Vacuum oven

Our goal was to design a vacuum oven that could reliably be used for vacuum baking in the range of 400 °C to 450 °C. Because seals can easily leak when heated to these temperatures, our design has only one seal in the hot region. The oven diameter is large

enough to accommodate a component 50 cm long with a DN 350 flange (13.25 CF). The system also required a vacuum pump, a gauge to monitor the vacuum level during the bake, and temperature sensors for external monitoring and control. We also included two optional internal temperature sensors. The pumping system and gauges are located outside of the hot zone. A turbomolecular pump with a dry backing pump was used to maintain the system at  $10^{-3}$  Pa or below during the bake. Our vacuum oven easily maintains pressure below  $10^{-4}$  Pa at 450°C, allowing us to reduce the equilibrium hydrogen concentration by greater than  $5 \times 10^5$ . This maximal pressure also avoids accidental overload of the turbomolecular pump.

Figure 4-3, (a) – (d), depicts the oven chamber which consists of three main stages: a medium-temperature stage (i.e., the “hot zone”), a low-temperature (<150 °C) stage, and the pumping stage. The hot-zone can reach temperatures up to 450 °C during use, and the low-temperature stage is maintained to between 100 °C and 150 °C. This is to prevent water or other condensable gases from collecting on cold surfaces during the bake. The pumping stage is unheated.

The medium-temperature stage is a large vacuum chamber made of 316 stainless-steel, 3.2 mm thick, and consisting of a main chamber and a narrow tube section or “snout” which connects it to the pumping manifold. The main chamber lies entirely in the hot-zone. It consists of a cylinder with outer diameter (OD) of 35.6 cm on a 41.7 cm OD (16.5 CF) knife-edge flange sealed using a silver-plated copper gasket. The 16.5 CF flange is the only flange in the hot-zone and provides access for loading the oven. To make removing the 16.5 CF flange easier (even silver-plated copper gaskets may stick to knife-edge flanges when heated to 450 °C), four tapped through-holes were machined

into the blank flange between the existing bolt holes, and outside of the knife-edge, thus providing “jack-screws” such that a bolt driven into these tapped holes lifts the blank flange and opens the chamber. During our first several operations of the vacuum oven, three Belleville disc-springs were used as washers on each bolt. This was to prevent the bolts from loosening as the flange was heated. After several operations, many of the disc-springs showed a deterioration in their spring-constant. Instead of replacing these with new disc-springs, we added lock-washers. In either case, we have yet to experience a leak in the large flange seal. The snout has 6.4 cm OD and ends in a DN 63 (4.5 CF) flange. It is welded onto the oven chamber and lies partly in the hot-zone and partly in the low-temperature zone.

The low-temperature stage consists of a standard DN 63 cross connected to the large vacuum chamber on one end, and the turbomolecular pump on the other end. One port of the cross is used for a cold-cathode gauge capable of measuring  $10^{-1}$  Pa to  $10^{-9}$  Pa, the other port is a feedthrough for thermocouples. Two thermocouples, electrically insulated with alumina beads, are used to monitor the interior temperature of the chamber and the components within the chamber. These are optional to the operation of the oven but are an excellent check of the true temperature of the components under bake. A cold-

cathode gauge was chosen to monitor the pressure. These gauges tend to be more durable than hot-filament gauges, and gauge accuracy isn't critical in this application.

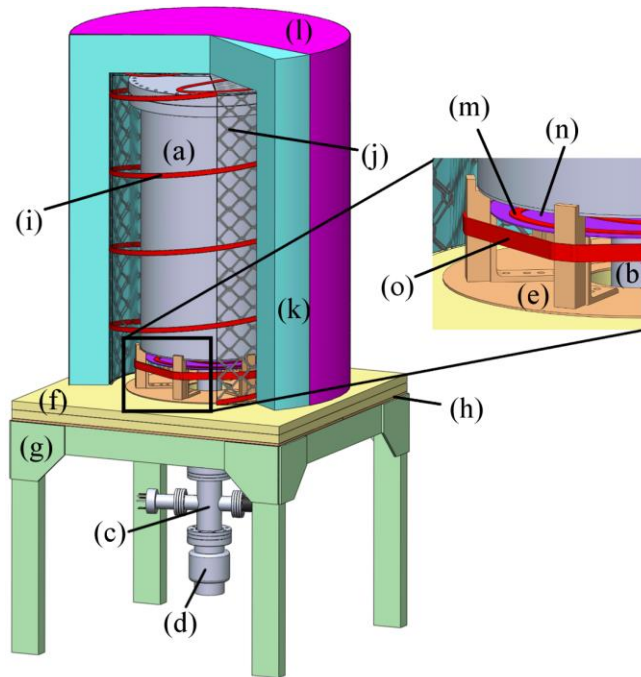


*Figure 4-3: Vacuum furnace system showing cutaway view of oven shell. (a) Hot zone main chamber, (b) snout, (c) low-temperature pumping stage, (d) turbo pump, (e) supporting plate and pedestals, (f) insulating boards, (g) table support, (h) table top, (i) main heaters  $\times 4$ , (j) heavy aluminum screen, (k) four-inch thick insulation, (l) foil outer shell, (m) bottom heater, (n) screen disk for bottom heater, (o) pedestal heater.*

The vacuum chamber is supported on 6 pedestals made of carbon steel. These sit on a circular carbon steel plate, 3.2 mm thick, with a 10.2 cm center hole that the snout passes through. Two 5.1 cm thick square slabs of ceramic fiber boards insulate the supporting plate from the table structure. The legs and cross supports are constructed from rectangular extruded aluminum hardware and the table top is a 6.4 mm thick carbon-steel plate. See Figure 4-3 (e) – (h).

The pumping system is shown in Figure 4-4 and consists of a 60 L/s turbomolecular pump backed by a dry scroll-type rough pump. A thermocouple gauge between the turbo-pump and rough-pump is used to monitor the backing pressure. We

also included a vent port to easily vent the system when the bake is complete. We included a valve on top of the rough-pump so that the rough-pump may be replaced during use. Once the chamber pressure is below  $10^{-4}$  Pa, the rough pump may be disconnected (to swap out for service) for several minutes without affecting the base pressure.

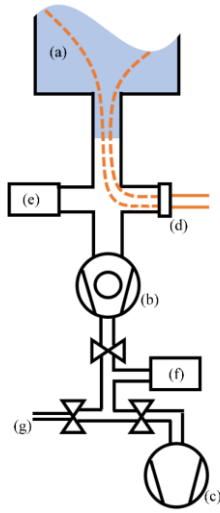


*Figure 4-4 Pumping system. (a) Main chamber and snout, (b) turbo pump, (c) dry scroll-type backing pump, (d) feedthrough for internal thermocouples, (e) cold-cathode high vacuum gauge, (f) thermocouple-type low vacuum gauge, (g) vent.*

The oven design is simple, inexpensive, yet effective. Heat is provided by fiberglass-insulated heat-cable (heater-tapes) rated to 750 °C. The hot-zone is heated by a total of 7 heater-tapes, each drawing about 300 W when powered. Four heater-tapes are wrapped around a cylindrical frame constructed of heavy aluminum screen which defines the oven shell. These are directly attached to the screen using steel wire. Each heater tape is paired with a thermocouple used to control the heater. These are also attached to the wire screen with steel wire. The sensing end is placed near, but not directly under, the heater tape, and does not touch the wire screen. A four-inch thick layer of ceramic fiber



insulation blanket surrounds the screen cylinder on the sides and top, secured with wire, and a layer of aluminum foil is wrapped around the insulation. This final layer is mainly to contain the insulation fibers and hold everything neatly in place. Figure 4-3(i)–(l) depicts the oven shell.

The bottom of the large portion of the chamber is heated by a heater tape wound to a washer-shaped aluminum screen. The screen disk has a slot cut into it so that it can be fit around the small part of the chamber. The screen disk is slightly flexible and shaped such that it can be held in place by being wedged between the supporting legs of the chamber, and that is all that is necessary to support it. We found that the single heater tape on the screen disk was not quite enough for the bottom of the chamber, therefore we wrapped a heater-tape once around the six supporting pedestals. Both of these heater tapes were controlled using the same thermocouple sensor, which was attached to the screen disk. See Figure 4-3 (m)–(o) for the bottom heater assembly. The portion of the apparatus between the turbo pump and the table-top (Figure 4-3 (b),(c)) was maintained between 100 °C and 125 °C during operation. We used custom designed heating boots for this, but conventional heater-tape wrapped around the components would have also sufficed.

Individual temperature controllers and type-K thermocouples were used to operate the four heater tapes on the main oven, and an additional controller and thermocouple operated both bottom heaters: the heater tape on the screen disk, and the heater tape on the pedestals. These individual controllers (Omega CN7223<sup>†</sup>) were

---

<sup>†</sup> Certain commercial equipment, instruments, or materials are identified in this paper to foster understanding. Such identification does not imply recommendation or endorsement by the National Institute of Standards and Technology, nor does it imply that the materials or equipment identified are necessarily the best available for the purpose.

integrated into a unit with transistors used as switched to drive a DC relay. A schematic is shown in Figure 4-5. When the transistor base-emitter junction is biased through a resistor, it acts like a saturated switch which effectively grounds the negative terminal of

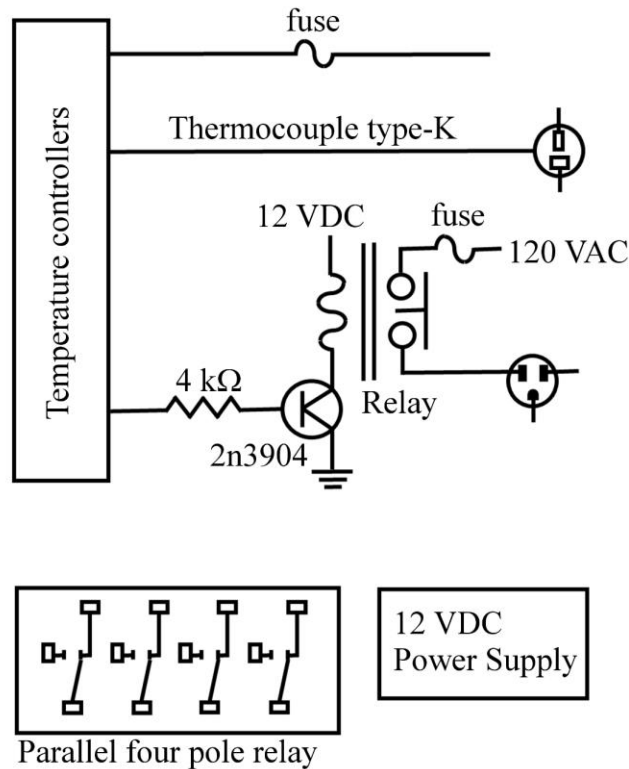


*Figure 4-5: Schematic diagram of a single temperature control unit used to drive a 120 V heater tape.*

the relay. The relay then becomes energized and this closes the contact to allow 120 Volts AC to energize the heater tape.

The transistor is required because the particular controller used was not capable of directly driving this relay, a different controller with a higher output current would obviate this need. The 12 VDC relay has four poles which are connected in parallel to improve the current capability and extend the life of the contacts under tight temperature regulation which results in rapid cycling of the current. Output fuses are added to protect the relay and heater tape in the event of an output overload (e.g. a short in the heater

tapes). We designed our control system to use 2.5 A fuses, and therefore all of the heater tapes used in the system were rated at  $\leq 2.5$  A.

#### 4.9 Operating the oven

The vacuum oven can be loaded and under vacuum in about 1 hour. We use a torque wrench to secure the 16.5 CF flange to the rated torque of 35.3 Nm. We typically allowed the oven to be evacuated overnight to reach a pressure below  $10^{-4}$  Pa before starting the heaters.

As the chamber warms, the pressure increases. After the final temperature is reached, the chamber base pressure will stabilize and eventually begin to drop. To keep the pressure below about  $10^{-3}$  Pa, we ramped the hot-zone temperature slowly, at a rate of  $5^\circ\text{C/h}$ . The low-temperature zone was heated much more quickly to about  $100^\circ\text{C}$ .

Figure 4-6 shows the pressure versus time for one of our 20-day bakes. The pressure steadily dropped over time, but after 20 days, the reduction rate was very slow. One method of determining bake times is to use the suggested times in Table 1, another way is to bake until the base pressure stops decreasing by a relevant amount.

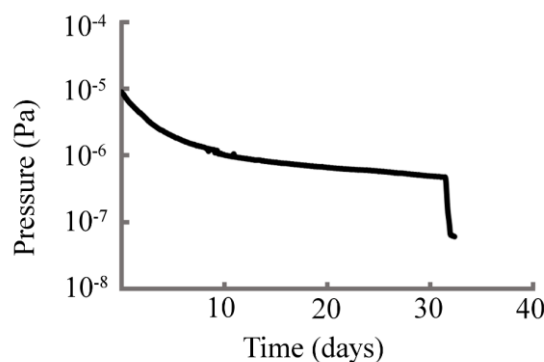


*Figure 4-6: Pressure vs time in the vacuum oven during one of our operations. The furnace was operated at  $425^\circ\text{C}$  from day 0 until day 30, after which it was cooled to room temperature.*

For our initial bake, in order to characterize the system and avoid any pressure or temperature anomalies, we controlled the ramp rate by manually adjusting the controller set points. Our first bake was with an empty chamber. This allowed us to debug our system with minimal risk. In addition, this allowed outgassing of the chamber itself before using it to bake other components. Subsequent bakes were computer controlled through an RS485 interface and LabVIEW software with controlled ramp rate. We have operated the vacuum oven without issue many times since the initial test. One of the components baked was a 28 mm gate valve, for which we achieved an outgassing rate of  $1.2 \times 10^{-9}$  Pa L s<sup>-1</sup>. If this valve were installed on a pump that had a pumping speed of merely 10 L/s, it would reach  $1.2 \times 10^{-10}$  Pa partial pressure.

#### 4.10 Investigation of materials in conjunction with heat treatments for vacuum

We've spent a great deal of effort to understand heat treatments for achieving low outgassing rates, but it is equally important to consider material selection. It is well-known that glass, for instance, doesn't outgas and is thus a great material for vacuum, if one can live with a delicate, brittle chamber (most experiments cannot). Other material properties are often important as well, some applications may require a material to be non-magnetic, and often cost is an important factor. In this section, which is reproduced from Fedchak *et al.*,<sup>100</sup> we focus on outgassing properties of a selection of metals commonly used for vacuum chambers: aluminum, titanium, and three different types of stainless steel, 304L, 316L, and 316LN. Chambers made of these materials were constructed with identical geometries by the same manufacturer (Anderson-Dahlen<sup>†</sup>) to facilitate comparison. In addition, chambers constructed of 316L and 316LN stainless

steel that were subjected to a vacuum-fire process of heating to approximately 950 °C for 24 hours. These two chambers are designated as 316L-XHV and 316LN-XHV. There is a reasonably large body of literature for outgassing rates of materials commonly used in vacuum,<sup>1-14, 81,83,106,107,91-93,101-105</sup> However, because of differences in materials, material treatments, and measurement techniques, published outgassing rates often vary and questions arise as to the outgassing rate practically achievable by an arbitrary user. Moreover, vacuum chambers have welds, seals, flanges, and variations in thickness and cleaning procedures that complicate the reproducibility of published outgassing rates. Because ours are made by a single manufacturer to a single design, and because we measured outgassing rates at NIST using SI-traceable measurement techniques, we are confident that the differences in outgassing rates we measured are due to the materials properties.

As mentioned before, UHV or XHV experiments typically require chambers with ultra-low specific outgassing rates of less than  $1.0 \times 10^{-11} \text{ Pa L s}^{-1} \text{ cm}^{-2}$ . Such a low outgassing rate cannot be achieved in stainless steel without heat treatment, generally at temperatures exceeding 400 °C<sup>93,92,83,99</sup>. Stainless steel is typically produced in an electro-arc process and, without additional refining processes that reduce hydrogen content, contains a high concentration of dissolved hydrogen. Aluminum contains far less dissolved hydrogen than stainless steel, and titanium has been shown to have a diffusion barrier to hydrogen that leads to low outgassing rates<sup>105,108</sup>. We will demonstrate that aluminum, titanium, and heat-treated stainless steel all have excellent ultra-low outgassing rates and can be used to build vacuum chambers capable of obtaining UHV or XHV pressures (i.e., pressures below  $1.0 \times 10^{-6} \text{ Pa}$ ).

As discussed in section 4.1 , any untreated vacuum chamber undergoes two distinct types of outgassing: that due to gases adsorbed on the surface (typically water), and that due to gases dissolved in the bulk (typically hydrogen). Water may be quickly desorbed from the surface by a low temperature bake in the nominal range of 100 °C to 250 °C. After such a low temperature bake, the outgassing products are predominantly hydrogen. (For chamber thicknesses exceeding 1 mm, bakes in this range even over many days will not significantly reduce the hydrogen outgassing that originates from gas dissolved in the bulk). We first determined the water outgassing rate as a function of time using a throughput method. Following a low-temperature bake, we then determined the hydrogen outgassing rate as a function of temperature using a rate-of-rise method. In both cases, the origin of the off-gassed products cannot be distinguished, i.e. the gas can desorb from the surface or originate from gas diffusing from the bulk material. The outgassing rate is the total throughput for the chamber and has units of  $\text{Pa L s}^{-1}$ . The outgassing rate per unit area, known as specific outgassing rate or outgassing flux, has units of  $\text{Pa L s}^{-1} \text{ cm}^{-2}$  and can be considered a material property.

Because it is relatively easy to perform a low-temperature bake, water outgassing is not a relevant consideration compared to the hydrogen outgassing rate for many UHV and XHV applications. However, low-temperature bakes are not always possible and long pump-down times can be required to reduce pressure. For example, for some very large vacuum systems, low-temperature bakes are prohibitively expensive so these systems may be baked once at most. Or the system may contain temperature-sensitive equipment and so cannot be baked at all. In these cases, the specific water outgassing rate or pump-down curve is an important consideration in vacuum design.

#### 4.11 Materials for Vacuum: Experiment

All chambers were made to be the same size, shape, and construction. They consist of a cylinder of 20 cm inner diameter and 20 cm interior length, open on one end and with 3 mm thick walls. A CF-type knife edge flange terminates one end of the cylinder and is sealed to a 13 mm thick DN200 flange using a copper gasket for all but the Al chamber, which used a gasket made of 1100-H14 series aluminum. The thickness of this flange is thinner than a standard DN200 flange to facilitate better degassing for the chambers that were vacuum fired. All interior surfaces were a standard machine finish of better than Ra (Roughness average) 1.6  $\mu\text{m}$ . The volume of the sample chamber is 6.3 L with an interior surface area of approximately 2000  $\text{cm}^2$ .

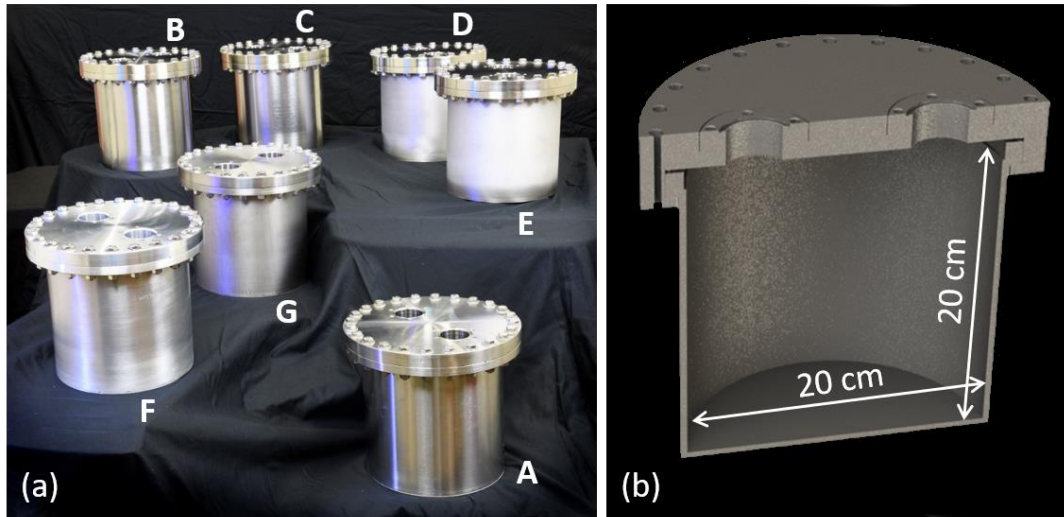
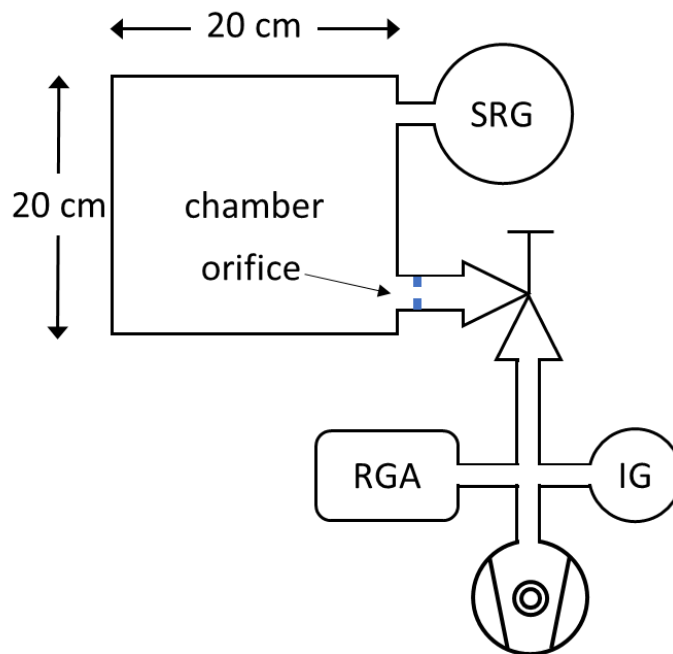


Figure 4-7: (a) Photograph of all sample chambers used in this study. These are (A) 304L, (B) 316L, (C) 316L-XHV, (D) 316LN, (E) 316LN-XHV, (F) Al, and (G) Ti. (b) cross section model view of a sample chamber.

The DN200 flange has two symmetrically placed DN40 ports, each located 5.7 cm from the flange center and 11.4 cm from each other. To one port is attached an all-metal valve and to the other is attached a spinning rotor gauge (SRG)<sup>49</sup>, note that the same valve and SRG were used for each chamber in turn. The interior surface of the SRG and the all-metal valve, up to the sealing surface, contribute to the outgassing rate during the rate-of-rise measurements; the combined surface area of the SRG plus valve represents less than 5% of the total area of the sample chamber. Both the all-metal valve and SRG were baked at greater than 400 °C for two weeks to reduce the hydrogen outgassing rate to avoid contaminating the results of this test<sup>83,99</sup>. The hydrogen outgassing rate of the combined SRG and all metal-valve were measured in a separate experiment and subtracted from the chamber outgassing results.



*Figure 4-8: Schematic of the apparatus used to determine the outgassing rates for the sample chambers. The water outgassing rates are determined using the throughput method and the hydrogen outgassing rates use the rate-of-rise method.*



To use the throughput method for measuring the water outgassing rate, it is necessary to have a flow-constricting element with known conductance through which the outgassed water flows before it is pumped away. We achieve this by using modifying a blank copper gasket (that is, a solid 2mm thick disk) to have a 6mm hole in the center. This blank gasket thus forms an orifice, which is installed between the chamber and the valve. The conductance of the orifice was determined from the dimensions to be 3.15 L/s for H<sub>2</sub>O at 25 °C, with a  $k = 2$  uncertainty of less than 1%. For the Al chamber, the orifice gasket was made of 1100-H4 aluminum.

#### 4.11.1 Materials for Vacuum: Outgassing Apparatus

A schematic of the outgassing apparatus is given in Figure 4-8. The sample chamber is pumped by a turbomolecular pump through the all-metal valve connected to the sample chamber; a dry mechanical pump backs the turbomolecular pump. An ionization gauge and an RGA are connected to the system between the turbomolecular pump and the all-metal valve. As described in the previous subsection, an orifice is between the all-metal valve and sample chamber, and an SRG is attached to the sample chamber. The SRG is used to determine the outgassing rates; the ionization gauge is only used to monitor the background vacuum level. Several platinum-resistance thermometers (PRTs) are attached to the chamber. The absolute calibrations of the PRTs are known to within 50 mK. To determine the outgassing rates as a function of temperature, a temperature-controlled enclosure is placed over the sample chamber, maintaining uniformity with gradients of less than 2 K.

The basic measurement procedure for determining outgassing rates is as follows: first, the sample chamber (soaked in room air) is attached to the all-metal valve in the

closed position. A dry pump backing the turbomolecular pump (not shown in Figure 4-8) evacuates the system up to the all-metal valve to a pressure  $p < 10$  Pa while the sample chamber remains at atmospheric pressure. The valve is then opened, and once the pressure above the backing-pump returns to 100 Pa or lower, both the SRG and the turbomolecular pump are started. Pressure in the sample chamber continuously drops as it is evacuated through the orifice. The time-constant for evacuating the chamber is a few seconds, therefore most of the gases that constitute room air are removed quickly. After about a minute, the remaining gas is mostly water desorbing from the chamber surface. As water desorbs from the chamber surfaces and is removed by the pumping system, both the water outgassing rate and the chamber pressure continue to drop. Vacuum level data (SRG) is continuously logged for up to ten days. By day ten, water is reduced, hydrogen becomes a significant portion of the gas off-gassed by the chamber, and the vacuum level recorded by the SRG changes very little because its signal is near the noise floor. The water outgassing measurement is terminated at this point (in many cases the data acquisition was terminated after only a few days for practical reasons).

Hydrogen outgassing rates are measured after the water outgassing measurement is complete. Before these beginning these measurements, the entire system is baked to between 125°C and 150°C for a minimum of three days to remove most of the remaining water. Afterwards, the sample chamber is allowed to re-equilibrate to laboratory temperature (maintained below 26 °C) and the SRG is turned on. Hydrogen outgassing rates are measured as a function of temperature. To reach temperatures above laboratory temperature, the temperature-controlled box is placed around the sample chamber.

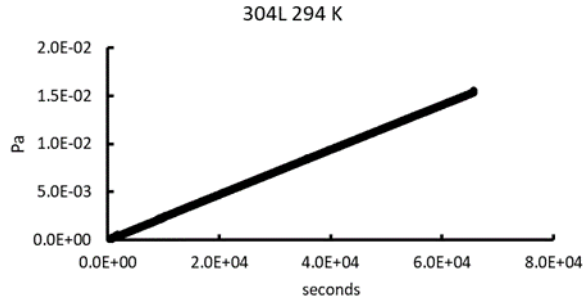


*Figure 4-9: An example of the rate-of-rise data used to determine the specific outgassing rate of the 304L chamber.*

Hydrogen outgassing is measured using a rate-of-rise technique. The vacuum level data produced by the SRG is continuously logged as a function of time throughout the entire process. The procedure begins with the all-metal valve open. The system temperature and pressure are monitored for stability. The all-metal valve is then closed and thus begins a hydrogen outgassing measurement. The pressure in the chamber rises with time, as shown in Figure 4-9. The valve remains closed for at least 4 hours and up to several days. Opening the valve ends the rate-of-rise measurement; outgassing products are quickly evacuated, and the pressure burst may be observed on the RGA.

Consider the outgassing data such as the example shown in Figure 4-9. A linear least-squares fit to the pressure vs. time data yields the slope  $\frac{dp}{dt}$ . The specific outgassing rate, or outgassing flux, is given by

$$Q_{H_2} = \frac{V \frac{dp}{dt} - q_0}{A} \quad 4.10$$

In Eq. 4.10,  $V$  is the volume of the sample chamber assembly (including the valve and SRG),  $A$  is the macroscopic surface area of the sample chamber interior taken from its

dimensions, and  $q_0$  is the background outgassing rate due the SRG and valve determined in a separate rate-of-rise measurement with no sample chamber and the SRG directly connected to the valve.

The relative uncertainty of  $Q_{H_2}$  is given by  $u_{Q_{H_2}} = \sqrt{u_V^2 + u_p^2 + u_{q_0}^2 + u_A^2 + u_{\text{type A}}^2}$ . All uncertainties reported here are given with a coverage factor of  $k = 2$  (95% confidence interval). The uncertainties associated with the chamber volume and area are  $u_V$  and  $u_A$  respectively, and are each estimated to be 4%. The term  $u_p$  is the uncertainty of the determined slope  $\frac{dp}{dt}$ , and is estimated to be 7% following Sefa et al.<sup>83</sup>; it is dominated by the uncertainty of SRG calibration factor for H<sub>2</sub>. The uncertainty of the background outgassing is  $u_{q_0}$  which itself is has a  $u_p$  component as well as a component due the uncertainty in the volume of the SRG plus valve; it is estimated at 12%. The type-A uncertainty  $u_{\text{type A}}$  is the uncertainty determined using statistical methods. The reproducibility of the measured  $Q_{H_2}$  is the dominant contributor to  $u_{\text{type A}}$  and the combined uncertainty  $u_{Q_{H_2}}$ . It is defined by the ability to reproduce the measured outgassing rate after the chamber has been vented, exposed to the atmosphere for some time. For  $Q_{H_2} > 1.0 \times 10^{-11} \text{ Pa L s}^{-1} \text{ cm}^{-2}$ , the reproducibility is 10%, whereas for  $Q_{H_2} < 1.0 \times 10^{-11} \text{ Pa L s}^{-1} \text{ cm}^{-2}$  the reproducibility is 70%. Real changes in the surface conditions may explain much of the large irreproducibility for  $Q_{H_2} < 1.0 \times 10^{-11} \text{ Pa L s}^{-1} \text{ cm}^{-2}$ ; however, measurement noise is also a significant contributor. The background  $q_0$  and SRG noise limit the measurable specific outgassing rate to above  $2 \times 10^{-13} \text{ Pa L s}^{-1} \text{ cm}^{-2}$  for data collection times on the order a day. In addition, the fundamental background signal of the

SRG (i.e. the residual drag) can have a frequency dependence that must be taken into account and can be another significant source of type A uncertainty for low signals.

Finally,  $u_{Q_{H_2}} = 24\%$  for  $Q_{H_2} > 1.0 \times 10^{-11} \text{ Pa L s}^{-1}$ , and  $u_{Q_{H_2}} = 72\%$  for  $Q_{H_2} < 1.0 \times 10^{-11} \text{ Pa L s}^{-1}$ .

Time-dependent water outgassing rates are determined using the throughput method. Prior to measuring water outgassing rates, the chambers are exposed to atmospheric conditions for long enough to saturate the surface with water; at least several days. Evacuation of the chamber begins by opening the all-metal valve with the rough pump operating. The measurement system is then turned on as quickly as feasible. Within the first minute after opening the all-metal valve to begin evacuation, the turbomolecular pump is started, the SRG is initiated and operated, and data logging is initiated. This is defined as  $t = 0 \text{ s}$ . Initially the SRG reading changes rapidly for two reasons: First, atmospheric gas is evacuated from the chamber in addition to water or other molecules desorbing from the chamber surfaces. Second, the SRG requires approximately 5 hours from initial suspension to come to temperature equilibrium with the chamber and produce a stable reading<sup>109</sup>. The rotor heats during the electromagnetic suspension causing the rotor temperature to rise; this heat slowly dissipates radiatively until the rotor temperature reaches equilibrium with the rotor chamber, causing the rotor diameter and hence its moment of inertia to change.<sup>109,110</sup> We arbitrarily cut the first 30 minutes of data, after which the majority of the gas in the chamber is due to desorption, although the rotor signal is still changing as it comes to temperature equilibrium. For the SRG used here, this effect results in an error in the SRG background reading that is approximately 7% low at  $t_3 = 2.0 \times 10^3 \text{ s}$ , 2% low at  $t_4 = 1.0 \times 10^4 \text{ s}$ , and negligible at  $t_5 = 1.0 \times 10^5 \text{ s}$ .

Pressure in the sample chamber is related to the gas throughput  $q$  through the orifice by  $q = (p - p_0)C$  where  $p_0$  is the pressure downstream of the orifice with conductance  $C$ . The pressure ratio, defined as  $R_p \equiv \frac{p}{p_0}$ , is estimated to be  $R_p = 5.8$  from an estimate of the effective pumping speed  $S$  downstream of the orifice and the conductance  $C$ . With  $Q = q/A$ , where  $A$  is, as before, the macroscopic internal area of the chamber assembly, the measurement equation for the specific outgassing rate of water using the throughput method becomes:

$$Q_{\text{H}_2\text{O}}(t) = \left( \frac{R_p - 1}{R_p} \right) \frac{p(t)C_{\text{H}_2\text{O}}}{A} \quad 4.11$$

In Eq. 4.11,  $C_{\text{H}_2\text{O}}$  is the  $\text{H}_2\text{O}$  conductance of the orifice and  $p(t)$  is the SRG pressure. A power-law of the form

$$Q_{\text{H}_2\text{O}}(t) = Q_0 t^{-\alpha} \quad 4.12$$

is fit to the data. The exponent  $\alpha$  is near unity and has been shown to be a function of the degree to which the system was exposed to water on venting, as well as the physical properties of the surface oxide layer.<sup>82</sup> The combined relative uncertainty in  $Q_{\text{H}_2\text{O}}$  is

given by  $u_{Q_{\text{H}_2\text{O}}} = \sqrt{u_p^2 + u_{C_{\text{H}_2\text{O}}}^2 + u_A^2 + \left( \frac{1}{R_p} \right)^2 u_{R_p}^2 + u_M^2 + u_{\text{type A}}^2}$ , where  $u_{C_{\text{H}_2\text{O}}} = 2\%$  is the

uncertainty in the  $\text{H}_2\text{O}$  conductance;  $\frac{u_{R_p}}{R_p} \approx 3\%$  is the uncertainty due the pressure ratio.

The uncertainty in the pressure reading  $u_p$  has three components: the uncertainty of the absolute pressure reading, the uncertainty associated with the error in the reading caused

by the rotor suspension as discussed above, and the uncertainty due to the residual drag or background offset of the SRG reading. Additionally, there is uncertainty in the pressure reading associated with the assumption that the gas is entirely water, this is accounted for in  $u_M$ , discussed below. Combined, these three components yield  $u_p(t=2 \times 10^3 \text{ s}) = 9\%$ ,  $u_p(t=1 \times 10^4 \text{ s}) = 19\%$ ,  $u_p(t=1 \times 10^5 \text{ s}) = 6\%$ . Both  $p$  and  $C_{\text{H}_2\text{O}}$  depend on  $\frac{1}{\sqrt{M}}$ , therefore the product  $pC_{\text{H}_2\text{O}}$  depends on  $\frac{1}{M}$ , where  $M$  is the atomic mass of the gas sensed by the SRG. After the first few minutes of pump-down when free gases are removed, water and hydrogen gas adsorbed on the surface constitute the majority of the gas left in the chamber. Initially the largest fraction is water, but because water is more easily removed, as the system is pumped for longer and longer times hydrogen gas begins to dominate. To estimate  $u_p$ , we assume 90% of the gas is  $\text{H}_2\text{O}$  at  $t=2000 \text{ s}$ , at  $t=10^4 \text{ s}$  50% is  $\text{H}_2$ , and at  $t=10^5 \text{ s}$  up to 90% is  $\text{H}_2$ . This yields  $u_p(t=2 \times 10^3 \text{ s}) = 1\%$ ,  $u_p(t=1 \times 10^4 \text{ s}) = 6\%$ ,  $u_p(t=1 \times 10^5 \text{ s}) = 10\%$ .  $u_A$  is the uncertainty due to the chamber area and is negligible compared to the other components.  $u_{\text{type A}}$  is the type A uncertainty and is taken from the reproducibility of the water outgassing rate; it is the dominant uncertainty component and is generally  $u_{\text{type A}} \approx 30\%$ . Finally, to estimate  $u_{Q_{\text{H}_2\text{O}}}$ , we take the root-mean-square average of the combined uncertainties at  $2 \times 10^3 \text{ s}$ ,  $t=1 \times 10^4 \text{ s}$ , and  $t=1 \times 10^5 \text{ s}$  to obtain  $u_{Q_{\text{H}_2\text{O}}} = 33\%$ .

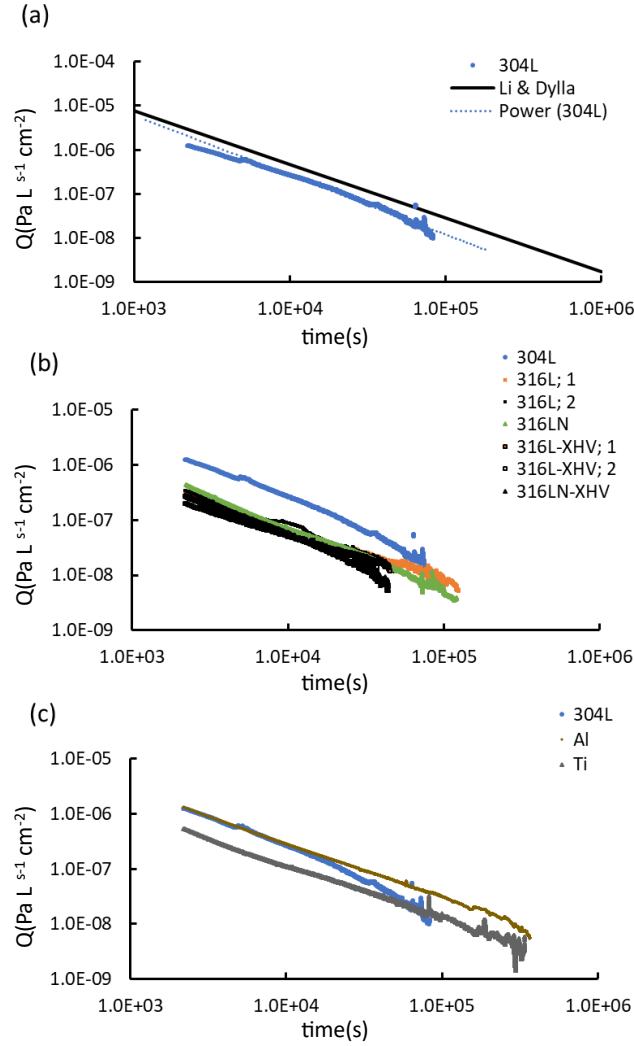


Figure 4-10: The measured specific outgassing rates for water,  $Q_{H_2O}$ , for all seven sample chambers, including repeats for 316L and 316L-XHV. (a) The present results for 304L compared to the results of Li and Dylla for chambers vented with air; (b) the present results for 304L compared to those of 316L, 316LN, 316L-XHV, and 316LN-XHV; (c) The present results for 304L compared to those of Ti and Al.

#### 4.11.2 Materials for Vacuum: Results for water outgassing

First we consider water outgassing. Measured water outgassing rates are shown in Figure 4-10. For comparison we include the water outgassing results from Li and Dylla<sup>82</sup> for 304L chambers exposed to ambient air in Figure 4-10 (a). This allows a relative



comparison among the present results to the benchmark results of Li and Dylla. The dotted line in Figure 4-10 (a) represents the power law fit of Eq. 4.12 to the 304L data. Results of the power law fit for all seven chambers are summarized in Table VI, along with the specific outgassing rates at three different times normalized to the those of the 304L chamber. Present results for the 304L chamber compare fairly well to the results of Li and Dylla; our results for  $Q_{\text{H}_2\text{O}}(t_3)$  are about 40% lower than those of Li and Dylla, and are a factor of 2.3 lower at  $t = t_5$ . Results for the 316 series chambers—316L, 316LN, 316L-XHV, and 316LN-XHV—all display lower initial outgassing rates than the 304L chamber. This is shown in Figure 4-10 (b). At  $t = 10^5$  s, the 316L and 316L-XHV chambers have between 50% and 70% lower outgassing rates than does the 304L chamber. Similarly, at  $t = 10^5$  s, the 316LN and 316LN-XHV chambers have between 20% and 40% lower outgassing rates than does the 304L chamber. The time-dependence in  $Q_{\text{H}_2\text{O}}$  for the 316LN and 316LN-XHV chambers are similar to that for the 304L chamber, as demonstrated by  $\alpha$  in Table V, but the 316L and 316L-XHV chamber seem to lose water at a slower rate.

Vacuum-firing does not seem to significantly affect the water outgassing. Neither the Al chamber nor the Ti chamber demonstrate significant practical advantage over 304L in terms of the outgassing rate at  $t = 10^5$  s: Ti is about 10% higher, which is within the measurement uncertainty, and the Al chamber is about 30% higher.

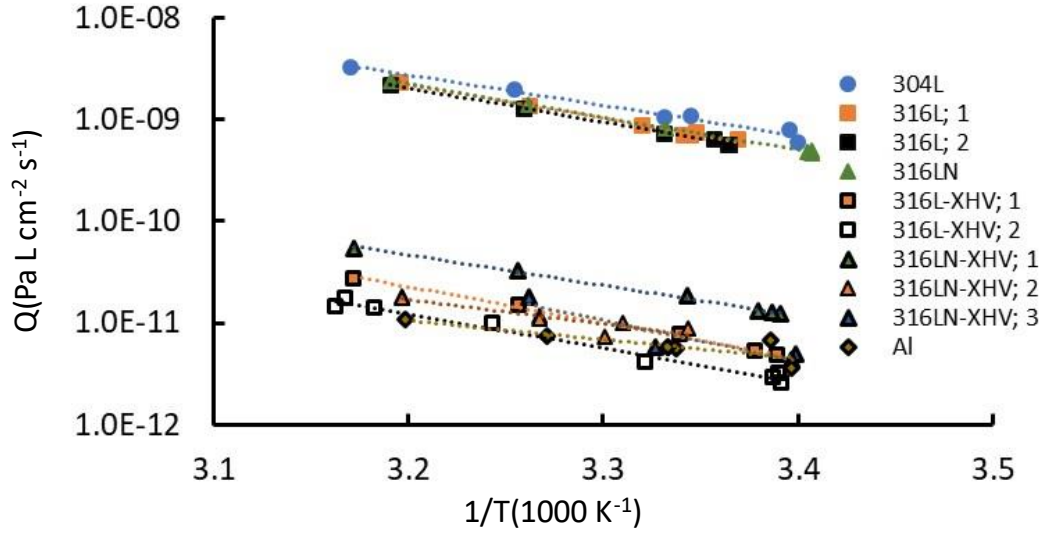


Figure 4-11: Arrhenius plots of the measured specific outgassing rate for  $H_2$ ,  $Q_{H_2}$  for six chambers.

Table V: Fit parameters  $Q_0$  and  $\alpha$  from Eq. 4.12. Given the fit parameters, the specific outgassing rate for water  $Q_{H_2O}(t)$  is calculated at three times:  $t_3 = 2 \times 10^3$  s,  $t_4 = 10^4$  s, and  $t_5 = 10^5$  s. The  $Q_{H_2O}(t)$  at these three times are also normalized to those of the 304L chamber.

Chamber	$Q_{H_2O}(t)$					$Q_{H_2O}(t) / Q_{H_2O}(t; 304L)$		
	$Q_0$	$\alpha$	$t_3$	$t_4$	$t_5$	$t_3$	$t_4$	$t_5$
304L	7.0E-02	1.3	2.4E-06	2.7E-07	1.2E-08	1	1	1
316L	2.5E-04	0.89	2.8E-07	6.6E-08	8.5E-09	0.1	0.2	0.7
316L	1.2E-03	1.0	4.1E-07	7.7E-08	6.9E-09	0.2	0.3	0.6
316L-XHV	1.3E-04	0.83	2.0E-07	5.2E-08	7.7E-09	0.1	0.2	0.6
316L-XHV	5.3E-04	0.99	2.6E-07	5.3E-08	5.4E-09	0.1	0.2	0.5
316LN	4.1E-03	1.2	5.2E-07	7.8E-08	5.2E-09	0.2	0.3	0.4
316LN-XHV	7.4E-03	1.3	4.2E-07	5.4E-08	2.8E-09	0.2	0.2	0.2
Al	4.2E-03	1.0	1.6E-06	3.2E-07	3.0E-08	0.7	1.2	2.5
Ti	1.3E-03	1.0	6.4E-07	1.3E-07	1.3E-08	0.3	0.5	1.1

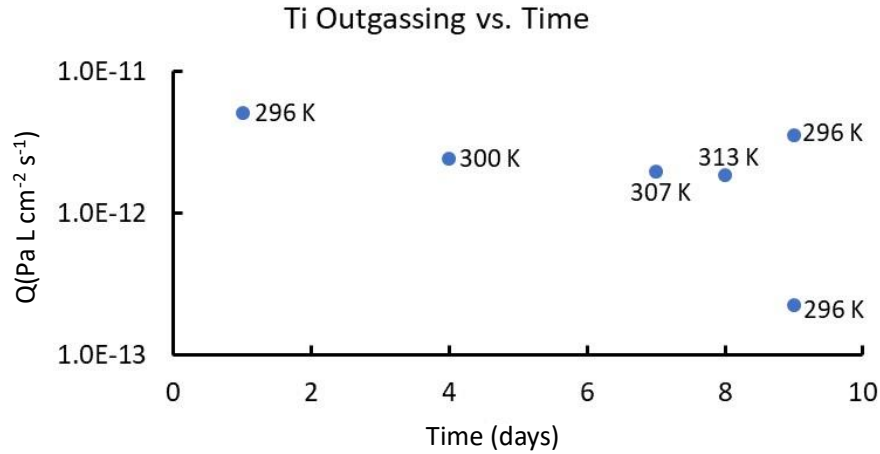


Figure 4-12: Plots of the measured specific outgassing rate for  $H_2$   $Q_{H_2}$  for Ti as a function of relative time.

#### 4.11.3 Materials for Vacuum: Results for Hydrogen Outgassing

Measured temperature dependent hydrogen specific outgassing rates are shown in Figure 4-12. In the limit of diffusion-limited outgassing, hydrogen outgassing originating from the bulk of the material may be described by

$$\log Q_{H_2} = \log A_0 - \frac{E_D}{k_B T} \quad 4.13$$

where  $E_D$  is an activation energy for hydrogen diffusion and  $A_0$  is related to the initial hydrogen concentration in the bulk of the material. Linear fits to the log of the outgassing data are displayed on all plots in Figure 4-11 and a summary of the  $E_D$  and specific outgassing rates determined from the fit at 25 °C is given in Table III. In cases where multiple data sets were taken, the average of all  $Q_{H_2}$  determined at 25 °C is given. The present  $E_D$  results for 304L and 316L are within 5% and 20%, respectively, of the benchmark results of Grant et al.<sup>85,111</sup>. For Ti, the specific outgassing rate given in Table VI is the average of all Ti data. The temperature dependence of the outgassing results for the Ti chamber did not follow the Arrhenius relationship. These are plotted as a function

of time in Figure 4-12, where  $t = 0$  is arbitrarily chosen as the time when the chamber bake was completed. The temperature of the chamber during the outgassing measurement is indicated by a label next to the data point. The general trend for the Ti chamber was that the outgassing rate decreased over time. This is not entirely surprising considering the studies done by Takeda and coworkers<sup>105,108</sup>. They demonstrate that the hydrogen concentration in Ti is largest in the boundary between the Ti bulk and oxide layer on surface, suggesting strong hydrogen traps in that region, but a much lower concentration of hydrogen in the surface oxide layer, suggesting a faster diffusion rate for hydrogen in the surface layer. These authors found that the oxide layer in Ti had much lower concentrations of hydrogen than the oxide layer in stainless steel. We speculate that in our experimental arrangement, hydrogen depletes from the Ti surface layer over a few days, reducing the outgassing such that it reaches the noise floor of the measurement. In Table III, for Ti we give the specific outgassing rate at 25 °C is the average of all the Ti measurements.

As can be seen from Table VI, ultra-low specific outgassing rates of  $Q_{H_2} < 1.0 \times 10^{-11} \text{ Pa L s}^{-1} \text{ cm}^{-2}$  are obtained from Al, Ti, 316L-XHV, and 316LN-XHV for  $T = 298.15 \text{ K}$ . As previously discussed, the repeatability of the outgassing measurements for  $Q_{H_2} < 1 \times 10^{-11} \text{ Pa L s}^{-1} \text{ cm}^{-2}$  is roughly 50%; therefore, results for the Al and the vacuum-fired stainless-steel chambers are equivalent to within the measurement uncertainty. For the Ti chamber, it is possible that there is re-absorption of the hydrogen on the Ti surface, and therefore the true outgassing rate may be larger than that measured using a rate-of-rise technique. Nevertheless, our results show that Ti is an excellent choice for many

XHV applications. Table VI also gives the outgassing improvement relative to 304L stainless steel.

*Table VI: Specific hydrogen outgassing rates  $Q_{H_2}$  at 298.15 K. For Ti,  $Q_{H_2}$  is taken as the average of all the Ti data. For the others,  $Q_{H_2}$  is determined from the fitting parameters  $A_0$  and  $E_D$  from Eq 4.13.*

	Activation Energy $E_D$		$Q_{H_2}(T=$ 298.15 K)	Relative improvement factor
Chamber	eV	K	Pa L s <sup>-1</sup> cm <sup>-2</sup>	
Ti			2.50E-12	295
Al	0.4	4251	4.70E-12	157
316L-XHV	0.7	8078	3.85E-12	191
316LN-XHV	0.5	6892	7.72E-12	95
316L	0.7	7583	4.93E-10	1.5
316LN	0.6	7445	5.39E-10	1.4
304L	0.6	6880	7.37E-10	1

We chose 304L as a benchmark because it is one of the most commonly used materials for vacuum chambers in the United States and, as the present study shows, produces a similar hydrogen outgassing rate as 316L or 316LN with no heat treatment. We see no improvement in the hydrogen outgassing between the chambers constructed of 316LN, which is produced by electroslag re-melt, over the chambers constructed of 316L. This is significant because 316LN tends to be a more expensive material than 316L or 304L, and so may not be the most economical choice unless the application requires materials with low magnetic susceptibility. The present results for Ti are in accord with previous outgassing measurements for Ti<sup>108,112</sup>, similarly, the present results for vacuum-

fired 316L are similar to or lower than outgassing measurement for vacuum-fired 316L found in the literature<sup>83,87,92,93</sup>.

#### *4.11.4 Materials for Vacuum: Summary*

We have compared the specific outgassing rates  $Q_{H_2}$  for seven chambers of identical geometry but of different materials and heat treatments: Al, Ti, 304L, 316L, 316LN, 316L-XHV, and 316LN-XHV. The chambers 316L-XHV and 316LN-XHV were vacuum fired at 950 °C for greater than 24 hours. Hydrogen outgassing rates were determined after a low-temperature bake between 100 °C and 150 °C for a minimum of 3 days. We found that Al, Ti, 316L-XHV, and 316LN-XHV all produced for  $Q_{H_2} < 1 \times 10^{-11}$  Pa L s<sup>-1</sup> cm<sup>-2</sup> and are excellent choices for UHV or XHV applications. Al, Ti, 316L-XHV, and 316LN-XHV show an improvement in outgassing of a factor of 150 over 304L, 316L, and 316LN. Ti showed the largest benefit, a factor of roughly 300 improvement over 304L. It is possible that some re-adsorption of outgassed hydrogen occurs on the Ti surface. We conclude that Al, Ti, 316L-XHV, and 316LN-XHV are all excellent choices for UHV or XHV applications. Material cost and properties would then be the factor in choosing among these materials. For example, 304L generally costs less than 316L but the 316L contains molybdenum and is more corrosion resistant and is typically used for vacuum-firing (as in this study) because it is regarded as more resistant to softening during the firing process. All the stainless steels have excellent structural and mechanical properties (machinability, weldability, etc.), but 316LN is the least magnetic and is used in applications that require non-magnetic steel, even though this alloy tends to be expensive. Al has the least expensive material cost compared to the other chambers studied here, and has an excellent strength-weight ratio, but practical chambers made of

Al can often be more expensive than those of stainless steel because of the difficulties of welding Al. Similarly, Ti tends to be an expensive material, and is more difficult to work with than stainless steel.

Water outgassing rates as a function of pump-down time were also determined for the seven chambers. The Al, Ti, and 304L chambers had similar water outgassing rates. The 316 stainless steels, 316L, 316L-XHV, 316LN, and 316LN-XHV, all started with lower water outgassing rates, about ten times lower than 304L at  $2 \times 10^3$  s, but the 316L and 316L-XHV do not show a significant improvement over the 304L chamber at  $10^5$  s. Interestingly, the 316LN and 316LN-XHV both showed a similar reduction in the water outgassing rate as a function of time to the 304L chamber, although the overall rate is about 10 times lower.

## Chapter 5: Overview of the CAVS

We turn our attention back to the Cold Atom Vacuum Standard, which was introduced in previous chapters. The operational premise of the CAVS is that an individual atom is knocked out of an atom trap when it undergoes a collision with a background gas molecule, and that measuring the trap lifetime is therefore a way to count background particles. The number of cold atoms  $N_c(t)$  in a trap decays exponentially due to these collisions,

$$N_c(t) = N_{0,c} e^{-\Gamma t} \quad 5.1$$

where

$$\Gamma = \rho_h \langle K \rangle \quad 5.2$$

is the loss rate and  $\langle K \rangle = \langle v\sigma \rangle$  is the thermally averaged loss rate coefficient. The subscript  $c$  indicates we mean the number or number density of *cold atoms*, which we must distinguish from *hot background particles* which are denoted by subscript  $h$ . In the UHV and XHV where the CAVS operates, the ideal gas law is an excellent equation of state to describe the background gas, and allows us to relate the pressure  $p$  to  $\Gamma$ ,

$$p = \frac{\Gamma}{\langle K \rangle} k_B T \quad 5.3$$

where  $\rho$  is the number density of the background gas,  $\sigma(E)$  is the total cross section for a relative collision energy  $E = \mu v^2/2$  and relative velocity  $v$ ,  $\mu$  is the reduced mass.

This naïve picture does a surprisingly good job of approximating the real behavior of the CAVS under the right conditions. That is, if we suppress other loss channels for trapped atoms so that we have a one-to-one correspondence between collision events and



ejections, and if we have a good understanding of the collision probability so that we can rigorously relate the number of collisions to the number of background particles, then indeed we have a fundamental measure of background gas density. We address these two issues in turn, following an introduction to laser cooling and trapping.

### *5.1 Fundamentals of Laser Cooling and Trapping*

The techniques for laser cooling and trapping of neutral atoms were developed in the 1980s. Here we provide a brief introduction for the non-expert, excerpted from Scherschligt et. al.<sup>72</sup> As stated above, the CAVS is based on trapping a cloud of cold atoms in a shallow, conservative trap (i.e., a trap where energy is conserved like an optical dipole trap or a magnetic trap) and measuring the rate at which background molecules eject cold atoms. The generation of a cold atomic cloud requires: (1) producing a vapor of atoms above room temperature, (2) laser cooling those atoms and (3) placing those cold atoms into the conservative trap.

Not all atoms are easily laser cooled. The most commonly used atoms in laser cooling are alkali-metal atoms, which exist as a solid metal at room temperature. To vaporize atoms into the vacuum chamber for laser cooling generally requires heating this metal to create an appreciable partial vapor pressure (typically  $10^{-6}$  Pa). For Li, this vapor pressure is only achieved at temperatures around 400 °C. Once an appreciable vapor of hot alkali-metal atoms is made, laser cooling techniques can be applied to cool and trap those atoms. Three concepts are needed to paint a general picture of laser cooling: (1) atomic energy levels are quantized, (2) light (or equivalently a photon) carries momentum, and (3) the Doppler shift. Figure 5-1 depicts an idealized, stationary, two-state atom with energies  $E_0$  and  $E_1$ . The resonant wavelength,  $\lambda_0$ , is related to  $E = E_1 -$

$E_0$  through Planck's constant,  $h$ , and the speed of light in vacuum,  $c$ , by  $E = hc/\lambda_0$ . If an atom at rest is exposed to this resonant light, it will absorb a photon (causing it to be excited to energy level  $E_1$ ). After excitation, it will emit a photon in a *random* direction and decay back to the ground state.

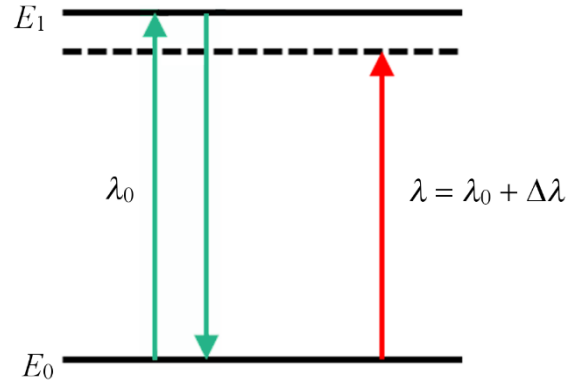


Figure 5-1: Schematic diagram of energy levels in a two-state atom, resonant photons  $\lambda_0$ , and a red-detuned photon  $\lambda$ .

Therefore, after one such cycle, the atom receives a net momentum kick in the direction of propagation of the light. The lifetime of the excited state  $\tau$  defines how often a momentum kick can be delivered to an atom, which is around 20 ns for alkali-metal atoms. This exchange of momentum between a photon and an atom at rest necessarily adds momentum to the atom. It is possible to employ the same physics to remove momentum from an atom in motion, thereby cooling it. To do this, one can exploit the Doppler effect to selectively change the velocity of atoms. In particular, if the atom has velocity  $v$ , the photons in the laser beam will be Doppler shifted with wavelength equal to  $\lambda' = \lambda \frac{c}{c-v}$  in the reference frame of the atom. By red-detuning the laser, one can ensure that only atoms with velocity toward the laser receive a momentum kick, slowing those atoms down. Atoms at rest and those moving in the same direction as the photons are

unperturbed. This is the fundamental basis of Doppler-cooling, which can be used in three dimensions with multiple laser beams creating an “optical molasses” to cool a cloud of atoms. The lowest temperature that can be reached in an optical molasses using this Doppler-cooling process is the Doppler temperature,  $T_D = \frac{\hbar}{2 k_B \tau}$ . This temperature is of the order of 0.1 mK for alkali-metal atoms.<sup>113</sup>

Laser cooling works quite well to reduce the temperature of atoms, but does nothing to confine them in space. To add spatial confinement, one exploits the Zeeman effect. For simplicity assume the atom has a ground state with quantized angular momentum  $J = 0$  and an excited state  $J = 1$ . If a magnetic field of strength  $B$  is applied, the atom’s energy levels split according to  $E = m_J \mu B$ , where  $\mu$  is the magnetic moment of the atom and  $m_J$  is the projection of  $J$  along  $B$ . If a magnetic field gradient is applied, the atom’s energy levels depend linearly on its position. Figure 5-2 shows our model atom from Figure 5-1, but with a magnetic field  $B$  that splits the  $E_2$  level into three levels. The figure also shows two lasers, one with right-circular polarized light (driving transitions to the  $m_J = +1$  state), and the other with left-circular polarized light (driving transitions to the  $m_J = -1$  state). If a slow atom moves into the region near  $z'$ , it will become resonant with the rightward going beam and be pushed back toward the center of the trap. In this way, the atom can be trapped spatially and cooled using the Doppler cooling technique described above. This is the magneto-optical trap, or MOT, which typically uses magnetic gradients of the order  $2 \times 10^{-3}$  T/cm.

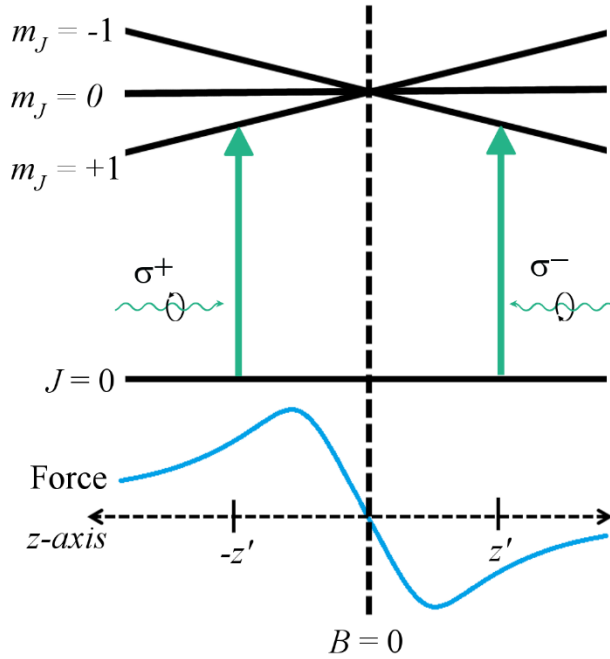


Figure 5-2 Principles of the magneto optical trap. (Top) Atomic energy levels as a function of position  $z$  in an applied magnetic field gradient with  $B = 0$  at  $z = 0$ . (Bottom) This results in a position-dependent force.

Once the atoms are cooled and trapped in a 3D MOT, they can be transferred to a conservative trap that is purely magnetic, by switching off the lasers and adjusting the magnetic field such that it has gradients at least an order of magnitude larger. In the ideal case, trapped cold atoms are only lost through collisions with background atoms and molecules. The trap is then said to have lifetime  $\tau_0$ . A discussion of non-ideal conditions that either lead to additional atom loss or prevent atom loss is discussed in Sections 5.3 and 7.2 of this chapter.

## 5.2 Estimating the loss rate coefficient

The background gas density  $\rho_h$  is what we're ultimately trying to determine, since it relates to pressure through the ideal gas law,  $p = \rho_h k_B T$ . So our goal is to make a measurement of  $\Gamma$  and combine it with a theoretically calculated  $K$  (recall  $\langle K \rangle = \langle v \sigma \rangle$  is

the thermally averaged loss rate coefficient, we drop the brackets for convenience). Many combinations of sensor atom species and background particle species are of interest to the vacuum community, some of which are calculable and some of which are not.

Semiclassical estimates of  $K$  based on published  $C_6$  or Casimir-Polder potentials have been carried out for a variety of systems, including  $\text{Li} + \text{H}_2$ , as well as other sensor atom species such as Na, K, Rb, and Cs, with a variety of background gas species such as He, Ar,  $\text{N}_2$ ,  $\text{O}_2$ ,  $\text{H}_2\text{O}$ ,  $\text{CO}_2$  and others.<sup>72,114</sup>

*Table VII. Estimated  $C_6$  coefficients in atomic units. Entries without references were calculated using the Casimir-Polder integral, for which we estimate a 10% uncertainty for the values. The coefficients do not depend on isotope to the accuracy given. Reproduced from Eckel et. al.<sup>115</sup>*

	Li (2S)	Li (2P)	Rb (5S)	Rb (5P)
$\text{H}_2^{116}$	83		160	
$\text{He}^{117,118}$	23		45	
$\text{H}_2\text{O}$	150	100	280	280
$\text{N}_2$	180	130	350	350
$\text{O}_2$	160	120	310	310
$\text{Ar}^{117,118}$	180		340	
$\text{CO}_2$	270	190	520	510

While these values are only estimates, an overall trend emerges in which there is little variation as a function of background gas species for all species other than hydrogen and helium, with  $K$  varying from about  $2 \times 10^{-9} \text{ cm}^3/\text{s}$  to  $3 \times 10^{-9} \text{ cm}^3/\text{s}$ , for hydrogen, the semiclassical estimate gives  $K \simeq 5 \text{ cm}^3/\text{s}$ . The variation of  $K$  with alkali sensor atom increases with sensor atom mass, i.e.  $K_{\text{Cs}} \simeq 1.5 \times K_{\text{Li}}$ . We are primarily concerned with using Li as the sensor atom in the CAVS, and the dominant background gas species for most systems is  $\text{H}_2$ , so in most realistic situations in deep vacuum, we get all the information we need from the *ab initio* calculations. In cases where other background

species are present, we must use a more accurate value for  $K$ , the estimates mentioned above are insufficient. As discussed in Scherschligt *et al.*,<sup>72</sup> we define a relative sensitivity coefficient

$$S_{GAS} \equiv \frac{K(GAS)}{K(H_2; ab)} \cong \frac{\Gamma_{GAS}}{\Gamma_{H_2}} \quad 5.4$$

so that a careful measurement of  $S_{GAS}$  combined with the *ab initio* calculations for the Li + H<sub>2</sub> system give a robust value for the loss rate coefficient of an arbitrary gas.

Measuring the sensitivity coefficients of a variety of gases requires an apparatus that enables measurement of loss rates of those gases at repeatable pressures. We can perform these measurements, which essentially amounts to verifying the calculated cross sections and measuring those we can't calculate, using a dynamic expansion technique discussed later, in section 6.6 . The pressures do not need to be known absolutely, so a calibrated pressure gauge is not necessary, and the technique remains fundamentally primary. This apparatus is based on a traditional technique for calibrating high-vacuum gauges in which a known flow is injected from a flowmeter into a dynamic expansion chamber. To adapt this technique to our needs, ultra-low outgassing materials are used in the construction so that it can reach outgassing flux rates less than about  $3 \times 10^{-12}$  Pa L s<sup>-1</sup>. These choices are motivated by our work as described in 4.10 and consist mostly of heat-treated stainless steel<sup>83,99</sup> with some titanium and copper (aluminum is avoided because it reacts with alkali metals).<sup>100</sup>

### 5.3 Other loss mechanisms and error sources in the CAVS

Now turning our attention to the issue of whether we have one-to-one correspondence between collisions and ejections, we must consider all possible ways to miscount collisions. The only realistic way we could undercount collisions is if the resulting energy

transfer from the background molecule to the trapped atom is insufficient to eject it from the trap. These so-called quantum-diffractive or glancing collisions are a function of trap depth and are a small percentage of losses from a shallow trap (a shallow trap is one for which the trap depth  $W$  obeys  $W/k_B \lesssim 1$  K, set by the diffractive energy scale which depends inversely on the total scattering cross section and the trapped atom mass).<sup>114</sup> Because that percentage can be accurately calculated, the associated uncertainty in the pressure measurement is small. Ways in which one could overcount collisions are more numerous, there are a number of loss channels in the trap due to effects other than collisions with background particles. In general, trap loss is described by the following differential equation where coefficients  $K$ ,  $K_2$ , and  $K_3$  describe trap decay due to single-body, two-body, and three-body loss respectively (where a *body* here is a sensor atom) in a trap with density  $\rho_c$

$$\frac{d\rho_c}{dt} = -K\rho_c - K_2\rho_c^2 - K_3\rho_c^3 \quad 5.5$$

Note that equation 5.1 is a solution when  $K_2 = K_3 = 0$  (two- and three-body losses are suppressed). In any case, the loss rate of interest  $K$  can be distinguished from  $K_2$  and  $K_3$  when fitting the data. Three-body loss is negligible for trapped Li at the temperatures ( $< 1$  mK) and densities ( $\sim 10^{10} \text{ cm}^{-3}$ ) relevant for the CAVS. Two-body loss is present in the CAVS due to evaporation, where two cold atoms elastically collide exchanging energy and causing one of the atoms to be ejected from the trap. Evaporation can be controlled by raising the trap depth relative to the temperature of the sensor atoms. Models of the evaporation process are accurate and can make the associated uncertainty negligibly small.

Our goal is to produce a primary standard as well as a sensor, which drives our decision about what kind of trap to use for the CAVS. For the ultimate, highest-accuracy measurements we use a pure magnetic trap to avoid complications arising from atom-laser interactions (for example, complications arising from the fraction of atoms in an excited state). In addition, the number of glancing collisions (and their associated uncertainty) is far smaller in magnetic trap ( $<1\%$ ) than for a MOT (approximately 50%), because the trap depth of a magnetic trap can be made arbitrarily small, whereas a typical MOT has a trap depth  $U/k_B \sim 1$  K. (Note that in many applications, the higher uncertainties associated with a MOT-based device are perfectly fine, and so we don't restrict ourselves to the magnetic trap in all cases.) As the CAVS is established in a pure magnetic trap, it may be possible to bootstrap to other trap technologies in similar devices.

But even in a magnetic trap, there are other losses to consider. Besides collisional losses, the CAVS could potentially have Majorana losses—a trapped atom may switch from a trapped state to an un-trapped state if it passes near a region in which the magnetic field is zero, such as the center of a quadrupole trap.<sup>119</sup> This is suppressed by using a magnetic field configuration that has no field zero—the Ioffe-Pritchard trap—though this loss channel cannot be eliminated completely and may represent non-negligible uncertainty at the lowest pressures.<sup>115</sup> The CAVS could also exhibit losses due to noise in the trap leading to heating (this can be suppressed somewhat by using low-density traps) or RF noise.



As a first-light demonstration, while the main CAVS apparatus was still under construction, we operated the CAVS MOT and used it to sense pressure (albeit in an incomplete apparatus with a configuration not optimal for testing). Since installing the coils needed for the magnetic trap, the CAVS-MOT is used to load atoms into the magnetic trap used for the CAVS. In Figure 5-3 (a) we show the decay of atom number trapped in the CAVS-MOT. At early times, we see the contribution from two-body loss

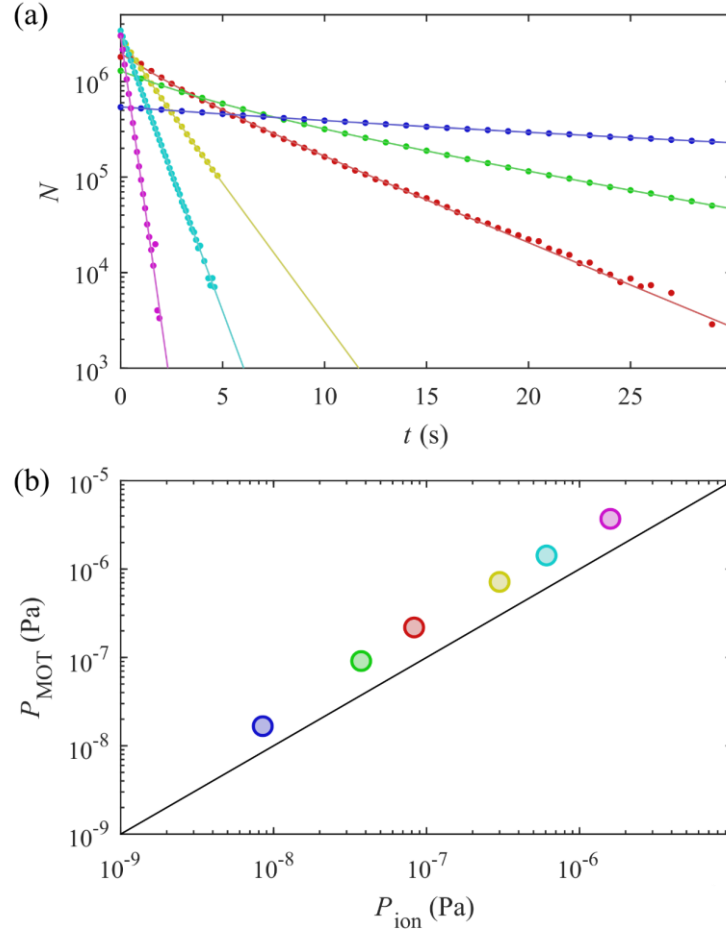


Figure 5-3: “First light” data. (a) Atom number decay in a magneto-optical trap (CAVS-MOT) data (circles) are fit to decay curves (solid curves) which are solutions to Eq. 14 and include single-body and two-body interactions. Panel (b): Pressure in the CAVS-MOT as determined by the data in panel (a) converted to pressure using semi-classical cross section estimates plotted versus an uncalibrated ion gauge.

(caused by light-assisted collisions) followed by exponential decay at long times. We separate the two mechanisms by fitting and extract the pressure from the exponential

decay. We compare the measured pressure to that measured by an ionization gauge, as shown in Figure 5-3 (b). The disagreement between the measured pressures is due to the following: First, the pressure in the chamber was produced by the outgassing induced by heating a Li source, rather than in a controlled way using an injected gas. Second, a significant pressure gradient existed between the ionization gauge and the CAVS-MOT. Third, the background gas composition was unknown, and could include significant portions of  $H_2$ ,  $N_2$ ,  $CO_2$ . Fourth, the trap was not characterized well enough to determine its depth. To analyze the data, we assumed the gas was  $H_2$  and took number of glancing collisions to be zero. Given the pressure gradients, we expect the ionization gauge to read lower than the CAVS-MOT, as shown in Figure 5-3 (b). Moreover, there is excellent linear agreement between the ionization gauge and the CAVS-MOT.

## Chapter 6: CAVS Experimental Design Details

In order to satisfy the demands of the metrological community, it is not enough to predict the foundational behavior of collisions between sensor atoms and the background particles of interest, it must be verified by measurement. We mentioned in section 5.2 that cross sections would be verified by comparison to a traditional vacuum metrology apparatus. In preparation for this comparison, we built the laboratory-scale CAVS because it was expected to have the best possible uncertainty, as well as a new version of the traditional Dynamic Expansion apparatus, purpose-built for these comparisons. In this chapter we will present the details of these apparatuses, before finally discussing the results in Chapter 8:.

### 6.1 CAVS Design

This section on the CAVS apparatus design is reproduced from Scherschligt et. al.<sup>72</sup> and refers exclusively to the laboratory-scale CAVS, as it was designed to have the lowest uncertainty and no compromises were made for practicality or ease of use. Figure 6-1 shows a cutaway view of the prototype CAVS apparatus. There are two distinct regions in the CAVS: a source stage and a sensing stage, which are separated from each other by a constriction which functions as a differential pumping tube. Because of the differential pumping tube's low conductance, there can be a significantly higher pressure in the source stage than in the sensing stage. In the source, alkali-metal atoms (Rb or Li) are vaporized using *in-vacuo* resistively heated alkali sources. These effusion sources produce a stream of atoms that travel through a cold shroud. Four lasers produce a MOT confined along two spatial dimensions (a 2D MOT) that's needle-like in shape. Because the sources are angled  $45^\circ$  in the axial direction, the atoms in the 2D MOT initially have

an average velocity toward the sensing chamber. This effectively produces a collimated beam of atoms. Two precautions are taken to ensure that only atoms redirected by the 2D MOT enter the sensing stage. First, alkali-metal atoms emerging from the source are not directly aligned with the differential pumping tube. Second, a cooling shroud, located in the vacuum, surrounds the 2D MOT and is maintained between -30 °C and -50 °C. Most atoms not cooled by the 2D MOT must strike the cold shroud at least once in order to scatter into the differential pumping tube. Because the sticking coefficient for alkali-metal atoms is near unity on metal surfaces, the probability of re-scattering into the sensing region is small. However, if a monolayer of Rb or Li accumulates on a surface, that coating will begin to emit atoms as an effusive source based on the saturated vapor pressure. To prevent re-emission of atoms from the shroud, we maintain the shroud at -30 °C , where Rb has a saturation vapor pressure on the order of  $10^{-9}$  Pa at 23 °C (The cooling shroud is not entirely necessary for Li because its vapor pressure is  $< 10^{-16}$  Pa at 23 °C).<sup>120</sup> The flux of cold atoms emitted from the 2D MOT is expected to be on the order of  $10^9$  atoms/s, and can be turned on and off simply by turning on and off the lasers of the 2D MOT.

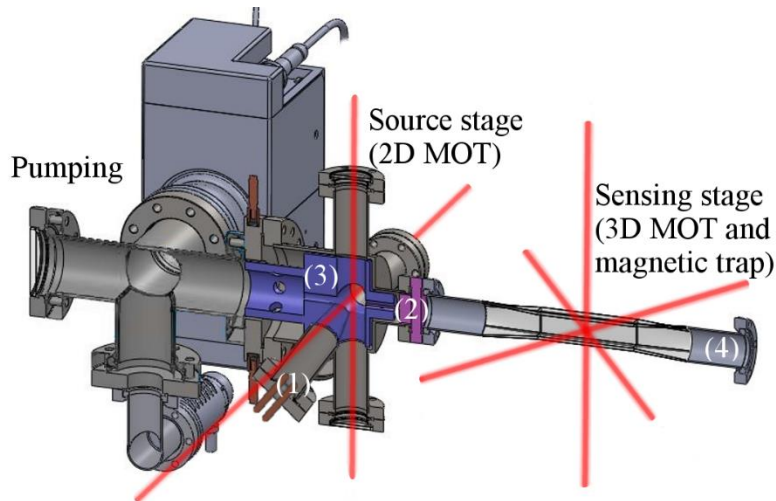


*Figure 6-1 Cutaway view of CAVS chamber showing the pumping region, the source stage, and the sensing stage. The alkali-metal atoms are injected by the (1) source which is angled to minimize contamination in the sensing stage while giving the atoms some initial momentum in the axial direction. A differential pumping tube (2) allows for lower pressures in the sensing chamber. The cooling shroud (3) increases the surface sticking coefficient and thus decreases stray alkali contamination. The vacuum under test attaches at (4). Red beams indicate lasers, magnetic field coils not shown.*

The atoms from the 2D MOT then pass through the differential pumping tube into the sensing chamber where they are captured into a 3D MOT. Here they are cooled to sub-millikelvin temperatures. The sensing chamber consists of a Pyrex glass cell surrounded by magnetic field coils. Six laser beams enter the cell along three primary axes. Once the atoms are trapped in a 3D MOT, the laser beams are extinguished and the magnetic field configuration is changed from a quadrupole-type field<sup>121</sup> to a Ioffe-Pritchard type magnetic trap (this is done by turning on additional coils).<sup>122,123</sup> The magnetic field geometry of the Ioffe-Pritchard trap is such that there is no field zero in the trapping region, which would otherwise lead to atom loss through Majorana loss.<sup>124</sup> The number of sensor atoms in the initially loaded magnetic trap is on the order of  $10^6$ , with a density of about  $10^{10}$  atom/cm<sup>3</sup>. Laser cooling is performed using circularly-

polarized laser beams. For the 2D MOT, four beams pass through optical quality viewports each attached to a vacuum nipple; for the 3D MOT, six beams pass through the glass cell. Not shown in Figure 6-1 are the magnetic-field coils that generate the fields required for the 2D MOT, 3D MOT, or magnetic trap. We do into more depth on the magnetic field design in the next section, 6.2 .

Once the atoms are in the magnetic trap they are sensing the background gas in the vacuum. The CAVS stage is connected to the vacuum system of interest via a vacuum port on the CAVS cell, shown on the right in Figure 6-1. The density of sensor atoms in the magnetic trap is determined by absorption imaging of the ultra-cold atomic cloud in the trap. Collisions between the background gas molecules and the trapped sensor atoms will eject cold atoms out of the trap, necessarily reducing the density  $\rho_c$  in the trap according to  $\rho_c(t) = \rho_c(t = 0)e^{-\Gamma t}$  (the solution to the one-body term of equation 5.5). The loss rate  $\Gamma$  is extracted from the exponentially decaying density and is related to the background gas number density  $\rho_h$  by equation 5.3,  $\rho_h = \frac{\Gamma}{k_{loss}}$ . Only the relative change in number density of the cold sensor atoms is necessary to determine  $\Gamma$ ; knowledge of the absolute atom number is not.

## 6.2 Magnetic Field System

Our magnetic field coils are Bitter-type electromagnets. Our coils assemblies enable us to produce multiple field configurations including uniform magnetic fields, spherical quadrupole traps, or Ioffe-Pritchard (IP) magnetic bottles. Unlike other designs, our coil allows both radial and azimuthal cooling water flows by incorporating an innovative 3D-printed water distribution manifold. This discussion describes work done by colleagues in Siegel *et. al.*<sup>125</sup> As with any magnetic field coils, the maximum field is

limited by the maximum current the coils can withstand. This in turn is limited by heating, or more precisely, the rate at which heat can be removed from the coils. The simplest approach to mitigating this problem is to use water-cooled electromagnets made from wound copper tubing. In such coils, the hydraulic resistance increases linearly with the winding length. To increase current density in the coil, flow channels are generally made as small as possible, further increasing the hydraulic resistance and reducing the flow, limiting the total cooling performance. A number of coil geometries have been proposed to optimize thermal and magnetic performance. Our design is comprised of non-concentric Bitter coils, necessitating a complicated cooling water circuit, which has only recently become possible to make through the advent of 3D printing.

Our coil assembly can generate multiple field configurations, including uniform fields along the symmetry axis  $\hat{z}$ , and spherical quadrupoles. Of particular interest for the CAVS, our coil assembly can generate an IP trap, which creates a non-zero local magnetic field minimum and is given by

$$\mathbf{B} = B_0 \begin{bmatrix} 0 \\ 0 \\ 1 \end{bmatrix} + B' \begin{bmatrix} x \\ -y \\ 0 \end{bmatrix} + \frac{B''}{2} \begin{bmatrix} -xz \\ -yz \\ z^2 - \frac{1}{2}(x^2 + y^2) \end{bmatrix}. \quad 6.1$$

To create this configuration, our assembly features three independent coil pairs: A pair of “curvature” coils creates  $B''$  with an offset that contributes to  $B_0$ , A pair of Helmholtz coils or anti-bias coils that opposes the contribution to  $B_0$  from the curvature coils, and a pair of quadrupole coils (clover coils) that creates  $B'$ . Figure 6-2 Rendering of Bitter coil assembly. The 3D-printed water distribution manifold is white, a section has

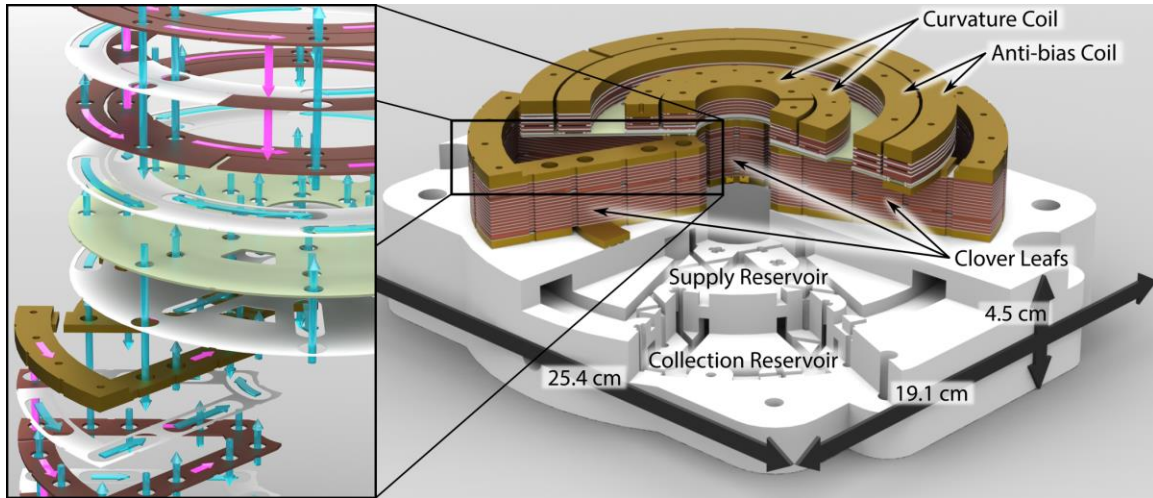


*Figure 6-2 Rendering of Bitter coil assembly. The 3D-printed water distribution manifold is white, a section has been cut away to reveal the geometries of the supply and collection reservoirs. The four leafs of the clover coil sit directly on this distribution manifold (one is hidden to allow the manifold interior to be seen). The inset shows an exploded view of the coil stack with insulating spacers (green and white) that create flow channels between conductive layers (brown). Pink arrows mark the flow of electric current, blue arrows mark the flow of cooling water.*

been cut away to reveal the geometries of the supply and collection reservoirs. The four leafs of the clover coil sit directly on this distribution manifold (one is hidden to allow the manifold interior to be seen). The inset shows an exploded view of the coil stack with insulating spacers (green and white) that create flow channels between conductive layers (brown). Pink arrows mark the flow of electric current, blue arrows mark the flow of cooling water. shows one of two identical Bitter coil assemblies.

The two identical assemblies were constructed and symmetrically mounted with a minimum spacing of 3.81 cm. We measured the magnetic field generated by each of the



three coils using a three-axis Hall probe (Lakeshore Model 360<sup>†</sup>) at a current of 150 A. The curvature coil generates  $B'' = -49.4(4) \mu\text{T}/(\text{cm}^2 \text{ A})$  and  $B_0 = -156.94(1) \mu\text{T}/(\text{A})$ . The clover coil produces  $B' = 33.3(1) \mu\text{T}/(\text{cm A})$ . Finally the anti-bias coil generates  $B_0 = 160.46(4) \mu\text{T}/(\text{A})$  when operated in Helmholtz configuration, and  $B' = -24.2(1) \mu\text{T}/(\text{cm A})$  when operated in anti-Helmholtz configuration. Additional details on the design and construction of the coil assemblies, as well thermal performance details, are available in Siegel *et. al.*<sup>125</sup>

To allow the tuning of the CAVS magnetic trap depth over a range of several mK, we use three sets of RF antennas. The first set is a pair of single-turn loop antennas in a near Helmholtz configuration. The paired loop antennas create RF magnetic fields polarized parallel to the symmetry axis  $\hat{z}$ . The second and third set are both pairs of

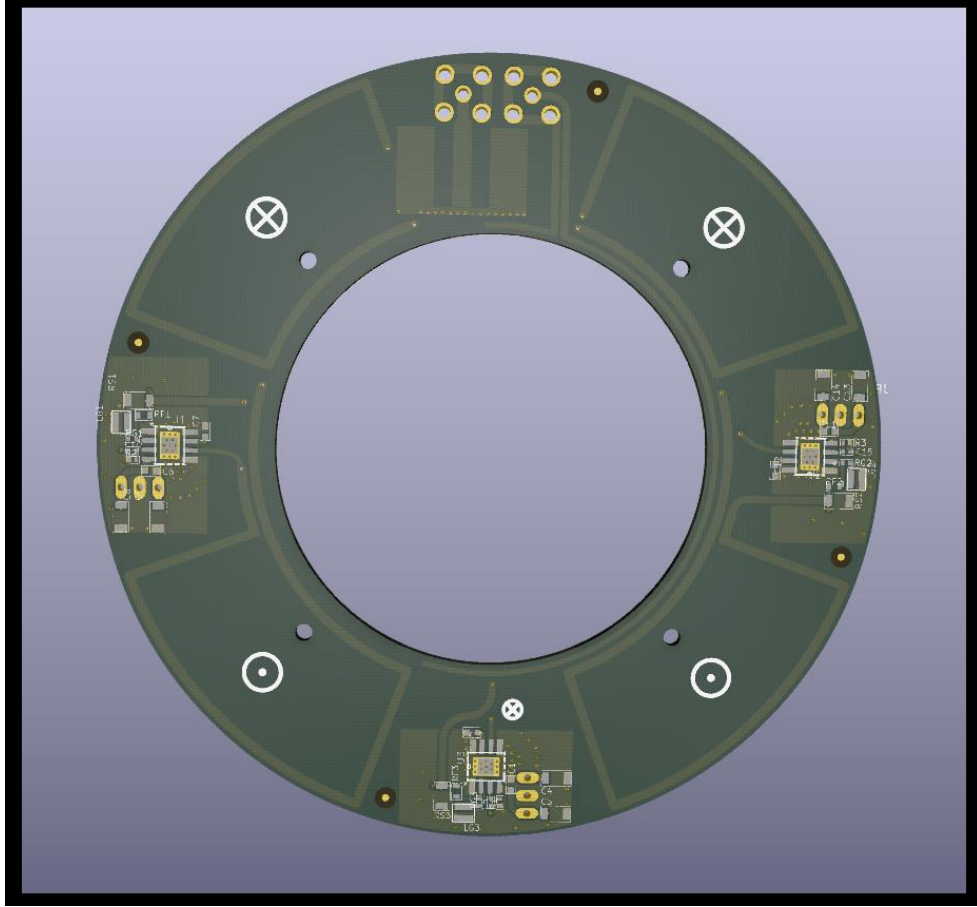


*Figure 6-3 Rendering of one of the two CAVS RF antenna PCBs. The RF current source driving the loop antenna is located bottom middle. The loop antenna itself is patterned on an internal PCB layer and not visible. The RF current sources for the linked-quadrant antennas are on the left and right. White silkscreen markings within each quadrant antenna show the local direction of the RF magnetic field.*

linked-quadrant antennas, which produce RF magnetic fields polarized along  $(\hat{x} + \hat{y})/\sqrt{2}$  and  $(\hat{x} - \hat{y})/\sqrt{2}$  respectively. The RF antennas are patterned onto printed circuit boards. Each antenna set generated RF magnetic fields that drive spin-flip transitions to eject sensor atoms from the CAVS magnetic trap. The CAVS is designed to trap lithium or

rubidium atoms in the  $|F = 1, M = -1\rangle$  state, so a sensor atom comes into resonance with the  $|F = 1, M = -1\rangle \rightarrow |F = 1, M = 0\rangle$  spin-flip transition when

$$\hbar\omega_{RF} = g_F\mu_B B(\vec{r}) \quad 6.2$$

Where  $\omega_{RF}$  is the angular frequency of the RF magnetic field,  $g_F$  is the Lande  $g$ -factor for hyperfine manifold  $F$ , and  $B(\vec{r})$  is the magnitude of the trapping field at position  $\vec{r}$ .

Equation 6.2 defines an RF resonance surface around the magnetic trap center  $\vec{r} = 0$  and, for a quadrupole trap, also defines the trap depth  $U = \hbar\omega_{RF}$ . A wide-bandwidth voltage-controlled RF current source is co-located with each antenna. The RF current source uses a current feedback operational amplifier circuit to compensate for the frequency-dependent impedance of the RF antennas. It was designed by colleagues as detailed in Barker *et. al.*<sup>126</sup> The RF current source can drive peak currents of 250 mA with a 3 dB bandwidth of approximately 80 MHz (45 MHz) for the loop (linked-quadrant) antenna. The bandwidth of the RF current source allows us to set trap depths up to  $U = \hbar\omega_{RF} \approx k \times 3.8 \text{ mK}$  ( $k \times 2.2 \text{ mK}$ ) using the loop (linked-quadrant) antenna. The range of achievable trap depths is sufficient for mapping the trap depth dependence of thermally averaged loss rate coefficients for rubidium-background gas scattering.

### 6.3 Atom Loading

The first step in trapping atoms is to prepare them in a vapor state. This is often done by heating a solid sample of metal in the vacuum to an appreciable vapor pressure. The necessary temperature for such an effusive source depends on the species, Rb has high enough vapor pressure that very little heating is required, whereas for Li the required temperature is much higher. In normal operation of our apparatus, we don't specifically

monitor the temperature of the source, but rather heat it until it's sufficiently effusive. We expect that we're reaching temperatures well in excess of 400°C. In this sense it's easier to get Rb into the vapor phase, and usually fewer byproduct gases are produced. But the downside is that Rb also more readily stays in the vapor phase, and in fact has appreciable vapor pressure at room temperature, which makes it a potential contaminate. That is, since it's less likely to immediately stick to the chamber wall upon colliding, a Rb atom may seep into the vacuum that we're trying to measure. Our preference for Li is partially motivated by this concern. Li room-temperature vapor pressure is  $\lesssim 10^{-17}$  Pa, so contamination is a much smaller concern.<sup>120</sup>

Our aim is to load a MOT which operates on the  $^2S_{1/2}$  ( $F = 2$ ) to  $^2P_{3/2}$  ( $F = 3$ ) transition of  $^7\text{Li}$ . It consists of six independent, circularly polarized laser beams, detuned - 18 MHz from the  $F = 2 \rightarrow F' = 3$  transition of the Li  $D_2$  line. Each beam has Gaussian rms width of 3.6(2) mm and power 40(1) mW. An electro-optic modulator adds 814 MHz RF sidebands ( $\approx 20\%$  of the optical power in each of the  $\pm 1$  order sidebands) to the beams in order to drive the  $F = 1 \rightarrow F' = 2$  repump transition. A quadrupole magnetic field with axial gradient  $\frac{\partial B}{\partial z} = 3$  mT/cm is formed by two arrays of grade N52 permanent magnet bars held in 3D-printed acrylonitrile butadiene styrene mounts around the vacuum chamber.

#### 6.4 Atom Loading via a 3D printed effusive source

The following is adapted from Norrgard *et. al.*<sup>127</sup> We designed an Alkali Metal Dispenser (AMD) made out of 3D printed titanium and demonstrated it as an effusive source for a lithium MOT. The AMD holds  $\approx 100$  mg of Li, is resistively heated, and was used to directly load a MOT. Figure 6-4 shows this 3D-printed AMD which consists of

two parts: a tube (5.1 mm diameter, 13.8 mm long, 0.13 mm wall thickness) and a plug (1.2 mm thick) which fits snugly into the open end of the tube. Both the tube and plug have tabs for mounting and electrical connections. A slit (5.1 mm long and 0.25 mm wide) in the tube directs the output of the effusive source orthogonal to the plane of the tabs. The combined tube and plug have a measured mass of 584 (2) mg and a designed total surface area (not including surface roughness) of 6.8 cm<sup>2</sup>. The AMD is loaded with seven pellets of natural-isotopic-abundance metallic lithium, which we estimate to total 100 mg. The plug fits tightly into the tube to secure the Li, this press-fit is snug enough to withstand heating and any mechanical stresses present. It is loaded and inserted into the vacuum chamber while under an argon-purged atmosphere.



*Figure 6-4: 3D printed titanium tube and plug.*

The AMD is resistively heated by a current of typically 10 A – 15 A. Upon initial warm-up, the resistance of the AMD dropped by nearly a factor of two, presumably as the (relatively conductive) Li melted and came into better electrical contact with the tube. We therefore characterize the AMD in terms of the power  $P$  dissipated across the AMD.

A laser beam counterpropagating to the Li emerging from the source allows the temperature  $T$  of the Li to be determined spectroscopically. We monitored the laser

induced fluorescence collected on a charge-coupled device (CCD) camera from a spatial region along the laser beam. The frequency-dependent fluorescence is fit to a Maxwell-Boltzmann distribution for a 1D beam. The temperature was measured for a number of dissipated powers  $P$ . In thermal equilibrium, the power dissipated is equal to the thermal power transported away from the source by conductive and radiative processes,  $P = a(T - T_r) + b(T^4 - T_r^4)$ , where  $T_r = 20(1)^\circ\text{C}$  is the measured room temperature and  $a$  and  $b$  are fit coefficients. In the experiments discussed below, the power  $P$  was measured and the AMD temperatures were inferred from the best fit to the empirical model.

In order to be a useful atom source, this AMD needs to deliver a stream of sensor atoms without overwhelming the experiment with contaminant gases. So we must demonstrate its operation in forming a MOT, as well as characterize its off-gassing products.

We begin with the latter. All stainless steel components of the vacuum chamber were degassed in the oven discussed in section 4.7, and all components were cleaned except the lithium pellets themselves (we selected pellets with a minimal visible nitride layer). After installation in the apparatus, we degassed the AMD at  $P = 2.0\text{ W}$  ( $T \approx 240^\circ\text{C}$ ) for 3 days but did not otherwise bake the apparatus to remove water. A mass spectrometer was used to monitor the vacuum during this process, which showed a significant decrease in all gases following this procedure, except  $m = 28$  u. Because Li forms a nitride layer in the presence of air, we suspect the  $m = 28$  peak to be  $\text{N}_2$  originating from the Li pellets.

Figure 6-5 shows the increase in background gas composition recorded on the mass spectrometer when operating the AMD under typical conditions ( $P = 3.0\text{ W}$ ,  $T \approx$

330°C, total pressure  $3.3(6) \times 10^{-7}$  Pa). The presence of an  $m = 14$  u peak roughly 1/10 the intensity of the  $m = 28$  u peak is consistent with the cracking fraction of  $N_2$  in most

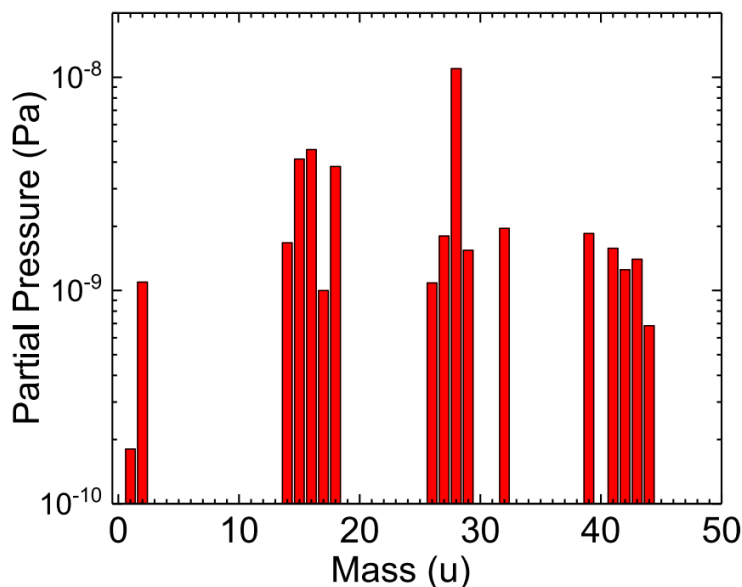


*Figure 6-5 Background-subtracted (i.e., source on minus source off) mass spectrum of gas composition with  $T = 330^\circ\text{C}$ . The total pressure including background is  $3.3(6) \times 10^{-7}$  Pa.*

mass spectrometers. The lack of a visible  $m = 12$  u peak indicates that the possible contribution of CO to the  $m = 28$  u peak is small. The magnitude of the observed  $m = 44$  u peak indicates a negligible contribution to the  $m = 28$  u peak from cracking of  $\text{CO}_2$  into CO (28 u) and O (16 u). In addition, the partial pressure of  $\text{O}_2$  (32 u) is observed to increase. This too may originate from the Li pellets because Li forms hydroxides and carbonates upon exposure to air.

We investigated the outgassing rate of the AMD using the throughput method described in Chapter 4:, obtaining a  $N_2$  outgassing rate of  $q_{\text{AMD}} = 5(2) \times 10^{-7}$  Pa L  $s^{-1}$  for the source operating at 330°C. We do not subtract possible contributions from the chamber itself (which is somewhat heated when the source is operated) and so this value represents an upper bound.

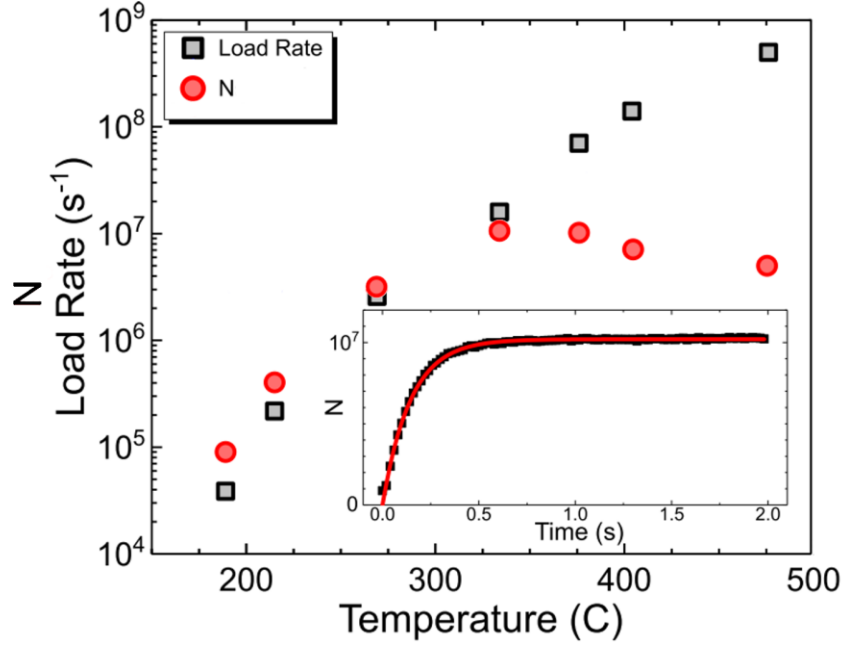


Figure 6-6, reproduced from Norrgard et. al. Loading rate  $R$  (black squares) and steady-state atom number  $N$  (red circles) as a function of temperature  $T$ . The inset shows a typical MOT loading curve with  $T = 330^\circ\text{C}$ . Black squares are measurements and the red line is a prediction, for detail see Norrgard et. al.

Figure 6-6 shows the loading rate  $R$  and steady-state atom number  $N$  as a function of AMD temperature  $T$ . We observe loading rates as high as  $5 \times 10^8 \text{ s}^{-1}$ , comparable to that of many Zeeman slowers.<sup>128</sup> The steady state atom number initially increases as  $T$  is increased, reaching a maximum  $N \approx 10^7$ . For temperatures in excess of  $330^\circ\text{C}$ , we measure an equilibrium  $\text{N}_2$ -equivalent pressure of  $1.8(4) \times 10^{-7} \text{ Pa}$  on an ion gauge installed on the vacuum chamber.

This demonstration shows that our 3D-printed Ti AMD is of sufficient quality to deploy in the experiment. It loads a Li MOT with comparable atom number, load rate, and background pressure to other MOTs directly loaded from effusive sources. With a modest pumping speed of  $100 \text{ L s}^{-1}$  and negligible other outgassing sources, the pressure in the chamber would be  $\approx 10^{-9} \text{ Pa}$ , a useful level for a range of atom experiments.



### 6.5 Atom Loading via Light-Induced Atomic Desorption

Producing atoms in a vapor as described above—by heating an effusive source—has a disadvantage, regardless of the atom species: eventually the source material is depleted, and it can be quite inconvenient to install a new source since it requires breaking vacuum. An attractive alternative to these conventional vapor sources is light-induced atomic desorption (LIAD)<sup>129,130</sup> where atoms are liberated from a surface using photons. Using LIAD as a source of sensor atoms would enable us to recycle them, in principle any atoms deposited on a visible interior surface could be used desorbed again and again. In order to investigate feasibility of this technique for use in the CAVS, we demonstrated light-induced atomic desorption of lithium and subsequent capture in a MOT. The following is adapted from Barker et. al.<sup>131</sup>

We characterize the light-induced atomic desorption process by loading a Li MOT within a stainless-steel vacuum chamber. All steel components were baked in the vacuum oven described in section 4.7 for 21 days at 425 °C to reduce hydrogen outgassing, subsequent water-bakes were not carried out after chamber assembly, but rather the system was continually pumped for several months before we began the LIAD study. The outgassing rate and base pressure are similar to what we would expect from a 48 hour bake at 150°C. The chamber was maintained by at 50 L/s ion pump at  $4(1) \times 10^{-8}$  Pa as read by an uncalibrated ion gauge. We used the 3D printed Ti AMD to deposit lithium on fused silica viewports installed on the chamber. Immediately after deposition, the optical depth of each viewport's lithium coating was on the order of 0.1. We observed no reduction in the coating's optical depth during our LIAD study.

Our six-beam MOT is as described previously in Section 6.1 . We use three different light sources to desorb Li from the fused silica viewports. The first two sources are multimode laser diodes (LDs) at 405 nm and 445 nm. The third light source is a UV LED with a center wavelength of 385 nm. The maximum power of these sources is 350 mW, 1.6 W, and 1.6 W respectively. We collimate the LED output, but the large divergence still limits the power available for LIAD to about 500 mW. The average intensity corresponding to the maximum LIAD power is approximately 45 mW/cm<sup>2</sup>, 70 mW/cm<sup>2</sup>, and 300 mW/cm<sup>2</sup> for the 385 nm, 405 nm, and 445 nm light sources, respectively. Our LIAD light sources are collimated and normally incident to the input and output viewports, and as such LIAD light passes through the vacuum chamber without impinging directly on any stainless-steel surfaces.

We load our MOT using LIAD for 40 s while measuring the MOT fluorescence with a CCD camera. This is long enough for the atom number  $N_S$  to saturate. In the absence of LIAD light, there is no observable MOT. After loading, we extinguish the LIAD light and record the decay of the trapped atom number for 10 s. We activate the LIAD light source and MOT beams 5s before turning on the repump EOM to collect images for background subtraction. Figure 6-7 shows a typical MOT loading curve taken using the UV LED as LIAD source. The corresponding vacuum pressure dynamics (pane b of the figure) measured by the ion gauge are not caused by desorbed Li, we know this because of the physical geometry of the chamber and low vapor pressure of Li at room temperature. Furthermore, an RGA was installed on the chamber near the location of the ion gauge, and it detected no Li.

The cause of the observed pressure variation is light-induced desorption of other species (contaminants) from the viewports, see Barker *et. al.* for a detailed description.<sup>131</sup>

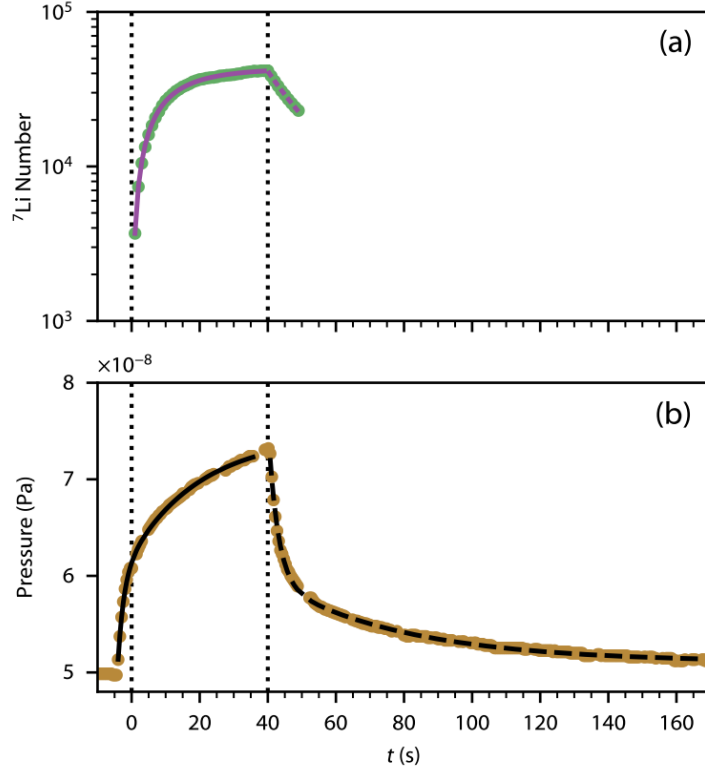


Figure 6-7 MOT loading with 490 mW of light from the 385 nm LED. (a) The atom number as a function of time in green and fits to the data in purple, with solid lines indicating loading and dashed lines indicating decay. The vacuum pressure measured by an ion gauge is shown in (b). The solid (dashed) black line in the bottom subplot indicates a double exponential growth (decay) fit to the pressure data. The vertical dotted lines denote the beginning and end of MOT loading.

Neglecting the two- and three-body loss terms that appear in Eq 5.4, the MOT loading is described by the following differential equation

$$\frac{dN}{dt} = R - [KP_r(t - t_0) + \Gamma_{Li}]N \quad 6.3$$

where  $R$  is the MOT loading rate,  $P_r$  is the pressure increase,  $t_0 = -5$  s is the delay between LIAD source activation and the beginning of MOT loading, and  $K$  is the loss

rate coefficient as usual. We observe that the additional MOT loss due to desorbed lithium, with rate  $\Gamma_{Li}$ , is time independent.

We measured the saturated atom number  $N_S = R/[KP_r(t_{load} - t_0) + \Gamma_{Li}]$  and loading rate  $R$  of the MOT as a function of the LIAD light power and wavelength. Figure 6-8 shows the results of these measurements. The MOT can load as many as approximately  $4 \times 10^4$   $^7\text{Li}$  atoms using the 385 nm LED or 445 nm LD as the LIAD light source. Use of the 385 nm LED yields the fastest loading rates (up to approximately  $4 \times 10^3$   $^7\text{Li}$  atoms per second). We do not observe saturation of either the MOT loading rate nor the saturated atom number, suggesting that our LIAD light sources are not depleting the viewport's lithium coating. This agrees with our observation that each viewport's optical depth is constant.

These loading rates are lower than those achieved by the 3D printed AMD discussed in section 6.4 , but this could still be a viable atom source depending on the particular details of the overall experiment. Dispenser sources can add a significant gas load to a vacuum system, whereas our LIAD source only increases the pressure by about 50%. Additionally, dispenser sources deplete more quickly, which limits the useful lifetime of a compact device.

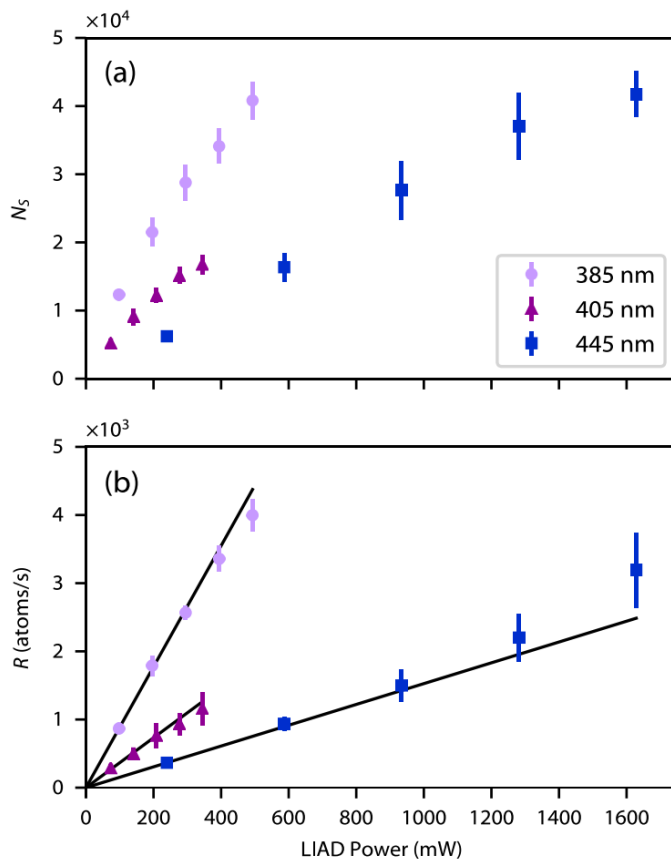
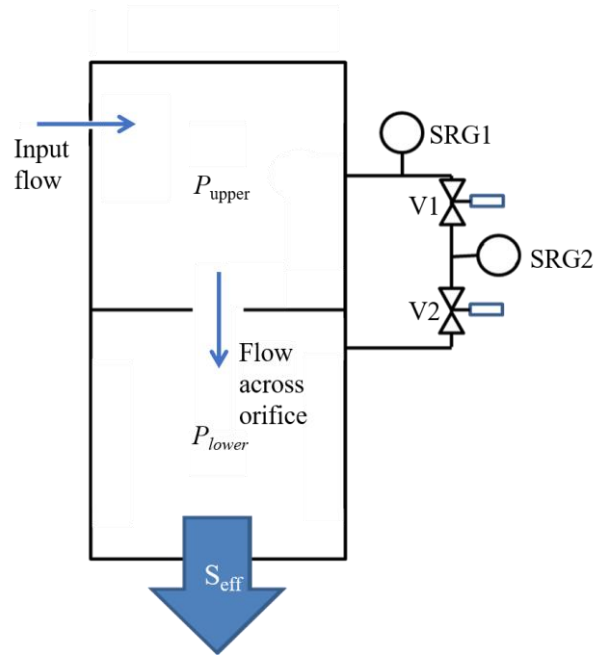


Figure 6-8 - Saturated atom number (a) and loading rate (b) for the  $^7\text{Li}$  MOT as a function of LIAD power. Data are for LIAD sources operating at 385 nm (lavender circles), 405 nm (purple triangles), and 445 nm (blue squares). The solid lines in (b) are linear fits to the measured loading rate. Error bars are one standard deviation.

## 6.6 Dynamic Expansion Chamber to produce known pressure

Prior to the development of the CAVS, the working primary standard at NIST and other NMIs consists of an apparatus to generate a known flow of gas and inject it into a dynamic expansion chamber (as briefly described in Chapter 2). We use this well-understood technique to set known pressures and verify the cross sections calculated *ab initio* by Makrides et. al.,<sup>132,133</sup> as well as to enable the measurement of cross sections

between sensor atoms and other gases of interest for which calculations are impossible. Moreover, this apparatus provides a helpful diagnostic tool. This section will cover the XHV dynamic expansion system, and the next will cover the XHV flowmeter.



*Figure 6-9: Basic schematic of a simple Dynamic Expansion chamber.*

The principle of dynamic expansion is based on gas flow through an orifice with conductance  $C_0$ , which sets up a pressure difference across the orifice according to equation 6.4 (We've already seen this equation, 2.1 in Chapter 2 traditional pressure metrology, it is reproduced here).

$$\Delta P = P_{\text{upper}} - P_{\text{lower}} = \dot{n}RT/C_0 \quad 6.4$$

For the moment, we assume freedom to set any arbitrary flow  $\dot{n}$ . In the idealized picture, if the pressure in the lower chamber  $P_{\text{lower}}$  can be reduced to zero, this gives us the ability to dial in whatever pressure we want in the upper chamber. This is the central aim of the entire apparatus, to set an arbitrary pressure in the upper chamber. For pressures in the high vacuum, this approximation of  $P_{\text{lower}} = 0$  is accurate and gives useful results.

Below about  $1 \times 10^{-4}$  Pa, we need to be more careful about the details. In order to consider it a functionally-primary pressure realization,  $P_{\text{lower}}$  must be negligible, because otherwise we must measure it in order to ascertain the pressure of interest,  $P_{\text{upper}}$ , and a measurement can't rely on another measurement of like kind and remain primary. To achieve the lowest possible pressures, our XHV Dynamic Expansion (XHV-DE) chamber is outfitted with a large turbo pump, and two UHV-rated getter pumps as shown in Figure 6-10. A large turbomolecular pump backed by a dry roots pump combine to provide sufficient effective pumping speed  $S_{s,\text{eff}}$  to evacuate the XHV side, and another large turbomolecular pump, this time backed by a smaller turbomolecular pump in turn backed by a second dry roots pump, provides pumping speed  $S_{\text{eff}}$  to evacuate the UHV side, in combination with two SAES model UHV1400 getter modules (hydrogen pumping speed

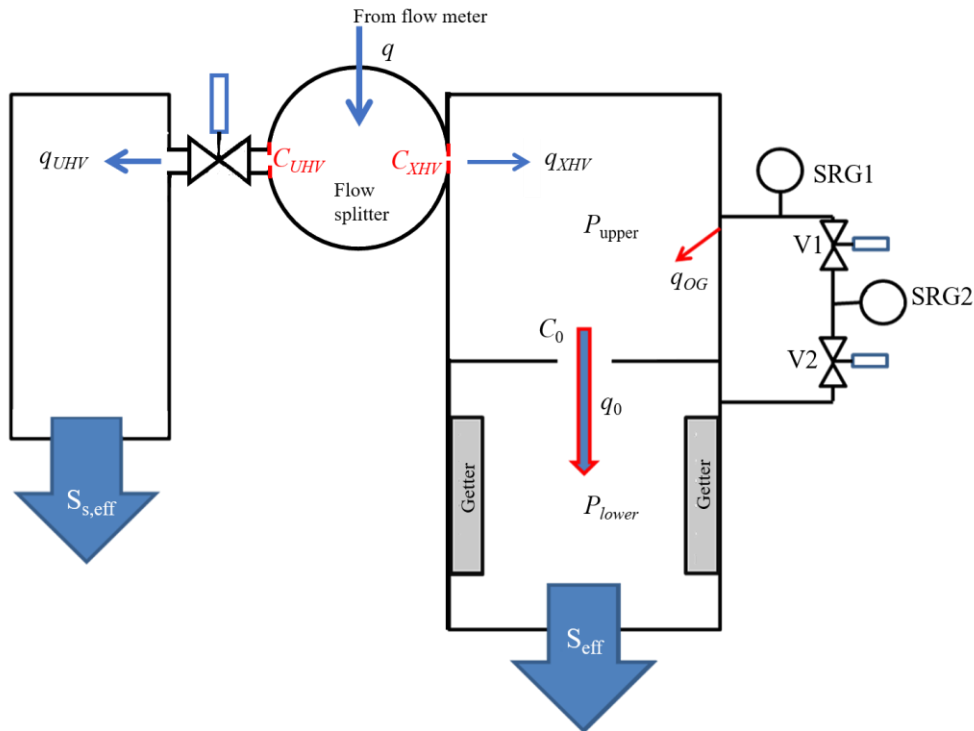
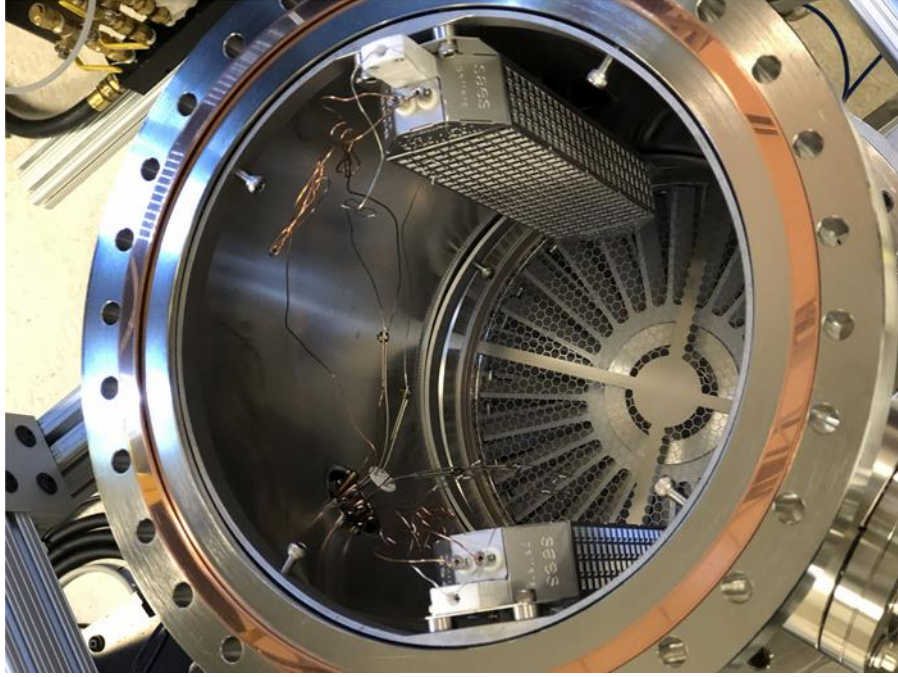


Figure 6-10: Full system schematic of the XHV-DE, similar to Figure 6-9 but showing the flow splitter and getters, as well as indicating outgassing. Flow splitter orifices are shown in red.

of 1360 l/s, hydrogen sorption capacity 9100 Torr-l, effective only for pumping reactive gases)<sup>†</sup>.



*Figure 6-11 View of XHV DE lower chamber, showing UHV getter pumps above the top of the turbomolecular pump.*

But of course, even with the best available pumping, in the real world true zero pressure is impossible to create, so we're in a bit of a bind. Instead, we can rewrite Eq 6.4 in terms of the pressure ratio  $R_p = P_{\text{upper}}/P_{\text{lower}}$ , and if we're clever about measuring the ratio in a way that is independent of any calibration, we retain the primary-ness of the method.

Neglecting outgassing and leaks, we have

$$P_{\text{upper}} = \left( \frac{R_p}{R_p - 1} \right) \frac{\dot{n}RT}{C_0} \quad 6.5$$



To measure the pressure ratio  $R_p$  we've designed the XHV-DE with a bypass constructed out of DN-40 (40mm bore) vacuum hardware. The valves on either side of the bypass are pneumatically actuated all-metal bakeable high-throughput valves (VAT series 57.1<sup>†</sup>, bakeable in open position to  $\leq 450^\circ\text{C}$  without actuator, UHV-rated) and a spinning rotor gauge (SRG2 in Figure 6-9) is mounted between them, such that it can be opened to either the upper or lower chamber. SRGs were introduced in Chapter 4. They are ideally suited to ratiometric comparison measurements because they have very good linearity over a wide range, as well as being bakeable. The uncertainty associated with the pressure ratio is  $u_{R_p}$  which contributes to the pressure of interest,  $P_{\text{upper}}$ , as  $u_{R_p}/R_p$ .

We measure  $R_p$  with the SRG installed on the bypass, it depends on the ratio of the effective pumping speed  $S_{\text{eff}}$  and the orifice conductance  $C_0$ . To see how, we can think of the DE system as being comprised of three chambers instead of two, if we consider the pump itself to be a chamber, as schematically illustrated in Figure 6-12.

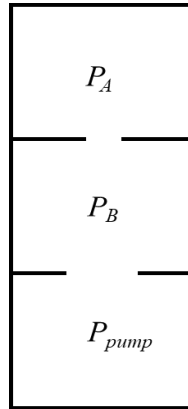


*Figure 6-12 Cartoon schematic depicting the XHV-DE as a three-chamber system.*

Now we apply Eq. 6.4 to the  $P_B/P_{\text{pump}}$  system for which the “conductance” is just the effective pumping speed  $S_{\text{eff}}$ , we get  $P_B = \dot{n}RT/S_{\text{eff}}$ . Now apply Eq 6.4 to the  $P_A/P_B$

system, for which the conductance is  $C_0$ . Combining these we get a useful expression to predict the pressure ratio based on the published pump specifications:

$$R_P = \left( \frac{S_{eff}}{C_0} \right) + 1 \quad 6.6$$

For example, if  $S_{eff} = 1000$  L/s and  $C_0 = 138$  L/s (roughly the  $H_2$  conductance for a 2 cm diameter orifice), then  $R_P \approx 8$ . This prediction is approximate, since the effective pumping speed varies, so in practice  $R_P$  is measured. In the molecular flow regime, where the mean free path of particles is large compared to chamber dimensions, conductance through an orifice depends not only its area  $A$ , but also on the particle mass  $m_0$ ,  $C_0 = A\sqrt{kT/2\pi m_0}$ .

Because both pumping speed and orifice conductance depend on the gas species, the pressure ratio depends on gas species as well, and must be measured. Since our system uses getter pumps in addition to a turbomolecular pump, the pressure ratio may change as the getters become more saturated and should be re-measured regularly, depending on the gas species. To measure  $R_P$ , a relatively large constant flow is injected into the upper chamber (with valve closed to isolate it from the flow splitter shown in the full system schematic). To be sufficiently above the noise floor of the SRG and thus keep  $u_{R_P}$  below 1%, we need to inject enough gas flow to maintain a pressure as high as 1 mPa in the lower chamber, meaning  $P_{upper}$  may exceed 10 mPa. Lower pressures result in higher uncertainties, and pressures above 100 mPa may exceed the limit in which the SRG is linear. A single  $R_P$  measurement consists of using the SRG to sample the upper and lower chambers following the pattern: U L L U (this pattern cancels linear drift). About six measurements are needed in order to get good statistics.

*Table VIII Measured pressure ratios in the XHV dynamic expansion system for selected gas species.*

<i>Gas Species</i>	<i>Mass (u)</i>	<i>Pressure Ratio</i>
He	4	19.1(3)
Ne	20	35.4(3)
N <sub>2</sub>	28	35.7(7)
Ar	40	42.2(8)
Kr	80	45.3(6)

The XHV-DE is designed with a flow splitter to divide the incoming gas from the flowmeter, and inject only 1/100 of it to the upper chamber, the balance is pumped away by  $S_{s,eff}$ , see Figure 6-10. This is accomplished by means of a spherical chamber (to simplify gas dynamics and ensure uniformity) and precision-machined orifices with conductances  $C_{XHV}$  and  $C_{UHV}$ . Flow  $q$  is defined as  $q = \dot{n}RT$  and has units of Watts (recall pressure has units of energy density).

The split ratio  $\alpha$  is defined  $\alpha \equiv q_{XHV}/q$ , where  $q$  is the input flow from the flowmeter and  $q_{XHV}$  is the flow into the upper chamber. We can measure  $\alpha$  using SRG1 to measure the pressure in the upper chamber (V1 open and V2 closed) and switching the gate valve between the flow splitter and the UHV chamber between open and closed states. It follows from Eq 6.5 that  $P_{upper} = \left(\frac{R_P}{R_P-1}\right)\frac{\alpha q}{C_0}$ . With the gate valve GV closed, this becomes  $P_{upper,closed} = \left(\frac{R_P}{R_P-1}\right)\frac{q}{C_0}$ . Dividing these equations we arrive at a simple expression for the split ratio,

$$\alpha = \frac{P_{upper,open}}{P_{upper,closed}} \quad 6.7$$

We designed the flowmeter with  $C_{\text{XHV}} = 1$  mm and  $C_{\text{UHV}} = 10$  mm, so we expect the split ratio to be about  $\alpha = 1/100$ . At time of writing, atom-side systematics prevent us from needing to push into the XHV, and so we have not yet measured  $\alpha$ .

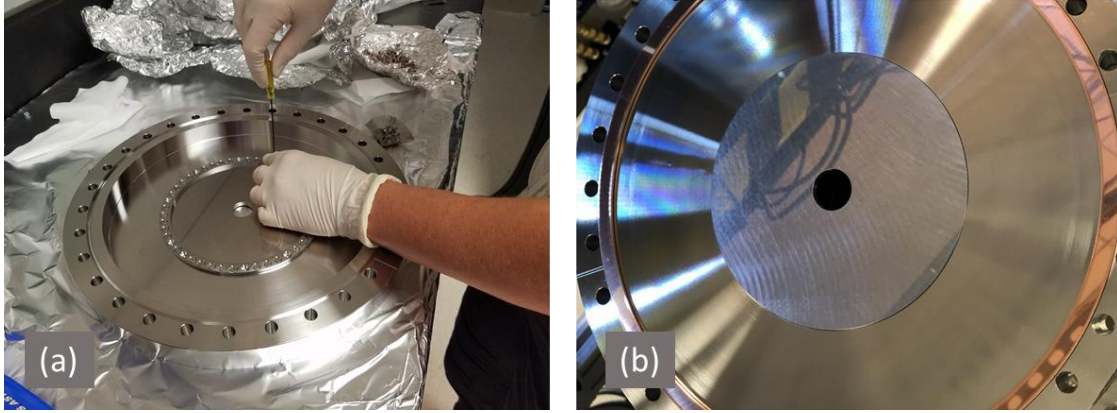


Figure 6-14: (a) bottom-view of nominal 2 cm orifice being installed onto orifice plate. The researcher is tightening the indium seal to close all alternate gas pathways. (b) top-view of orifice immediately following installation.

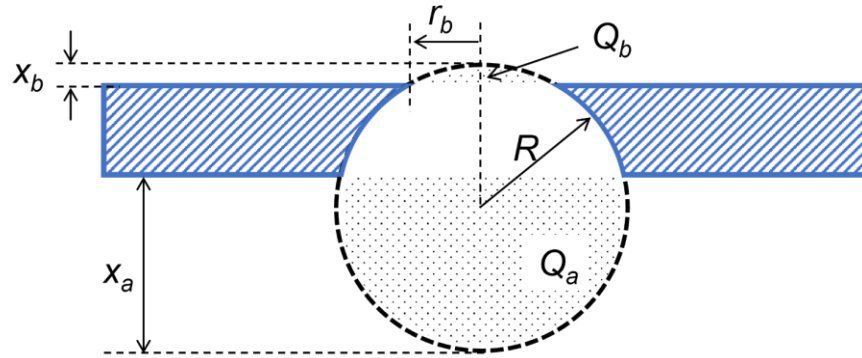


Figure 6-13: Cross section of slab (blue) with partial-spherical orifice, which can be thought of as a spherical bubble with radius  $R$  that extends a distance  $x_a$  ( $x_b$ ) below (above) the lower (upper) face of the slab. The circular hole in the upper face of the slab has radius  $r_b$ .  $Q_a$  and  $Q_b$  are the pieces of the spherical bubble that extend beyond the slab, useful for characterizing the transmission probability of the orifice.

Another source of uncertainty in the XHV dynamic expansion chamber is related to the orifice.<sup>134</sup> In the molecular flow regime, the dynamics of gas particle collisions are calculable with objects of certain analytical geometries. An ideal orifice would have a

partial-spherical cross section, but a real orifice by necessity must have at least a short cylindrical section.

Following Poulter<sup>135</sup>, the total conductance is given by

$$C = K_T K_S \frac{1}{4} A \bar{v} = K_T K_S \frac{1}{4} \bar{v} \pi r_b^2 \quad 6.8$$

Here,  $K_T$  is the transmission probability through the small tube and  $K_S$  is the transmission probability of the spherical orifice,  $A = \pi r_b^2$  is the entrance area, and the average speed of the gas is  $\bar{v} = \sqrt{8RT/\pi M}$ , see Figure 6-15. The transmission probabilities  $K_T$  and  $K_S$  of the cylindrical tube and spherical sections can be calculated analytically. For a very short tube ( $D \ll L_T$ , certainly true here) an approximate formula<sup>84</sup> is often used,

$$K_T = 1 - \frac{L_T}{D} \quad 6.9$$

This formula assumes that an incoming particle which hits the tube will leave the tube in the forward or backward direction, and not hit the tube again. The spherical orifice was calculated analytically by Edwards and Gilles<sup>136</sup>, their expressions are reproduced below. They first derive a unitless factor to characterize the amount of the sphere that's cut off from either end, depicted in Figure 6-13,

$$Q_a = \frac{(x_a/R)-1}{|(x_a/R)-1|} \left[ 1 - \left( \frac{r_a}{R} \right)^2 \right]^{\frac{1}{2}} \quad 6.10$$

And an analogous expression for  $Q_b$ . The transmission probability  $K_S$  depends on  $Q_a$  and  $Q_b$ ,

$$K_S = \left[ \frac{1 + Q_b}{2 + Q_b + Q_a} \right] \left[ \frac{2}{1 - Q_a} \right] \quad 6.11$$

Notice that the first factor on the right-hand side of Eq. 6.10 is just for the sign, so  $K_s$  really just depends on the radii  $r_a$ ,  $r_b$ , and  $R$ . Conductance of a realistic partial-spherical orifice can now be calculated using Equation 6.8. Our Dynamic Expansion apparatus employs a number of orifices, but in most instances, it is sufficient to measure the conductance, so we just use a straight hole. The main orifice,  $C_0$  in Figure 6-10, had originally been manufactured to have a partial-spherical cross section with short cylindrical land, but difficulty in polishing the bore without damaging the plate limited its

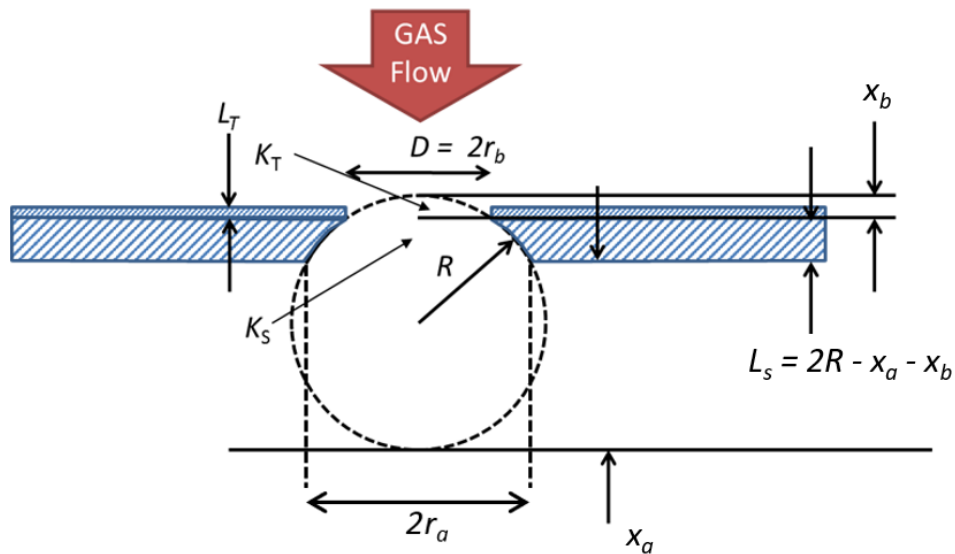


Figure 6-15. Another diagram of an orifice with near partial-spherical cross section, this time showing the small cylindrical “land” or tube which must be present in order to be machinable (a truly spherical cross section would have an infinitely sharp edge). The diameter of the tube is  $2r_b$  and its length is  $L_T$ . The transmission probability of the tube section is  $K_T$ , and that of the spherical section is  $K_S$ .

practicality. Ultimately, we made the decision to use a cylindrical bore instead, since we have access to expertise in dimensional measurement.

*Table IX - Calculated transmission probabilities and total conductance for a near-spherical orifice with 2 cm diameter in a ~2 mm thick plate. See Figure 6-15 for geometry.*

<i>Spherical Orifice Transmission</i>						
<i>D(mm)</i>	<i>L<sub>S</sub>(mm)</i>	<i>R(mm)</i>	<i>x<sub>b</sub>(mm)</i>	<i>x<sub>a</sub>(mm)</i>	<i>r<sub>a</sub>(mm)</i>	<b><i>K<sub>S</sub></i></b>
20.00	1.78	19.05	33.49	2.84	12.43	<b>0.99606</b>
<i>Short Tube Transmission</i>						
<i>D(mm)</i>	<i>L<sub>t</sub>(mm)</i>					<b><i>K<sub>T</sub></i></b>
20.00	0.0508					<b>0.99746</b>
<i>Total Conductance for Hydrogen</i>						
<b><i>C<sub>0</sub></i></b>						
<b>138.168 l/s</b>						

The dimensions of the cylindrical bore orifice have been precisely determined by the Dimensional Metrology group at NIST. The nominally-cylindrical bore tapers from 21.961 mm to 21.954 mm between plate surfaces, and is free of chatter to within measurement resolution (microns).

Another technique exists to reduce the pressure of interest  $P_{\text{upper}}$ , and although we have not configured our experiment this way as of writing, it bears mentioning as a future possibility. Naively one might simply build a larger orifice  $C_0$  into the chamber in order to reduce  $P_{\text{upper}}$ , since  $C_0 \approx \frac{1}{4} \bar{v} A_0$  and  $P_{\text{upper}}$  scales as  $1/C_0$ . But this also reduces  $R_p$  and increases the uncertainty in  $R_p$ , so there's a limit to how large a practical orifice can be. Instead, we can achieve lower pressures through the so-called split flow method, in which we inject the gas into the lower chamber such that it backstreams through the orifice into the upper chamber. We define the flow ratio  $R_f$  to be the ratio of such a lower chamber flow to an upper chamber flow that induces the same pressure in the upper chamber. It is determined by Eq. 6.6,  $R_f = \frac{S_{\text{eff}}}{C_0} + 1$ . This quantity would need to be measured for each

gas species since it depends on  $S_{\text{eff}}$  and  $C_0$  which are themselves dependent on gas species. If necessary, this method would enable us to reduce the upper chamber pressure by a factor of ten or a hundred.

### 6.7 Flowmeter for Gas Injection

In order to make use of the dynamic expansion technique just described in section 6.6 we need to inject a known flow of gas into the upper chamber. Doing so is not trivial, and so we dedicate this entire section to it. The apparatus for producing this known gas flow is called a “flowmeter,” an unfortunately confusing term that has little to do with the devices one can buy off the shelf for measuring fluid flow. The first flowmeters for use with expansion techniques were developed by researchers at PTB in Germany, NIST’s sister institute<sup>25</sup>. The operational principle is as follows: a reservoir of gas has an intentional “leak” out of which gas flows, and depending on the apparatus particulars, the rate is measured through a feedback system. Both the flowmeter at NIST in use for traditional metrology, as well as the XHV flowmeter that was built for this project are controlled by maintaining constant pressure, and thus are called, creatively, *constant pressure flowmeters*. In a constant pressure flowmeter, a reference volume and a variable volume are connected to either side of a differential gauge, the variable volume being the one from which output gas flows. The mechanism that operates the variable volume (usually by compressing a bellows) is controlled by feedback to this differential gauge. As gas exits the variable volume, the mechanism reduces it in order to keep the differential gauge reading zero. This serves both to generate and measure the flow.

The newly built flowmeter is referred to as the XHVFM (XHV-Flowmeter), and it was designed to be capable of producing flows between  $1 \times 10^{-13}$  and  $1 \times 10^{-8}$  mol/s.



Using the dynamic expansion system described in section 6.6 and pictured schematically in Figure 6-10, this flow range corresponds to generated pressures between  $1 \times 10^{-11}$  Pa and  $1 \times 10^{-5}$  Pa. The system comprised by the XHVFM and the dynamic expansion apparatus is capable of measuring the thermalized cross sections between various gases and the trapped atoms in the CAVS, the subject of Chapter 8:.

Assuming an ideal gas at temperature  $T$  and fill pressure  $p$ , the equation for flow out of the “leak” is given by,

$$\dot{n} = -\frac{p}{RT} \frac{dV}{dt} + \dot{n}_{OG} \quad 6.12$$

where  $R$  is the molar gas constant,  $V$  is the variable volume,  $t$  is the time, and  $\dot{n}_{OG}$  is the outgassing from the walls of the variable volume. The XHVFM variable volume is made by a welded stainless steel bellows, attached to a DN16 flange in a way that minimizes dead volume, and surrounded by an oil reservoir. A piston is plunged into the oil which in turn compresses the volume at a rate controlled by feedback to the differential gauge. The temperature is monitored, and can be treated as constant over the timescale of operation

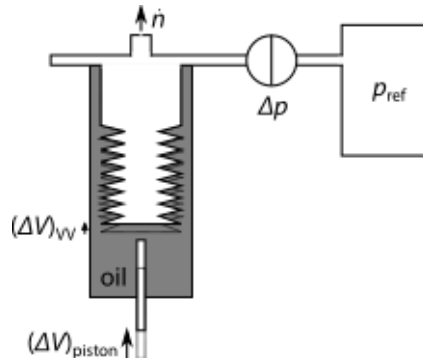


*Figure 6-16 Schematic of the core of the Flowmeter, the volume of the variable volume is adjusted by compressing the bellows. This is controlled via feedback to the differential gauge  $\Delta p$ , keeping the pressures in the reference and variable volumes equal.*

or in the event that it changes appreciably, corrected for. Indeed in the general case,

pressure is not necessarily constant either (say, in a constant-volume flowmeter), and so our measurement equation can be written

$$\dot{n} = -\frac{p\dot{V}}{RT} - \frac{\dot{p}V}{RT} + \frac{pV}{RT^2}\dot{T} + \dot{n}_{OG} \quad 6.13$$

The assumption that the gas be ideal is not necessary either, we can still operate at pressures for which the particles are no longer non-interacting. See Eckel et. al.<sup>137</sup> for a treatment of this case.

Previous flowmeter designs required the operator to fill the reference volume by manually adjusting a leak valve, the behavior of which is non-linear and very difficult to predict and therefore difficult to automate. To make the XHVFM fully automated, we designed a fill system that uses an array of three crimped capillaries to fill the reference volume, rather than a leak valve. This fill system fills the reference volume and the variable volume to the same pressure within 2% of a setpoint in the range of 13 Pa to 150 kPa. Given rough knowledge of the outlet conductance  $C$ , filling to a particular setpoint ensures that the generated flow will be close to the desired value, but it is not correct to say that the flowmeter generates a known flow. The flow is *measured* via constant-pressure feedback to the reference volume.

Gas flow  $\dot{n}$  exits the variable volume of the XHVFM through one of two constrictions: a leak valve, or a sintered stainless steel Standard Conductance Element or *SCE*, each has advantages and disadvantages and can be selected by the user. The leak valve can be adjusted to dial in a wide range of conductances from 0.4 L/s to  $1 \times 10^{-13}$  L/s for N<sub>2</sub> around room temperature, allowing the user to tune the system for gas species and flow rate, but mechanical slop in the actuator mechanism makes it non-linear and difficult

to set repeatably, and it can be prone to drift, especially for low conductances. The SCE is not adjustable at all, sacrificing flexibility for repeatability, with a conductance of about  $5 \times 10^{-10}$  L/s for N<sub>2</sub> around room temperature. In practice, for pressures in the UHV and XHV, we can use the SCE almost exclusively.

Flowmeters are primary realizations for flow, that trace to the SI through the pascal and the second. This traceability is crucial for the overall goal of the CAVS experiment, in order to gain acceptance in the metrology community, we have to demonstrate the accuracy of the CAVS via comparison to traditional pressure realizations. Traceability to the second is trivial at the accuracies required, we can use the control computer's clock for our timing. For pressure traceability we have to be somewhat more careful, but we're fortunate to have the machinery of NIST pressure calibration services at our disposal. As of writing, NIST still realizes pressure by manometry (the FLOC will be adopted within the next few years, and manometry retired), which is employed to calibrate capacitance diaphragm gauges (CDGs) giving us pressure sensing capabilities with the lowest possible uncertainties, generally on the order of a few  $p \times 10^{-3}$ . CDGs are the gauge of choice for a number of reasons. All-metal CDGs can withstand heat treatment and mechanical shock, they're true sensors of pressure (as opposed to sensors of a proxy such as gas conductivity) and so are independent of gas species, and they have excellent sensitivity and repeatability compared to Pirani or thermocouple gauges. We use a suite of three bakeable CDGs in an enclosure to ensure traceability of the XHVFM to the pascal, and because they will be routinely heat-treated, we undertook an investigation of their stability under repeated bakes as described in the following subsection.

## 6.8 Stability of Bakeable CDGs

We obtained three series 616A Baratron gauges from MKS instruments for use in the XHVFM. These gauges are specified to be bakeable up to at least 400°C and operable up to at least 300°C. Each of these gauges is of differential type, but if the reference side is evacuated, they can be used as absolute gauges as well. The gauges have nominal upper scale limits of 133 Pa, 1333 Pa, and 133322 Pa; we refer to them as 1-torr, 10-torr, and 1000-torr for simplicity. Before installing them into the XHVFM, these were subjected to a bake at 425°C for 33 days in the oven described in section 4.7 to reduce hydrogen outgassing. They were then installed in an aluminum box insulated on the inside with 25 mm thick Marinite board. A custom-built thermoelectric cooler controls the temperature inside the box to  $\approx 25^\circ\text{C}$ . The gas handling manifold was designed to minimize volume,

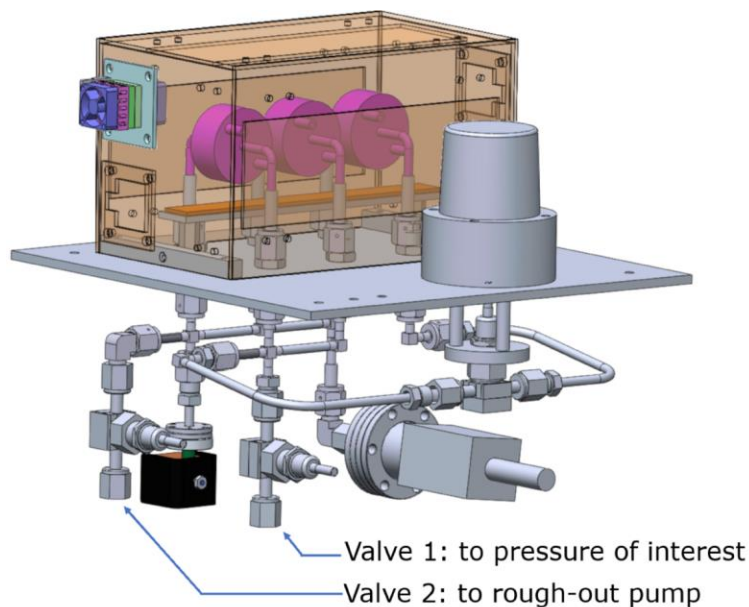


*Figure 6-17: Bakeable CDGs (pink) inside a temperature controlled box with plumbing manifold.*

and is equipped with a pneumatic shut-off valve to isolate the 1-torr gauge from high pressure fills. An ion pump maintains base pressure of  $\approx 10^{-6}$  Pa on the reference side.

Following this bakeout and assembly, we performed an initial comparison of the three bakeable CDGs to a set of transfer standard CDGs calibrated by manometry. The initial comparison indicated a large (on the order of tens of percent) difference in linear sensitivity between the two sets of 10-torr and 1000-torr gauges. In fact, the difference in sensitivity was much larger than the manufacturer's specifications, suggesting that the high temperature 425°C bake annealed the iconel membrane. The 1-torr gauges did not show a large discrepancy. The offset and span controls were adjusted to bring the gauges into alignment.

We then performed a subsequent comparison of the bakeable CDGs to our transfer standard following the procedure outlined below. First, we evacuated both the transfer standard and the bakeable CDGs to  $< 0.4$  Pa and recorded pressures. We tested the gauges at pressures covering the entire range of each gauge, selecting nine nominally equally spaced pressures to cover each of three pressure decades (eg., 0.1, 0.2, 0.3, ... 0.9, 1, 2, etc.) for pressures up to 12 kPa. Pressure readings were recorded for both the transfer standard and for the bakeable CDGs for all combinations of gauges and ranges which had as their maximum full-scale range the maximum point of the decade.

For example, the 10-torr gauge at gain X0.1 has a full-scale pressure range of 133 Pa, so its readings were recorded on the decade spanning 13 Pa to 120 Pa. A full sweep through the pressure ranges is labeled a "run". In most cases a run requires about 6 hours to complete. Generally we acquired ten runs before stopping to perform a bake. At this

point, the TEC is removed and replaced by insulation, and internal heaters ramp the temperature to 110°C at a rate of 1°C/min. This temperature is maintained for three to five days, and then the system is allowed to cool back to room temperature. The TEC is reinserted to stabilize the temperature at 25°C. Extra stress was induced at bake 5, which will be explained in due turn.

To begin our analysis, for a given gauge each run is initially fit to a polynomial of the form

$$P = c_0 + c_1R + c_2R^2 + c_3R^3 \quad 6.14$$

where  $R$  is the pressure reading of the bakeable CDG and  $P$  is the pressure reported by the standard. A weighted method was used to determine the coefficients in which the data are inversely weighted by the estimated uncertainty in the transfer standard for the given pressure. Figures 6-18 and Figure 6-19 show the resulting best fit coefficients  $c_0$  and  $c_1$  vs run number, respectively. For now, we ignore higher order coefficients. Bakes are represented by vertical dashed lines. Baking causes large discontinuities in the zero offset, the  $c_0$  term, between several runs for the 10-torr and 1000 torr gauges. For the 1-torr gauge, this discontinuity is only apparent after the first bake; all subsequent bakes maintain a relatively stable zero offset. The discontinuities are less apparent in the linear sensitivity coefficient  $c_1$ . After the first bake, the  $c_1$  coefficient appears to stabilize for all three of the gauges.

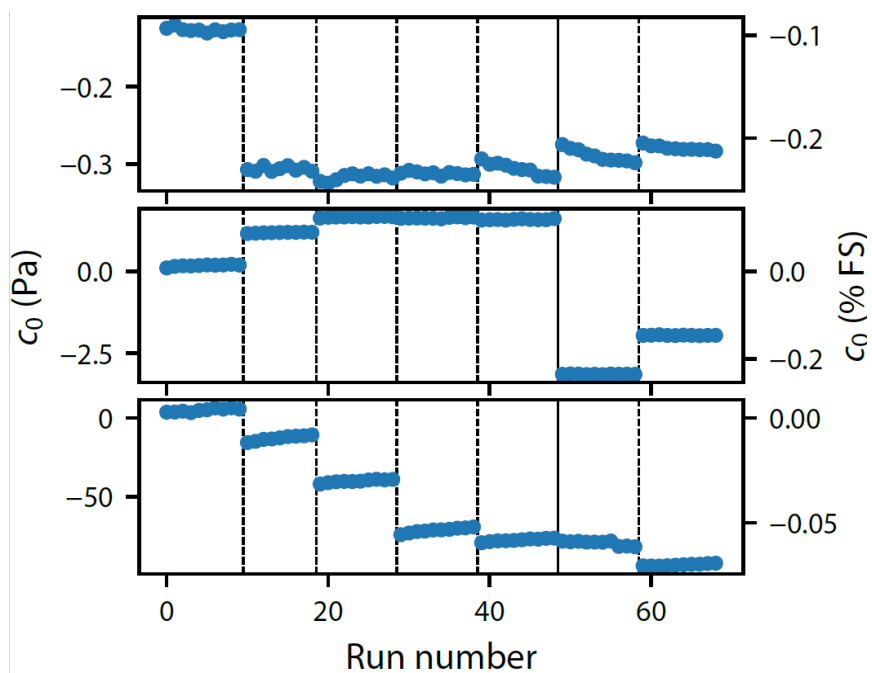


Figure 6-18: The offset  $c_0$  fit coefficients versus run number for the 1-torr gauge with gain X1 (top); 10-torr gauge with gain X1 (middle); and 1000 torr gauge with gain X0.1 (bottom).

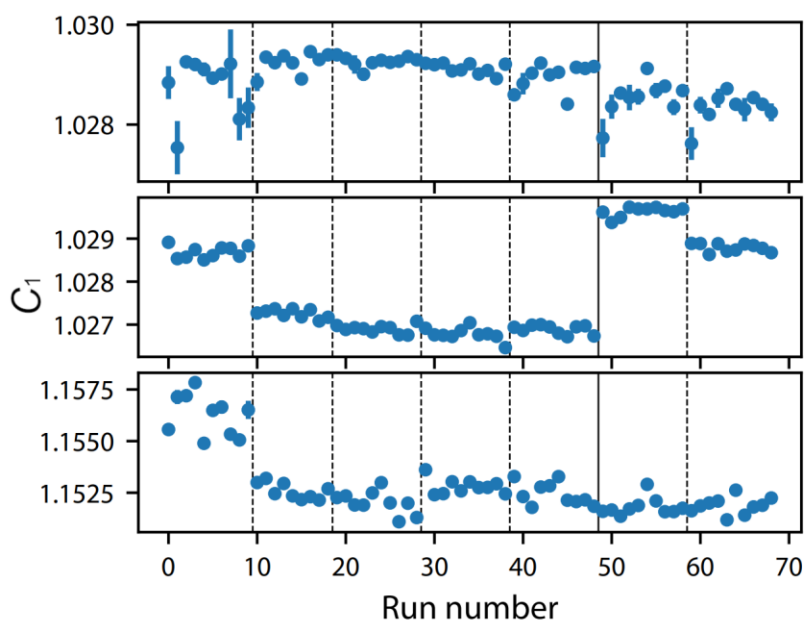


Figure 6-19 Linear sensitivity  $c_1$  coefficients versus run number for the 1-torr gauge with gain X1 (top); the 10-torr gauge with gain X1 (middle); and the 1000-torr gauge with gain X0.1 (bottom).

Preceding the fifth bake (between runs 47 and 48) a test was performed in which three additional stresses were induced to simulate a mishandling incident. First, a mass of approximately 3 kg was intentionally dropped from a height of about 0.5 meters onto the platform on which the entire assembly rested, inducing a shock. Second, a bellows directly under valve 1 in Figure 6-17 was disconnected and reconnected, possibly inducing a torque or other forces on the system. Third, the plumbing leading to the CDGs was wrapped with heater tape, insulated, and baked at 150°C while baking the CDGs to the standard 110°C. These additional tests do not appear to have affected the 1000-torr gauge or the 1-torr gauge, but dramatically impacted the 10-torr gauge. Moreover, the 1-torr gauge appears to be experiencing a downward drift over time. While the zero offset is easily corrected (it can be adjusted when the system is evacuated to base pressure), the linear sensitivity coefficient  $c_1$  is not, and so it must be well understood in order to use the gauge reliably. Drifts in  $c_1$  over time result in uncertainty in the pressure reading (in fact, these drifts are the predominant source of uncertainty in the transfer standard). Excluding runs before the first bake, the  $c_1$  coefficients vary by about 0.08%, 0.2%, and 0.1% for the 1-torr (X1 gain), 10-torr (X1 gain) and 1000-torr (X0.1 gain) gauges, respectively. These variations are consistent with the long-term stability seen over 20 years of calibration of our transfer standard, which uses traditional non-bakeable CDGs. Because the best fits are polynomials, variations in  $c_1$  are strongly correlated with higher



order terms, so variations in  $c_1$  do not by themselves fully characterize the fluctuations of the gauge.

To better quantify the variations between each calibration run, we repeat the fit procedure for each run after the first bake, e.g. with  $r \geq 10$ . We use the entire ensemble of  $r \geq 10$  data to find  $c_1$  and higher order coefficients for a given gauge, but each individual run is fit to find a unique  $c_0$ . We write this global fit function

$$P_r = c_{0,r} + c_1 R_r + c_2 R_r^2 + c_3 R_r^3 \quad 6.15$$

where  $R_r$  are the corresponding pressure readings and  $c_{0,r}$  is the zero offset of run  $r$ . All pressure readings  $R_r$  and true pressures  $P_r$  are fit together to obtain  $c_p$  and  $c_{0,r}$ . An example of this global fit function is shown in Figure 6-20, along with the residuals. The black dashed curves represent that statistical width of the residuals at the  $k = 2$  or  $2\text{-}\sigma$  level. The standard deviation of the residuals around the global fit may be used as an estimate of the long term stability of the gauge, assuming for simplicity that all of the drift is in the gauges under study and not the transfer standard (thus resulting in an overestimate of the drift in the bakeable gauges). And so, we can estimate the long term

stability  $u_{\text{ts}}$  in the operation of the CDGs independently of the uncertainty in their

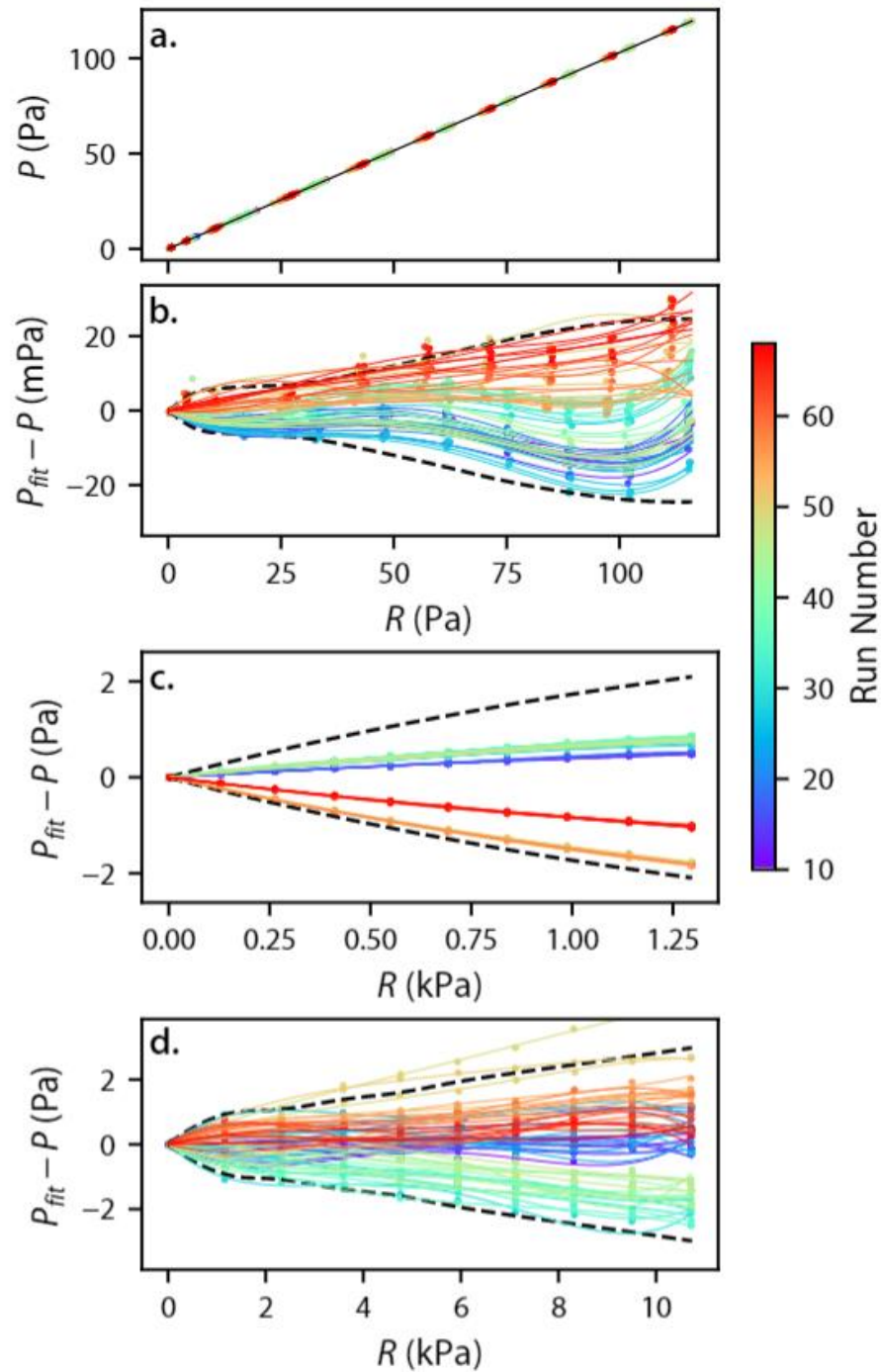


Figure 6-20 (a) example of global fit function for the 1-torr gauge, dots show experimental data, and the black line is the fit. Panes (b), (c), and (d) show residuals of the fit vs. pressure reading  $R$  for the 1-torr, 10-torr, and 1000-torr gauges, respectively. Colored curves indicate the difference of the single-run fit and the global one, and dashed black curves show the estimated 2- $\sigma$  width of the residuals.

calibration.

In addition to the long term stability, there are several other sources of uncertainty in the operation of the CDGs. The full uncertainty in the pressure measured by these gauges is given by

$$u_p^2 = u_{cal}^2 + u_{lts}^2 + u_{rdm}^2 + u_{zero}^2 \quad 6.16$$

Where  $u_{cal}$  is the uncertainty in the gauges' calibrations as described in Ricker et. al.<sup>24</sup>,  $u_{lts}$  is the uncertainty in the long term stability just discussed,  $u_{rdm}$  is the uncertainty due to random fluctuations during a measurement, and  $u_{zero}$  is the uncertainty in the zero measurement. Each of these components is shown in Figure 6-21. The remaining terms  $u_{rdm}$  and  $u_{zero}$  tend to be small by comparison. These both need to be determined at time-of-use. For the calibration data, we recorded a point about every 5 s for 60 s, resulting in 12 individual measurements for a given gauge at a given pressure. With this scheme of data collection,  $u_{rdm}$  is about 10 times smaller than  $u_{lts}$ . The uncertainty in the zero will be a similar value, provided that the gauge is properly and routinely zeroed. If the gauges are calibrated this way, using the global fit function, we expect that even with occasional baking the total uncertainty will be less than 0.3% for all the gauges and ranges tested.

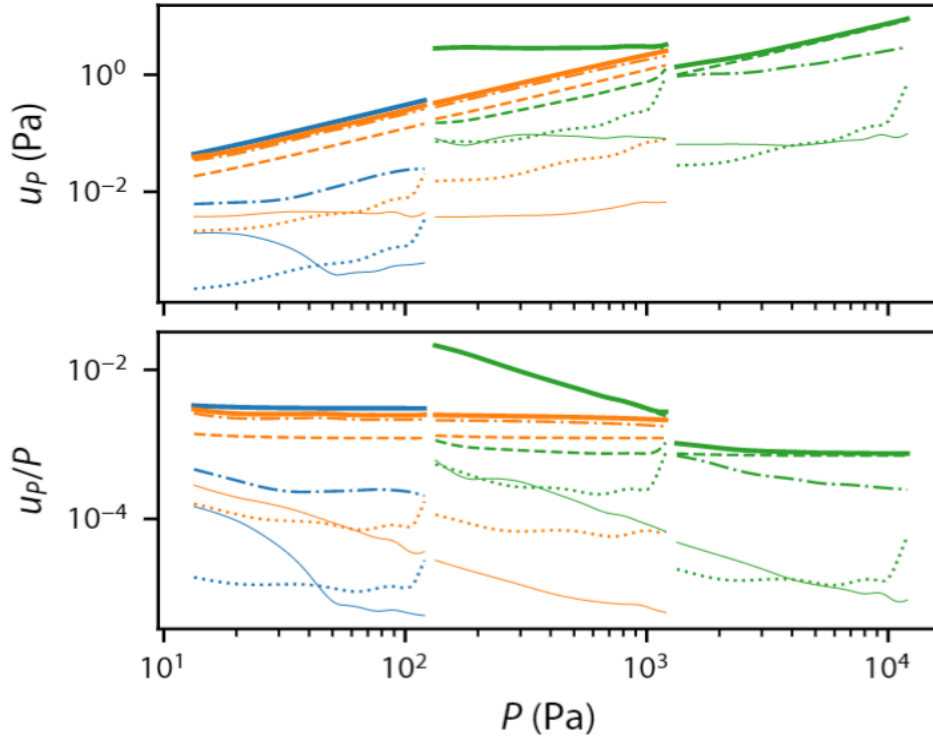


Figure 6-21 Absolute (top) and relative (bottom) uncertainties for the 1-torr (blue), 10-torr (orange), and 1000-torr (green) gauges vs. pressure  $P$ . The thick solid lines indicate the total uncertainty  $u_P$ , the dashed curves indicate the uncertainty in the transfer standard  $u_{\text{trans}}$ , the dashed-dot curves show the uncertainty in the long-term stability  $u_{\text{ls}}$ , the dotted curves show the uncertainty in the fit  $u_{\text{fit}}$ , and the thin solid curves show the average uncertainty due to random fluctuations  $u_{\text{rdm}}$  during a single calibration run. All uncertainties are at the  $k = 2$  level.

Having characterized these bakeable CDGs in this way enables us to know with sufficient certainty the fill pressures in the XHVFM and by extension, give us the requisite confidence our measurement of the flow produced, and ultimately the pressure set in the DE chamber. This pressure is then directly compared with the CAVS, so it sets a lower limit on our uncertainty for the entire project.

## Chapter 7: Beyond the laboratory-scale CAVS

The CAVS will be the first primary pressure standard operating at UHV pressures and below at any national metrology institute. While it promises vast improvements over existing measurement technology, there remains one disappointing fact: it is confined to the lab and can only be operated by NIST personnel. By its Quantum-SI nature, it is inherently accurate and never requires calibration, but it is not deployable. To truly revolutionize pressure metrology at UHV and below, we are developing a miniaturized version of the CAVS (the pCAVS).

### *7.1 Advantages and challenges of a portable CAVS*

Like the lab-scale CAVS, the pCAVS uses trapped Li atoms, which have several advantages over the more commonly used Rb. Rb is more easily trapped, and thus the associated technology is more mature and affordable. However, the high vapor pressure

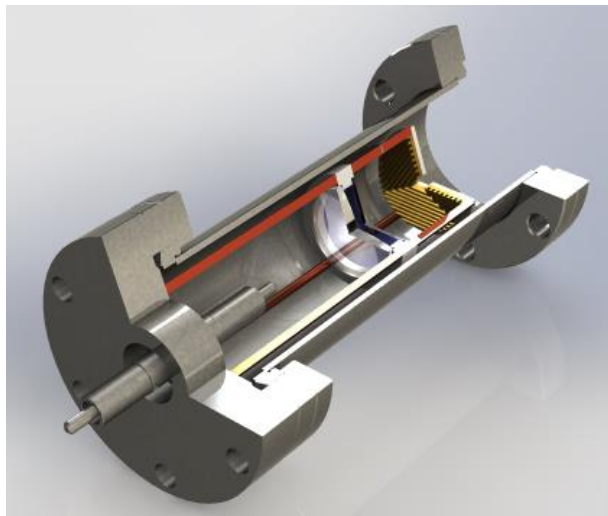


*Figure 7-1: A 3D model of a possible commercial pCAVS device, including a model of the triangular grating chip. Reprinted from S. Eckel, D. Barker, J. Fedchak, N. Klimov, E. Norrgard and J. Scherschligt, Metrologia (2018).*

of Rb limits its use as a vacuum measurement tool for two reasons: a Rb-based device cannot be baked (and baking is essential for achieving UHV pressures, as discussed in chapter 4) and Rb will eventually pollute the vacuum environment. Li has an exceptionally low vapor pressure ( $3.2 \times 10^{-18}$  Pa at 20 °C)<sup>138</sup> which prevents vacuum pollution and permits Li-based devices to be baked at 150 °C.

We are investigating methods to reduce vacuum contamination by the pCAVS's Li source. In air, Li oxidizes and reacts with other gas constituents to form hydroxides, nitrides, and carbonates; presumably, these compounds then contribute to outgassing and contamination when the lithium is heated. In chapter 5 we discussed a miniature Li oven made of 3D-printed titanium.<sup>127</sup> This oven achieves an outgassing rate of  $5(2) \times 10^{-7}$  Pa L s<sup>-1</sup> at operating temperature, which is approximately ten times lower than similar commercial Li sources. The outgassing rate of the oven is only limited by nitrogen contamination of the loaded Li metal and can therefore be reduced with straightforward improvements to our Li preparation. In chapter 5 we also discussed another low-outgassing technique for producing Li vapor is light-induced atomic desorption (LIAD) which has been demonstrated for Rb and Na.<sup>139,140</sup> When a Li-coated surface is exposed to UV light, Li atoms desorb from the surface and can be captured by a MOT. We have loaded Li atoms from a LIAD source into a MOT in sufficient quantities for operation of the pCAVS (although the 3D-printed titanium source allows MOT loading at a much higher rate.) A LIAD source is ideal for measuring XHV pressures because it is non-thermal: any vacuum pressure increase will be rapidly erased when the UV light is extinguished. Both the 3D-printed titanium source and the LIAD source could be used to load the pCAVS, or a commercially available effusive source; the preferable source will

be determined by the target measurement range and necessary Li loading rate. The prototype version that currently operates in the lab uses a commercial source and a mechanical shutter to reduce this contamination.

The optical access requirements of a MOT can be substantially reduced by using diffraction gratings. A single laser beam incident upon a 2D diffraction grating can generate all the beams needed to form a MOT. Such an optical configuration has been used to trap Rb.<sup>141</sup> We have adapted this technique for trapping of Li, which is complicated by the high operating temperature of Li sources and the comparatively weaker confinement of diffraction grating MOTs compared to traditional MOTs. A photograph of our nanofabricated grating chip is shown in Fig. (9). A Li grating MOT, combined with a low-outgassing Li source, in a suitably compact package constitutes our first generation pCAVS. The lowest detectable pressure for this device is limited by the large depth of the MOT (which increases the fraction of glancing collisions, making cross sections much more difficult to compute). The second generation pCAVS integrates a miniaturized magnetic trap to allow primary sensing of even lower pressures, with reduced systematic uncertainties associated with light-induced collisions.

The expense of a pCAVS device will limit its application space. The most promising avenue to reduce the cost to the final user is to optimize the pCAVS for use in large facilities where more than one device will be required. Since the laser system is the most expensive element by far, a large savings is realized by using a single laser system

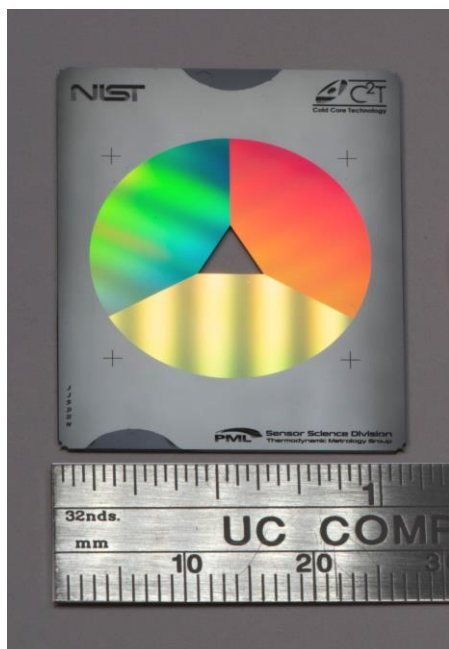


*Figure 7-2: Photograph of the prototype CCT triangular grating chip, with ruler.*

to operate two or more pCAVS (multiplexing). We have secured patent protection of this technology<sup>142</sup>, and as of writing, several commercial entities have expressed interest in developing the pCAVS into a product.

## 7.2 A closer look at systematics

The preliminary data of Figure 5-3 (b) indicated that the CAVS would be a good pressure sensor. With additional effort to understand and quantify the loss mechanisms and sources of uncertainty, we can fully characterize and qualify the pCAVS as a primary standard as well as an absolute sensor. We discuss the consequences of our choice of sensor atom species and type of trap on the eventual uncertainty of a pressure measurement, as well as the effect of glancing or quantum diffractive collisions following Eckel et. al.<sup>115</sup>

The physics basis of this measurement technique is the collision cross section between a sensor atom (cold) and a background particle (hot). This depends strongly on



the long-range potential and is dominated by the van der Waals interaction, which scales like  $-C_6/r^6$ , enabling us to estimate the loss rate coefficients for arbitrary sensor and background species. It turns out that the loss rate coefficients  $K$  are sensitive to  $C_6$ ,  $m_{\text{hot}}$ , and  $T$ , but surprisingly not  $m_{\text{cold}}$ .

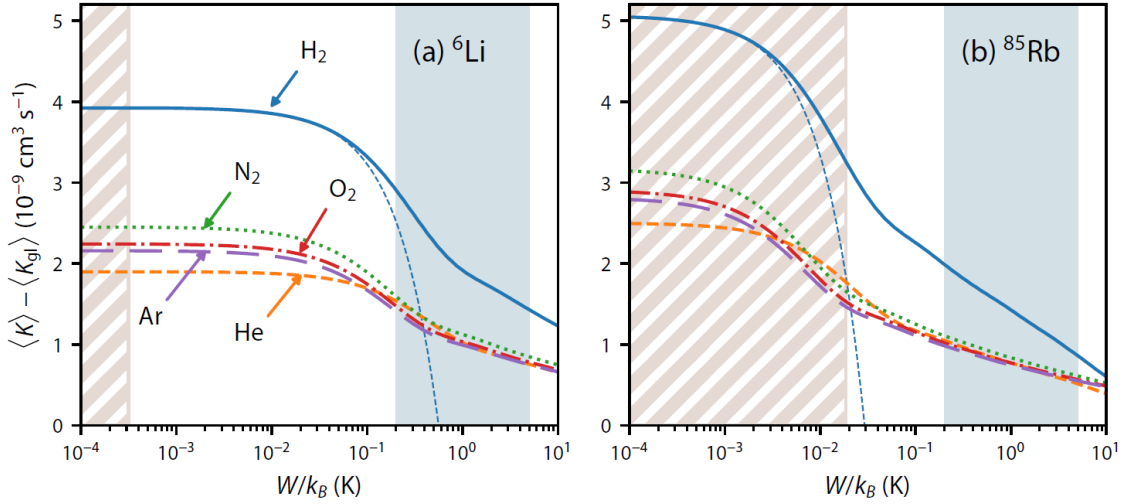


Figure 7-3 Glancing collision-corrected loss rate coefficient for ground state  $^6\text{Li}(^2S)$ , pane (a), and  $^{85}\text{Rb}(^2S)$ , pane (b) as a function of trap depth for various background gases at  $T = 293$  K. The result to first-order only is shown for  $\text{H}_2$  (thin-dashed curve), indicating the range over which it is applicable. The red-striped (blue) shaded regions highlight the accessible range of trap depths with a magnetic (magneto-optical) trap.

To eject an atom, the final kinetic energy thereof must be at least the trap depth  $W$ . There exists a critical scattering angle  $\theta_c$  for which atoms are *just* ejected from the trap. For scattering angles less than  $\theta_c$  atoms are not ejected, these are glancing or quantum-diffractive collisions. The existence of these glancing collisions means that we can't assume 1-1 correspondence between collisions and ejections, so 5.3 is corrected to

$$p = \Gamma k_B T / (\langle K \rangle - \langle K_{gl}(W) \rangle) \quad 7.1$$

A detailed calculation of these corrected loss rate coefficients is carried out by colleagues in Eckel et. al.<sup>115</sup>, Figure 7-3 shows the results.

Some interesting features emerge. First, for the same background gas, the loss rate coefficient for Rb is larger than for Li. This is because Rb has the larger van-der-Waals coefficient (surprisingly *not* because it's more massive). Second, the loss rate coefficient for H<sub>2</sub> is twice as large as for other gases, due primarily to its smaller mass. Third, the behavior is linear (dashed blue lines) until  $[\langle K \rangle - \langle K_{gl}(W) \rangle] / \langle K \rangle \approx 0.9$ , at which point it gives way to a logarithmic dependence on  $W$ .

Since our design allows for realization of either a MOT or a quadrupole magnetic trap, and the details of each are different, we have to consider them separately.

Fluorescence imaging is used in both cases to ascertain the trap size. In the case of the MOT this can be done continually since laser light is always present, but in the case of the magnetic trap, imaging is destructive so the trap needs to be reformed (and the stopwatch restarted) following each interrogation. Because of this, each run in the magnetic trap yields only one point on the decay curve. Therefore many more runs and much more time are needed to measure the loss rate for the magnetic trap. But as we will discuss, the tradeoff is that as a pressure sensor the magnetic trap is more accurate, and at deep vacuum timescales tend to be long anyway.

### 7.3 Fast Operation – the MOT as pressure sensor

When one chooses to operate the pCAVS with the MOT as pressure sensor, some systematic uncertainties arise as mentioned above. Of these, glancing collisions dominate, so it's important to characterize the trap depth well in order to correct for this term. Two methods for determining trap depth have been developed: (1) inducing two-body loss with a catalyst laser<sup>143</sup>, and (2) comparing the background-gas induced MOT loss rates to those of a magnetic trap with known depth<sup>144</sup>. These two methods have been

shown to yield identical results but are impractical to implement in a sensor like the pCAVS. Instead, we rely on models that have been demonstrated to agree quantitatively with these measurements. Following Ritchie *et. al.*,<sup>145</sup> we model the MOT trap depth for the pCAVS with the beam geometries, polarizations, and magnetic field specific for our device as shown in Figure 7-4, and the equations of motion from Eckel *et. al.*<sup>115</sup>

A single laser beam diffracts to form additional beams with no zero-order reflection. Only the incident beam and the diffracted beams pointing inward contribute to

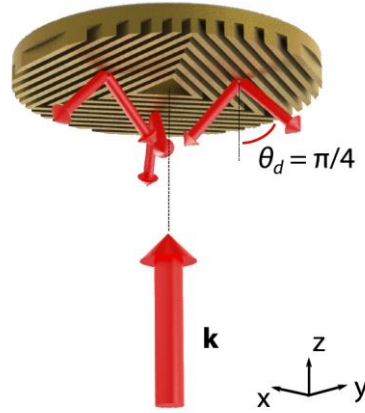


*Figure 7-4 Geometry of the pCAVS grating. A single laser beam (large red arrow) is diffracted into six beams (small red arrows) by three reflective gold diffraction gratings whose lines form superimposed triangles and diffract light at  $\theta_d = \pi/4$  with respect to the normal of the grating ( $-\hat{z}$ ). Grating lines are not to scale.*

forming the MOT. The magnetic field is produced by permanent magnets, and does not set the center of the trap. We find the trap center  $\mathbf{r}_0 = (0, 0, z_0)$  by placing atoms at rest at  $\mathbf{r} = 0$ , integrating the equations of motion, and following its damped motion to the center.

The temperature of the cold-atom cloud is small compared to the trap depth, therefore the atoms are initially concentrated near the center of the trap. After a collision with a background particle, they acquire momentum  $\mathbf{q}_c$  directed at azimuthal angle  $\varphi$  and polar angle  $\theta$  in the laboratory frame. Then to determine trap depth  $W$ , we can

numerically integrate the equations of motion starting from the center of the trap. For each pair of  $(\theta, \phi)$ , the trap depth  $W(\theta, \phi)$  is given by the initial kinetic energy  $q_e^2/(2m_c)$  where  $v_e = q_e/m_c$  is the escape velocity.

The anisotropy of  $W(\Delta, \phi)$  complicates our calculation of the loss rate coefficients for

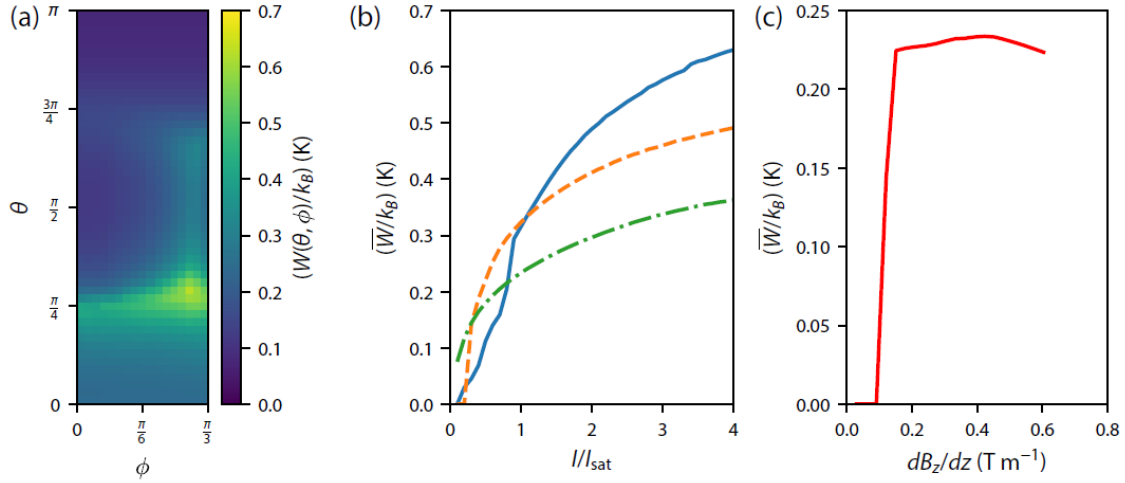


Figure 7-5 Trap depth for a typical three-beam grating MOT for Li. (a) angularly-resolved  $W(\Delta, \phi)$  for an incident beam at saturation intensity and with detuning  $\Delta/\gamma = -1$  and  $dB_z/dz = 0.5$  T/m. (b) Average trap depth as a function of incident beam intensity for detunings  $\Delta/\gamma = -3.0$  (solid blue),  $-2.0$  (dashed orange), and  $-1.0$  (dashed-dot green) with  $dB_z/dz = 0.5$  T/m. (c) Average trap depth as a function of magnetic field gradient at saturation intensity and with detuning  $\Delta/\gamma = -1$ .

glancing collisions. To understand the dependence on detuning and intensity of the incoming beam, we take an angularly averaged trap depth  $\overline{W}$ . The results of the trap depth simulation are shown in Figure 7-5. The uncertainty in pressure due to uncertainty in MOT trap depth is suppressed (it has logarithmic dependence) which is fortunate as we only know  $W$  to a few tens of percent through this simulation.

The second largest contribution to the uncertainty in a pressure measurement comes from the fact that some fraction of atoms are in the excited (P) state, which has different  $C_6$  coefficients than the ground (S) state. We estimate that the likelihood of

being in the P state is  $P_{\text{ex}} \approx 25\% \pm 12\%$ , leading to a fractional uncertainty of about 3% in the pressure measurement for both Li and Rb.

Lastly, an additional contribution to uncertainty from light-assisted collisions is considered but dismissed, as our data show no third- or higher-order decay, and 2nd-order decay can be accurately separated from exponential loss while fitting the data.

#### 7.4 Accurate Operation – the magnetic trap as pressure sensor

Unlike MOTs, magnetic traps are conservative traps: an atom's kinetic energy must decrease by the same amount as its internal energy increases. A consequence of this is that only states whose internal energy  $E$  increases with magnetic field  $|\mathbf{B}|$ , i.e.  $dE/dB > 0$ , can be trapped.

The energy of the internal states of  ${}^6\text{Li}(^2\text{S})$ ,  ${}^7\text{Li}(^2\text{S})$ , and  ${}^{85}\text{Rb}(^2\text{S})$  are shown in Figure 7-6, including effects of the hyperfine and Zeeman interactions. The former gives rise to two non-degenerate states at  $\mathbf{B} = 0$ , denoted by  $F = I \pm 1/2$ , where  $I$  is the nuclear spin. For  ${}^6\text{Li}$ ,  ${}^7\text{Li}$ , and  ${}^{85}\text{Rb}$ ,  $I = 1$ ,  $3/2$ , and  $5/2$  respectively. For non-zero  $B$ , the levels split according to projection  $m_F = -F, -F + 1, \dots, F$ . In the limit  $B \rightarrow \infty$ , magnetic traps are infinitely deep for states with  $F = I + 1/2$ , so these states are impractical for pCAVS operation. Instead we focus of the state  $\langle F = I - 1/2, m_F = -(I - 1/2) \rangle$  which has a maximum energy at a finite  $B_{\text{max}}$  and a trap depth  $W_{\text{max}} = E(B_{\text{max}}) - E(B = 0)$ .

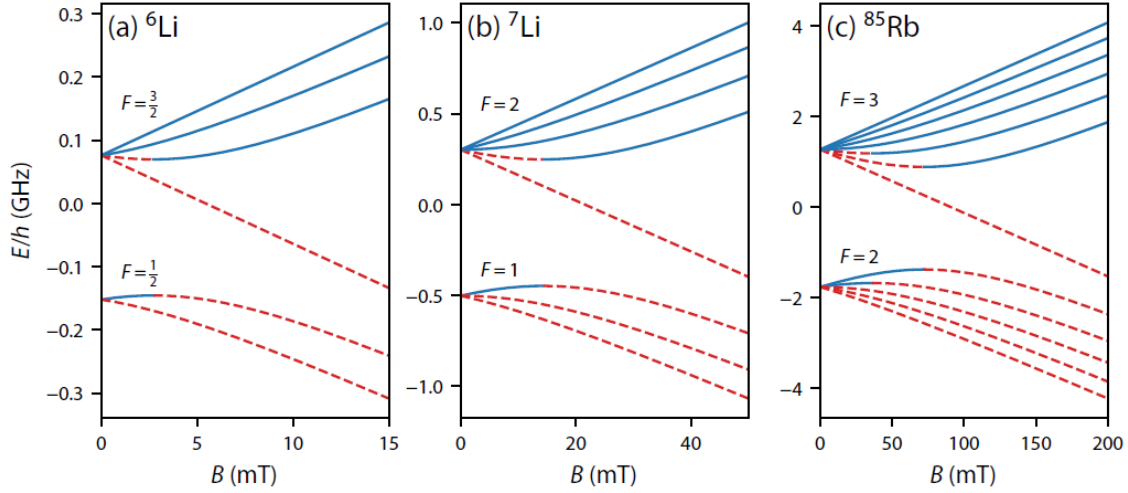


Figure 7-6 Energy of the magnetic sublevels as a function of magnetic field for  ${}^6\text{Li}$  (pane a),  ${}^7\text{Li}$  (pane b) and  ${}^{85}\text{Rb}$  (pane c). Blue solid curves correspond to states that are magnetically trappable, Red dashed curves depict states that have negative slope and thus are not magnetically trappable.

The characteristic spatial extent of the magnetically trapped cloud  $z_t$  ranges from 5 mm for  ${}^6\text{Li}$  to 1600 mm for  ${}^{87}\text{Rb}$ . The size of the initial cold atom cloud is set by the MOT that loads it into the magnetic trap. The initial temperature out of the MOT is  $\lesssim 1\text{mK}$ , which leads to a cloud size  $z_c \approx 5\text{ mm}$  for Li and  $z_c \approx 20\text{ mm}$  for Rb. For  ${}^6\text{Li}$ , this causes some loss of atoms when transferred from the MOT to the magnetic trap, while for Rb the cloud will expand into the grating. This may require increasing the magnetic field gradient to reduce the size of the initial cold-atom cloud in order to prevent the atoms from sticking to the grating.

As with the MOT-based pCAVS, glancing collisions complicate the loss rate of atoms from a magnetic trap. Rather than ejecting an atom (which appears as exponential decay) glancing collisions warm the gas and lead to evaporative losses in an accelerating process. We expect that this will cause non-exponential decay, and is thus separable from the loss rate of interest. Finally, because of practicality concerns, we use a quadrupole

magnetic trap which of course has a magnetic field zero. This means that our grating-based trap is susceptible to Majorana loss as well.

### 7.5 Direct comparison of two prototype pCAVS

Using a combination of off-the-shelf components, 3D printed parts, and our grating chip, we built two nominally identical pCAVS. These consist of a source chamber and a measurement chamber separated by a differential pumping tube 2.67 cm long and 3 mm in diameter, yielding a vacuum conductance of approximately 0.014 L/s For  $N_2$  at 300 K. A 3D printed Ti mechanical shutter can effectively block the source from injecting atoms into the measurement chamber. A NEG pump with 100 L/s pumping speed for  $H_2$  is included to capture byproduct contaminants released by the effusive source.

Input beams incident on the grating chip are prepared using external beam shaping optics, which can be made relatively compact (20 cm or less in length). The magnetic field for the MOT is generated by NdFeB permanent magnets mounted to the exterior of the chamber by 3D printed mounts. The grating chip has a novel feature: an aperture in the center of the chip allows atoms to be loaded from the back, moving toward the trapping region opposite the direction of propagation of the input beam. This quirk of geometry greatly increases our capture velocity by itself, but furthermore provides space for a Zeeman slower to be inserted around the differential pumping tube between the source and the chip surface without interfering with the trapping light. We note that though the laser beam is well aligned to the chip, the chip normal and the differential pumping tube axis may be out of parallel by several degrees.

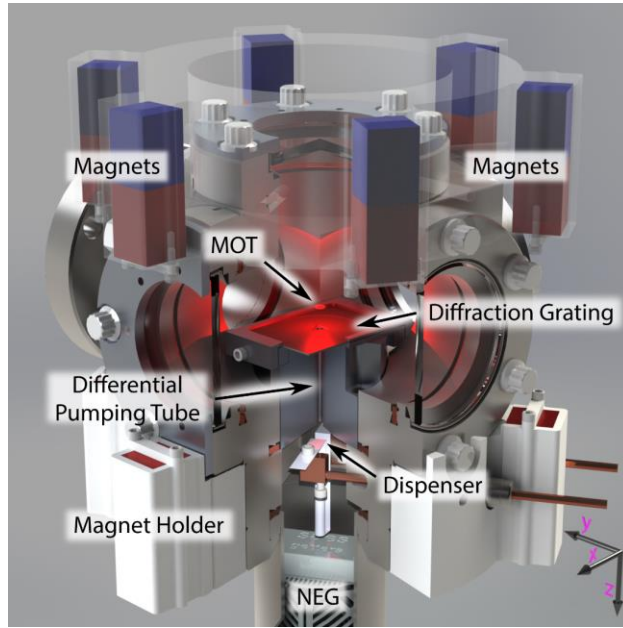


*Figure 7-7 CAD rendering of a prototype pCAVS. The total vertical size is about 10 cm. The atomic shutter is not shown, it fits snugly between the dispenser and the differential pumping tube.*

The input laser is tuned to be roughly  $-9$  MHz detuned from the  $^2S_{1/2}(F=2) \rightarrow ^2P_{3/2}(F'=3)$  transition in  $^7\text{Li}$ , which has linewidth  $2\pi \times 5.87$  MHz. An electro-optic modulator (EOM) before the fiber produces sidebands at  $\pm 813$  MHz, with the blue sideband resonant with the  $^2S_{1/2}(F=1) \rightarrow ^2P_{3/2}(F'=2)$  transition. The sidebands have roughly 50% of the power of the carrier, as measured using a Fabry-Perot cavity. A  $1 \times 4$  fiber switch can select to which pCAVS the laser light is sent. The switch operates with about 6 dB of loss and requires approximately 100 ms to actuate between the two output fibers. The two outputs have roughly 20 mW of total power and a peak intensity of 12 mW/cm<sup>2</sup>, approximately four times the saturation intensity.

We mounted the two pCAVS on a single vacuum chamber with direct line-of-sight to each other, so that they should be at the same pressure. The vacuum components were vacuum baked before assembly to remove hydrogen, and again after assembly at



low temperature to desorb water (see Chapter 4:). The operation of a pCAVS follows this procedure: The source shutter is opened, and atoms allowed to flow into the trapping region. The EOM is turned on and light is injected into the pCAVS for 2 seconds, forming a MOT with about  $10^5$  atoms. The shutter is closed and atoms are allowed to transfer into the  $^2S(F = 1)$  hyperfine state (EOM turned off). The laser is then turned off entirely, and about  $10^4$  atoms with projection quantum number  $m_F = -1$  with respect to the local magnetic field direction congregate at the location of zero magnetic field. We vary how long the atoms are held in this quadrupole trap in order to diagnose the loss rate. In order to count the remaining atoms after time  $t$ , we recapture them into a MOT. This entire procedure is completed for one pCAVS device before switching the laser to and beginning the procedure for the other. In order to ascertain a decay curve, this is repeated for a variety of times  $t$ .

As can be seen in Figure 7-8, the results for the two pCAVS devices reveals a discrepancy. Each of the curves is fit to  $N/N_0 = Ae^{-\Gamma t}$ , where  $A$  and  $\Gamma$  are parameters. For equal pressures, the slopes ( $\Gamma$ ) should be the same but clearly are not. We set out to troubleshoot the discrepancy, initially assuming it to be due to a problem with the

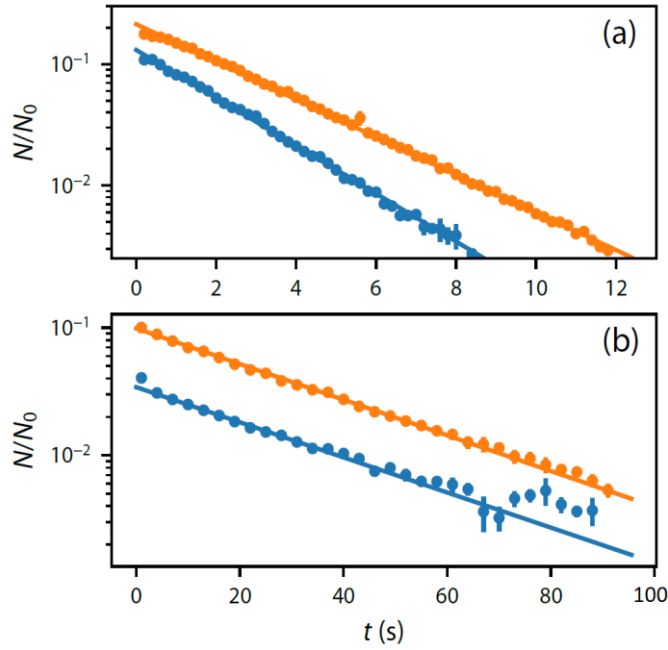


*Figure 7-8 Recaptured atom number vs time  $t$ . The blue points are for pCAVS #1 and the orange are for pCAVS #2. These example decays were captured before (a) and after (b) repairing a leak.*

apparatus, but no issues were discovered.

Unless our entire premise is wrong, it must be the case, then, that the two devices were actually detecting *different* local pressures. The simplest cause of local pressure variation in a system like ours is a leak. We can estimate the size of the presumed leak using the pressures measured by pCAVS #1 and pCAVS #2. We assume  $K = 2.5 \times 10^{-9} \text{ cm}^3/\text{s}$  (this is the semi-classical estimate for  $\text{N}_2$ , the primary constituent of room air) and room temperature  $T = 295 \text{ K}$ . From the data in Figure 7-8, the pressure in pCAVS #1 is  $7 \times 10^{-7} \text{ Pa}$ , and that in pCAVS #2 is  $6 \times 10^{-7} \text{ Pa}$ , giving a pressure difference of  $1 \times 10^{-7} \text{ Pa}$ . With

estimated pumping speed 10 L/s at each pCAVS, the leak rate is on order  $10^{-6}$  Pa L/s (equivalent to a flow of about  $10^{-13}$  mol/s). This leak rate is small, but can be seen using an RGA with an electron multiplier. We attached such an RGA to the system and verified location of the leak and its predicted size via helium leak testing.

With the leak repaired, we repeated our comparison, and now the two pCAVS devices appear to measure equal decay times, see Figure 7-8 pane (b).

We can now calculate the pressure in the vacuum chamber and its uncertainty including potential systematic shifts inherent in the operation of the pCAVS, and assuming the dominant background gas is  $H_2$ . We revisit equation 5.3, which describes the fundamental relationship between the pressure and decay rate,

$$p = \frac{\Gamma}{\langle K \rangle} k_B T$$

And rewrite it to include glancing collisions (those which fail to transfer enough energy to eject the sensor atom from the trap) and other loss mechanisms due to 2- or 3-body collisions between sensor atoms, or those inherent to the quadrupole trap (i.e., Majorana losses):

$$p = \frac{\Gamma - \Gamma_{other}}{\langle K_{H_2} \rangle \times [1 - f_{gl}(W)]} k_B T \quad 7.2$$

where  $\Gamma_{other}$  captures other loss mechanisms and  $f_{gl}$  is the fraction of glancing collisions given a quadrupole trap depth  $W$ . The background gas temperature  $T = 301.7(1.6)$  K (uncertainty here arises primarily from a gradient across the chamber, as well as drift and a small calibration uncertainty). The rate coefficient for Li and  $H_2$  has been calculated *a priori*<sup>146</sup>  $K_{H_2} = 3.18(6) \times 10^{-9}$  cm<sup>3</sup>/s. The glancing collision fraction is estimated to be  $f_{gl} = 3.2(1.7) \times 10^{-3}$ , for trap depth  $W/k = 1.5(3)$  mK. The decay due to other loss

mechanisms is consistent with zero. See Ehinger<sup>147</sup> for a more detailed treatment of these terms. Combining this information, we arrive at results for our two pCAVS devices:

Device	Pressure measurement
pCAVS #1	$41.5(1.2) \times 10^{-9}$ Pa
pCAVS #2	$42.2(1.0) \times 10^{-9}$ Pa

This measurement is of the base pressure in the system, and is somewhat higher than we'd expect given the careful material selection and treatment motivated in Chapter 4:. The pressures we're seeing are in fact due to contamination from the effusive Li sources, which operate around 400°C. Although we have NEG pumps incorporated into the devices, some fraction of the source outgassing will escape through the differential pumping tube. The additional gas load will scale exponentially with AMD temperature, which in turn is determined by the balance of electrical power dissipated within the AMD

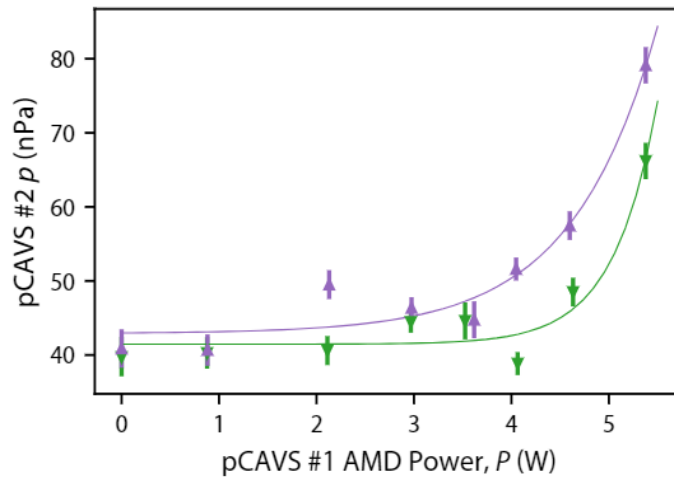


*Figure 7-9* Pressure measured by pCAVS #2 as functions of power  $P$  dissipated in pCAVS #1 with its shutter open (purple) or closed (green).

(about 3 W) and the flow of heat out. For our operating temperature of 400°C, radiative loss is negligible, and the temperature rise of the AMD is proportional to the dissipated power.

To quantify this effect, we used one of the devices (pCAVS #2) to measure the additional gas load produced by operating the other device (pCAVS #1). See Figure 7-9. At our typical operating power of 3 W, the resulting outgassing rates  $q(P)$  can be extracted from exponential fits,  $q(P) = q_0[\exp(P/P_0 - 1)]$ . The fit parameters  $p_0$ ,  $q_0$ , and  $P_0$  correspond to the chamber base pressure, the AMD outgassing rate coefficient, and the activation power for the outgassing process, respectively. These are  $2 \times 10^{-8}$  Pa L/s with the pCAVS #1 shutter open, and  $1 \times 10^{-9}$  Pa L/s with the shutter closed, corresponding to pressure increases of 2 nPa and 0.1 nPa respectively. These results indicate that the AMD is the predominant source of additional gas load, and that other options for sources as discussed in section 6.3 should be considered as next-generation devices are developed.

Currently the pCAVS can measure pressure throughout the UHV regime with accuracies ranging from 1% at  $10^{-6}$  Pa to about 30% at  $10^{-9}$  Pa. This level of accuracy meets requirements for leak triangulation in the next generation of the gravitational wave detectors and accelerator experiments, and makes the pCAVS a good transfer standard for ion gauge and RGA calibrations. To achieve lower uncertainties, more work needs to be done to understand the contribution of Majorana loss. This can be mitigated either through analysis (if the time-dependence of Majorana loss is other than exponential, it's contribution can be subtracted from the fit) or by refining the magnetic trap to have no field zero. We can also reduce statistical uncertainty by more averaging; the tradeoff is that at low pressures the integration time is already hours or even days at the lowest pressures. For certain applications this may be acceptable, as any excursions from a long-term base pressure monitoring measurement would still be detected more-or-less immediately. There is also room to improve the signal-to-noise in the pCAVS by

increasing the atom number from about  $10^5$  to about  $10^7$ , which can be accomplished by better aligning the laser, differential pumping tube, and diffraction grating chip.

## Chapter 8: Measurement of loss rate coefficient and comparison to theory

This entire project hinges on the idea that vacuum measurement can be traceable to collision cross sections. A working *sensor* need only transduce pressure, all that's required is a well-characterized, preferably linear relationship between the signal output, and the quantity of interest. But how does one know this relationship? Usually through calibration against another device with known relationship, and so on through potentially many steps, until reaching a fundamentally primary or functionally-primary standard. The output of the *standard* must be known through a combination of calculation and definition, and often “realizes” or generates a quantity, rather than sensing it. Our device is simultaneously a standard and a sensor, wherein the traceability to pressure comes from knowledge of cross sections.

In order to test that the CAVS and pCAVS work, and to verify the results of our theoretician colleagues, we invert this process and realize a vacuum pressure via a traditional technique, then sensing that pressure with the CAVS or pCAVS allows us to measure the loss rate coefficient. These are compared with theory for a small selection of gases. In section 5.2 we discussed the technique for measuring cross sections of an arbitrary gas ratiometrically, such measurements are planned for the future.

### 8.1 Brief Review of Analysis

We begin by listing the important quantities and equations, most of which have been introduced earlier:

$\Gamma$	Loss rate, determined experimentally
$\Gamma_0$	Background loss rate

$K$	First order loss rate coefficient, determined from theoretical collision cross sections.
$K_2$	Second-order loss rate coefficient, largely due to glancing collisions.
$\rho_h$	Density of the hot background gas, directly relatable to pressure.
$\rho_c$	Density of the cold trapped atom cloud
$\dot{n}$	Flow injected by flowmeter into dynamic expansion system
$R_p$	Pressure ratio in dynamic expansion system ( $P_{\text{upper}}/P_{\text{lower}}$ )
$C$	Conductance of orifice
$k_B$	Boltzmann constant
$R$	Gas constant, $R = N_A \times k_B$
$T$	Temperature of the background gas (generally room temperature)

Equation 5.2 tells us the loss rate and loss rate coefficient are related through the density of the hot gas, our proxy for pressure. It is reproduced here:

$$\Gamma = \rho_h K \quad 8.1$$

When operating the CAVS as a pressure sensor, we use calculated  $K$  and measured  $\Gamma$ , but here we want to extract  $K$  given a known pressure. To do this we use the ideal gas law:

$$K = \frac{\Gamma - \Gamma_0}{\rho_h} = \frac{(\Gamma - \Gamma_0)k_B T}{p} \quad 8.2$$

If we had perfect 1-1 correspondence between collisions and ejections, and if we could achieve perfect vacuum,  $\Gamma_0$  would be zero. In the lab under real-world conditions, it is dominated by two-body loss. From Equation 2.1, the pressure in the dynamic expansion system is

$$p_{\text{upper}} = \frac{\dot{n}RT}{C} \frac{R_p}{R_p - 1} \quad 8.3$$

Where  $\dot{n}$  is known from equations 6.5 and 6.12, and possibly 6.7 if using the flow splitter.

Finally we can write down the measurement equation for  $K$ :



$$K = \frac{k_B}{R} \frac{(\Gamma - \Gamma_0)C}{\dot{n}} \frac{R_p - 1}{R_p} = \frac{1}{N_A} \frac{(\Gamma - \Gamma_0)}{\dot{n}} \frac{R_p - 1}{R_p} \quad 8.4$$

A corresponding uncertainty statement is produced in the usual way by taking partial derivatives of the measurement equation. If we write  $\Gamma' = \Gamma - \Gamma_0$ , then the relative uncertainty in  $K$  is given by

$$\left(\frac{u_K}{K}\right)^2 = \left(\frac{u_{\Gamma'}}{\Gamma'}\right)^2 + \left(\frac{u_C}{C}\right)^2 + \left(\frac{u_{\dot{n}}}{\dot{n}}\right)^2 + \left(\frac{1}{R_p - 1} \frac{u_{R_p}}{R_p}\right)^2 \quad 8.5$$

## 8.2 Procedure and results

Cross section measurements have been fully carried out for He, Ar, and N<sub>2</sub>.

Additional gases Xe, Ne, Kr, and H<sub>2</sub> are planned for the near future. These measurements have been done in both the CAVS and the pCAVS, the latter has been outperforming our expectations, so much so that future work may exclude the CAVS completely. We also find that the systematic errors associated with using Rb as sensor atom are significant, confirming our prediction that Li will be the more useful choice.

Our theoretician colleagues have completed calculated cross sections for a number of combinations of sensor atom and background gas. At the time of writing, the subset of these that has been published<sup>132,133,146</sup> consists of:

*Table X Published elastic loss rate coefficients, errors are reported at the  $k = 1$  level.*

Sensor Atom	Background Gas	Loss Rate Coefficient $K_0(\text{cm}^3/\text{s})$
<sup>6</sup> Li	H <sub>2</sub>	$3.13(6) \times 10^{-9}$
<sup>7</sup> Li	H <sub>2</sub>	$3.18(6) \times 10^{-9}$
<sup>6</sup> Li	He	$1.467(13) \times 10^{-9}$
<sup>7</sup> Li	He	$1.471(13) \times 10^{-9}$

We restrict our experimental comparison to this subset. We have attempted to measure  $\text{H}_2$ , but discovered a systematic effect wherein the pressure in the chamber decreases over the course of a measurement. We are currently exploring this issue, and expect the cause is gettering by titanium elements of the flowmeter. Functionally this means that we can only compare  ${}^7\text{Li} \times \text{He}$ . The disappointed reader is assured that publications in the near future will discuss other species. To risk further disappointing the reader, we are currently configured to run Rb, not Li in the CAVS. But since we've demonstrated that the pCAVS works as expected and with better-than-expected accuracy, we can perform the cross section measurement using the pCAVS.

Initial background data must be taken following a long evacuation of the flowmeter and DE system, so as to reach the ultimate pressure of the system as it's currently configured. We learned that these tend not to change over the course of several days, so generally one background run is taken at the beginning of each week, one example run is shown in Figure 8-1. The outgassing rate of the flowmeter and DE system must be measured daily. Following this measurement, the flowmeter is filled to a fill pressure that's predicted to result in the desired DE pressure. Because the flowmeter measures as well as generates the pressure, it's not necessary to reach an exact fill pressure. This sets a known pressure to which we subject our trapped atoms. We then run

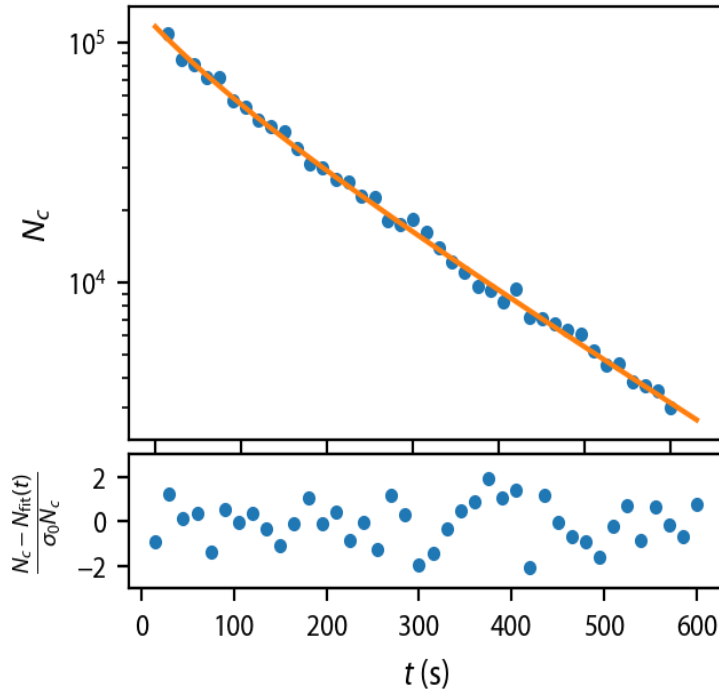


*Figure 8-1 Example Background data. The decay is approximately exponential (straight line), but some curvature on this plot indicates two-body processes are present.*

the pCAVS in accurate mode: atoms are captured in a MOT and transferred to a magnetic trap, then allowed some time to interact with the background pressure before being subjected to destructive imaging. We do this for approximately thirty hold times to adequately sample the loss rate  $\Gamma$ . Our minimum signal to noise is reached when we have about 1,000 trapped atoms, which sets the upper limit of our hold time for a given pressure. We repeat this decay rate measurement over as many DE-set pressures as feasible. Figure 8-2 shows a set of decay curves for the  $^7\text{Li} \times \text{He}$  system.

To find the loss rate coefficient  $K$  we need to fit these decay curves to extract  $\Gamma$  and reject  $\Gamma_1$  and any higher order terms. The loss rate  $\Gamma_0$  of the background ultimate pressure is found similarly and subtracted out. The fill pressure of the flowmeter is used

to calculate the set pressure in the DE system, along with the measured pressure ratio  $R_p$  from Table VIII for the gas under investigation, in this case helium.

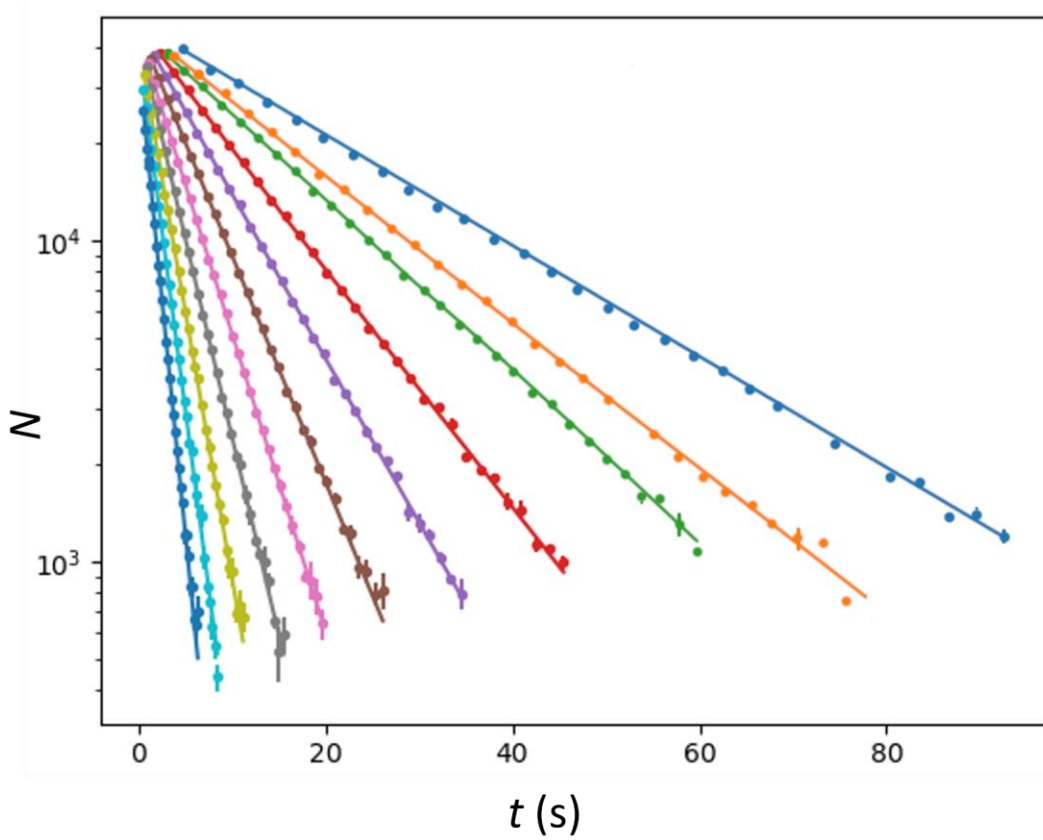


*Figure 8-2 decay curves for  $7\text{Li} \times \text{He}$  at a number of different helium pressures. Color encodes fill pressure which scales with chamber pressure, higher slopes are higher pressures. From left to right, fill pressures in torr are 7.50 (blue), 5.62 (teal), 4.22 (peridot), 3.16 (gray), 2.37 (pink), 1.78 (brown), 1.33 (violet), 1.00 (red), 0.75 (green), 0.56 (orange), 0.42 (navy).*

The loss rate  $K$  is expected to be independent of pressure, so a plot of  $K$  vs  $P$  should describe a horizontal line, see Figure 8-3.

We can now compare the measured loss rate coefficient to the calculated loss rate coefficient, and we find they agree within the error bars. See Table XI.

*Table XI: Theoretical and experimentally determined first order loss rate coefficient for  ${}^7\text{Li} \times \text{He}$ .*

${}^7\text{Li} \times {}^4\text{He}$	
$K_{\text{thr}} (10^{-9} \text{ cm}^3/\text{s})$	1.66(4)
$K_{\text{exp}} (10^{-9} \text{ cm}^3/\text{s})$	1.69(1)
Difference	0.04(5)

This is the first species for which we can make this comparison, more are to follow. As more data are taken and analyzed, we may find evidence of systematic errors not captured in this initial result.

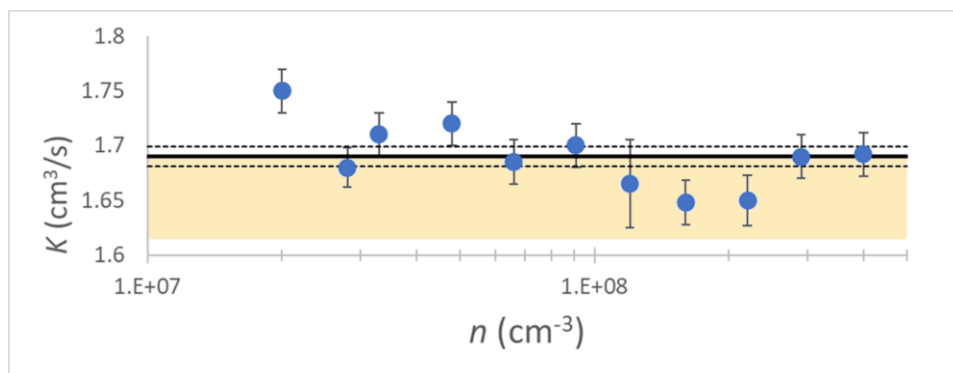


*Figure 8-3 Loss rate coefficient  $K$  vs Pressure in the pCAVS for the  ${}^7\text{Li} \times \text{He}$  system. Error bars are calculated as described in the text. The solid horizontal line shows the weighted mean of these experimental values, dashed lines are at one standard deviation of the mean. The gold band is the  $k = 1$  confidence interval for the theoretical value.*

### 8.3 Closing remarks

This project is one of several at NIST that embody a shift from traditional metrology to so-called quantum-based metrology. The traditional method for measuring vacuum is to use an ionization gauge, which is calibrated on a dynamic expansion system. This in turn is traceable back to other pressure gauges and ultimately a primary pressure standard that operates at a completely different range. There are a number of links in this traceability chain, at each link uncertainty is accrued, and at each link lies the opportunity for something to go wrong.

Now with a quantum-SI device, the end user no longer has to rely on a chain of calibrations but can access the SI directly through an interrogation of a device that links the quantity she's trying to measure to a fundamental, unchanging physical property. In the case of the CAVS, this is the collision cross section, which relates back to the dynamic polarizability of the particles. Though the CAVS and pCAVS are relatively expensive and hard to operate, for certain applications and users the advantages are great, and hopefully as we work to form industry partnerships, we'll be able to make the technology more accessible.

Leading up to the project described in this thesis, a number of other attempts were made by other NIST researchers to develop new types of pressure metrology, these were reviewed in Chapter 3:, and are concerned with higher pressure ranges. In particular, the FLOC has been the subject of extensive research and investment and is on the cusp of release as a commercial device. In order to establish the CAVS at the lowest pressure ranges, we had to develop and refine methods for achieving UHV and XHV pressures in the first place. Likewise we had to test materials and treatments, as well as develop

diagnostic procedures to ensure those materials behaved as needed. The results of these investigations described in Chapter 4:are relevant for a wide range of research and applications that make use of deep vacuum.

The concept of the CAVS is trivial, but its utility to the metrology community depends upon a deep and rigorous treatment of uncertainties, and an honest accounting of what can go wrong. This is what makes the CAVS and pCAVS a standard and not just a sensor. In Chapter 5:the author reviews and summarizes her colleagues' efforts in this vein to date, though some questions remain outstanding.

The design and construction of the various parts of the experiment is presented in Chapter 6:As a development project from the ground up, this extensive discussion includes details about aspects of both the vacuum side and atom side, and includes information about tests and characterizations. Details about electronics and software development are omitted. We focus on the portable device pCAVS in Chapter 7:and present the results of a comparison between two nominally identical devices.

At the end of all of this reviewing, planning, background work, design work, building, and testing, we finally were able to measure cross sections and compare to theory. This is discussed in Chapter 8:These efforts are ongoing, to date only a few gases have been measured, but these confirm that we're on solid footing with the overall concept, and that refinement and extension are only contingent on doing the work. Our theoretician colleagues continually expand our roster of gases to test, and when they're eventually exhausted, we can do ratiometric comparisons to arbitrary gases that are of interest to the vacuum community.

It is hoped that our technology will be commercialized in a device based on the pCAVS, and that it will have other applications outside of vacuum metrology. Future work will explore these possibilities.



## Bibliography

1. Dylla, H. F. Development of ultrahigh and extreme high vacuum technology for physics research. *J. Vac. Sci. Technol. A Vacuum, Surfaces, Film.* **21**, S25 (2003).
2. Newell, D. B. Physics Today A more fundamental International System of Units. *Cit. Phys. Today* **67**, 35 (2014).
3. Possolo, A., Schlamminger, S., Stoudt, S., Pratt, J. R. & Williams, C. J. Evaluation of the accuracy, consistency, and stability of measurements of the Planck constant used in the redefinition of the international system of units. *Metrologia* **55**, 29 (2017).
4. Newell, D. B. *et al.* The CODATA 2017 values of h, e, k, and NA for the revision of the SI. *Metrologia* **55**, L13 (2018).
5. Lafferty, J. M. Review of Pressure Measurement Techniques for Ultrahigh Vacua. *J. Vac. Sci. Technol.* **9**, 101 (2000).
6. Redhead, P. A. History of ultrahigh vacuum pressure measurements. *J. Vac. Sci. Technol. A Vacuum, Surfaces, Film.* **12**, 904 (1998).
7. Redhead, P. A. Measurement of vacuum; 1950–2003. *J. Vac. Sci. Technol. A Vacuum, Surfaces, Film.* **21**, S1 (2003).
8. Calcatelli, A. The development of vacuum measurements down to extremely high vacuum – XHV. *Measurement* **46**, 1029–1039 (2013).
9. Batey, J. H. The physics and technology of quadrupole mass spectrometers. *Vacuum* **101**, 410–415 (2014).
10. Blessing, J. E., Ellefson, R. E., Raby, B. A., Brucker, G. A. & Waits, R. K.

- Recommended practice for process sampling for partial pressure analysis. *J. Vac. Sci. Technol. A Vacuum, Surfaces, Film.* **25**, 167 (2007).
11. Basford, J. A. *et al.* Recommended Practice for the Calibration of Mass Spectrometers. *J. Vac. Sci. Technol. A Vacuum, Surfaces, Film.* **11**, A22 (1998).
  12. Fedchak, J. A., Abbott, P. J., Hendricks, J. H., Arnold, P. C. & Peacock, N. T. Review Article: Recommended practice for calibrating vacuum gauges of the ionization type. *J. Vac. Sci. Technol. A Vacuum, Surfaces, Film.* **36**, 030802 (2018).
  13. Redhead, P. A. New Hot-Filament Ionization Gauge with Low Residual Current. *J. Vac. Sci. Technol.* **3**, 173–180 (1966).
  14. Helmer, J. C. & Hayward, W. H. Ion gauge for vacuum pressure measurements below  $1 \times 10^{-10}$  Torr. *Rev. Sci. Instrum.* **37**, 1652–1654 (1966).
  15. Akimichi, H., Tanaka, T., Takeuchi, K., Tuzi, Y. & Arakawa, I. Development of a new ionization gauge with Bessel Box type energy analyzer. *Vacuum* **46**, 749–752 (1995).
  16. Akimichi, H. *et al.* Improvement of the performance of the ionization gauge with energy filter for the measurement of an extremely high vacuum. *Vacuum* **47**, 561–565 (1996).
  17. Arnold, P. C., Bills, D. G., Borenstein, M. D. & Borichevsky, S. C. Stable and reproducible Bayard–Alpert ionization gauge. *J. Vac. Sci. Technol. A Vacuum, Surfaces, Film.* **12**, 580–586 (1994).
  18. Rushton, J. A., Aldous, M. & Himsworth, M. D. Contributed Review: The feasibility of a fully miniaturized magneto-optical trap for portable ultracold

- quantum technology. *Rev. Sci. Instrum.* **85**, 121501 (2014).
19. D. J. Melville. No Title. *Archimedes* **45**, (2016).
  20. Bock, T., Ahrendt, H. & Jousten, K. Reduction of the uncertainty of the PTB vacuum pressure scale by a new large area non-rotating piston gauge. *Metrologia* **46**, 389 (2009).
  21. Scherschligt, J., Olson, D. A., Driver, R. G. & Yang, Y. Pressure Balance Cross-Calibration Method Using a Pressure Transducer as Transfer Standard. *NCSLI Meas.* **11**, 28–33 (2016).
  22. Middleton, W. E. K. *The History of the Barometer*. (Johns Hopkins Press, 1964).
  23. Hendricks, J. H. & Olson, D. A. 1–15,000 Pa Absolute mode comparisons between the NIST ultrasonic interferometer manometers and non-rotating force-balanced piston gauges. *Measurement* **43**, 664–674 (2010).
  24. Ricker, J. *et al.* Final report on the key comparison CCM.P-K4.2012 in absolute pressure from 1 Pa to 10 kPa. *Metrologia* **54**, 1–37 (2017).
  25. Jousten, K., Menzer, H., Wandrey, D. & Niepraschk, R. New, fully automated, primary standard for generating vacuum pressures between 10–10 Pa and  $3 \times 10^{-2}$  Pa with respect to residual pressure. *Metrologia* **36**, 493 (1999).
  26. McCulloh, K. E., Tilford, C. R., Ehrlich, C. D. & Long, F. G. Low-range flowmeters for use with vacuum and leak standards. *J. Vac. Sci. Technol. A Vacuum, Surfaces, Film.* **5**, 376–381 (1987).
  27. Fedchak, J. A. & Defibaugh, D. R. Accurate conductance measurements of a pinhole orifice using a constant-pressure flowmeter. in *Measurement: Journal of the International Measurement Confederation* vol. 45 2449–2451 (Elsevier, 2012).

28. JCGM. *International Vocabulary of Metrology - Basic and General Concepts and Associated Terms (VIM 3rd edition)*. 18 (2008).
29. Quinn, T. J. Primary methods of measurement and primary standards. *Metrologia* **34**, 61 (1997).
30. Tilford, C. R., Dittmann, S. & McCulloh, K. E. The National Bureau of Standards primary high-vacuum standard. *J. Vac. Sci. Technol. A Vacuum, Surfaces, Film.* **6**, 2853–2859 (1988).
31. Hong, S.-S., Kim, J.-T. & Shin, Y.-H. Development of an in situ vacuum gauge calibration system. *Meas. Sci. Technol.* **19**, 015102 (2007).
32. Yoshida, H., Arai, K., Akimichi, H. & Hirata, M. Two-stage flow-dividing system for the calibration of vacuum gauges. *J. Vac. Sci. Technol. A Vacuum, Surfaces, Film.* **26**, 128 (2007).
33. Li, D., Guo, M., Cheng, Y., Feng, Y. & Zhang, D. Vacuum-calibration apparatus with pressure down to 10<sup>-10</sup> Pa. *J. Vac. Sci. Technol. A Vacuum, Surfaces, Film.* **28**, 1099 (2010).
34. Berg, R. F. & Fedchak, J. A. NIST Special Publication 250-93 NIST Calibration Services for Spinning Rotor Gauge Calibrations. doi:10.6028/NIST.SP.250-93.
35. Scherschligt, J. *et al.* Review Article: Quantum-based vacuum metrology at the National Institute of Standards and Technology. *J. Vac. Sci. Technol. A* **36**, 040801 (2018).
36. Looney, J. P., Harrington, J. E., Smyth, K. C., O'Brian, T. R. & Lucatorto, T. B. Measurement of CO pressures in the ultrahigh vacuum regime using resonance-enhanced multiphoton-ionization time-of-flight mass spectroscopy. *J. Vac. Sci.*

- Technol. A Vacuum, Surfaces, Film.* **11**, 3111 (1998).
37. Looney, P. J. No Title. *J. Vac. Soc. Japan* **37**, 703 (1994).
  38. Cool, T. A. Quantitative measurement of NO density by resonance three-photon ionization. *Appl. Opt. Vol. 23, Issue 10, pp. 1559-1572* **23**, 1559–1572 (1984).
  39. Hodges, J. T., Looney, J. P. & Zee, R. D. van. Response of a ring-down cavity to an arbitrary excitation. *J. Chem. Phys.* **105**, 10278 (1998).
  40. Looney, J. P., Hodges, J. T. & Zee, R. D. van. Laser bandwidth effects in quantitative cavity ring-down spectroscopy. *Appl. Opt. Vol. 35, Issue 21, pp. 4112-4116* **35**, 4112–4116 (1996).
  41. Zee, R. D. van, Looney, J. P. & Hodges, J. T. Measuring pressure with cavity ring-down spectroscopy. *Adv. Sensors Monit. Process Ind. Environ.* **3535**, 46–56 (1999).
  42. O’Keefe, A. & Deacon, D. A. G. Cavity ring-down optical spectrometer for absorption measurements using pulsed laser sources. *Rev. Sci. Instrum.* **59**, 2544 (1998).
  43. Galli, I. *et al.* Molecular Gas Sensing Below Parts Per Trillion: Radiocarbon-Dioxide Optical Detection. *Phys. Rev. Lett.* **107**, 270802 (2011).
  44. Jousten, K. *et al.* Perspectives for a new realization of the pascal by optical methods. *Metrologia* **54**, S146–S161 (2017).
  45. Bielska, K. *et al.* High-accuracy measurements of the vapor pressure of ice referenced to the triple point. *Geophys. Res. Lett.* **40**, 6303–6307 (2013).
  46. K. Bielska, D.K. Havey, G.E. Scace, D. Lisak, and J. T. H. No Title. *Philos. Trans. R. Soc. A Math. Phys. Eng. Sci* **370**, 2509 (2012).

47. Hodges, J. T. & Lisak, D. Frequency-stabilized cavity ring-down spectrometer for high-sensitivity measurements of water vapor concentration. *Appl. Phys. B* 2006 852 **85**, 375–382 (2006).
48. Bello, I. *Vacuum and Ultravacuum: Physics and Technology*. (CRC Press, 2017).
49. Fremerey, J. K. The spinning rotor gauge. *J. Vac. Sci. Technol. A Vacuum, Surfaces, Film.* **3**, 1715–1720 (1985).
50. Christian, R. The theory of oscillating-vane vacuum gauges. *Vacuum* **16**, 175–178 (1966).
51. Blom, F. R., Bouwstra, S., Elwenspoek, M. & Fluitman, J. H. J. Dependence of the quality factor of micromachined silicon beam resonators on pressure and geometry. *J. Vac. Sci. Technol. B Microelectron. Nanom. Struct. Process. Meas. Phenom.* **10**, 19 (1998).
52. Verbridge, S. S., Ilic, R., Craighead, H. G. & Parpia, J. M. Size and frequency dependent gas damping of nanomechanical resonators. *Appl. Phys. Lett.* **93**, 013101 (2008).
53. Chakram, S., Patil, Y. S., Chang, L. & Vengalattore, M. Dissipation in Ultrahigh Quality Factor SiN Membrane Resonators. *Phys. Rev. Lett.* **112**, 127201 (2014).
54. Norte, R. A., Moura, J. P. & Gröblacher, S. Mechanical Resonators for Quantum Optomechanics Experiments at Room Temperature. *Phys. Rev. Lett.* **116**, 147202 (2016).
55. Tsaturyan, Y., Barg, A., Polzik, E. S. & Schliesser, A. Ultracoherent nanomechanical resonators via soft clamping and dissipation dilution. *Nat. Nanotechnol.* 2017 128 **12**, 776–783 (2017).

56. Matthews, C. *et al.* Mathematical modelling to support traceable dynamic calibration of pressure sensors. *Metrologia* **51**, 326 (2014).
57. Hjelmgren, J. & Sveriges provnings- och forskningsinstitut. *Dynamic measurement of pressure : a literature survey*. (SP Sveriges Provnings- och Forskningsinstitut, 2002).
58. Douglass, K. O. & Olson, D. A. Towards a standard for the dynamic measurement of pressure based on laser absorption spectroscopy. *Metrologia* **53**, S96 (2016).
59. Olson, D., Douglass, K. O. & Ahmed, Z. Precision Spectroscopy to Enable Traceable Dynamic Measurements of Pressure. *Conf. Lasers Electro-Optics (2016), Pap. ATu1J.1* ATu1J.1 (2016) doi:10.1364/CLEO\_AT.2016.ATU1J.1.
60. Hanson, E., Olson, D. A., Liu, H., Ahmed, Z. & Douglass, K. O. Towards traceable transient pressure metrology. *Metrologia* **55**, 275–283 (2018).
61. Moldover, M. R. Can a Pressure Standard be Based on Capacitance Measurements? *J. Res. Natl. Inst. Stand. Technol.* **103**, 167 (1998).
62. Cencek, W. *et al.* Effects of adiabatic, relativistic, and quantum electrodynamics interactions on the pair potential and thermophysical properties of helium. *J. Chem. Phys.* **136**, 224303 (2012).
63. Fischer, J. Low uncertainty Boltzmann constant determinations and the kelvin redefinition. *Philos. Trans. R. Soc. A Math. Phys. Eng. Sci.* **374**, (2016).
64. Puchalski, M., Piszczatowski, K., Komasa, J., Jeziorski, B. & Szalewicz, K. Theoretical determination of the polarizability dispersion and the refractive index of helium. *Phys. Rev. A* **93**, 032515 (2016).
65. Born, M. and Wolf, E. *Principles of Optics, Ch 2*. (Pergamon, 1980).

66. Pendrill, L. R. Refractometry and gas density. *Metrologia* **41**, S40 (2004).
67. Egan, P. F., Stone, J. A., Ricker, J. E. & Hendricks, J. H. Comparison measurements of low-pressure between a laser refractometer and ultrasonic manometer. *Rev. Sci. Instrum.* **87**, 053113 (2016).
68. Egan, P. *et al.* Performance of a dual Fabry – Perot cavity refractometer. *Opt. Lett.* **40**, 3945–3948 (2015).
69. Schmidt, J., Gavioso, R. M., May, E. F. & Moldover, M. R. Polarizability of Helium and Gas Metrology. *Phys. Rev. Lett.* **98**, 254504 (2007).
70. Egan, P. F., Stone, J. A., Ricker, J. E., Hendricks, J. H. & Strouse, G. F. Cell-based refractometer for pascal realization. *Opt. Lett.* **42**, 2944 (2017).
71. Stone, J. *et al.* Picometer Metrology for Precise Measurement of Refractive Index, Pressure, and Temperature. *NCSLI Meas.* **8**, 67–73 (2013).
72. Scherschligt, J. *et al.* Development of a new UHV/XHV pressure standard (cold atom vacuum standard). *Metrologia* **54**, S125–S132 (2017).
73. Madison, K. & Booth, J. Method and device for accurately measuring the incident flux of ambient particles in a high or ultra-high vacuum environment. U.S. Patent US8803072B2 (2014).
74. Fagnan, D. E. *et al.* Observation of quantum diffractive collisions using shallow atomic traps. *Phys. Rev. A* **80**, 022712 (2009).
75. Arpornthip, T., Sackett, C. A. & Hughes, K. J. Vacuum-pressure measurement using a magneto-optical trap. *Phys. Rev. A* **85**, 033420 (2012).
76. Yuan, J.-P. *et al.* Simple, reliable, and nondestructive method for the measurement of vacuum pressure without specialized equipment. *Appl. Opt. Vol. 52, Issue 25*,



pp. 6195-6200 **52**, 6195–6200 (2013).

77. Moore, R. W. G. *et al.* Measurement of vacuum pressure with a magneto-optical trap: A pressure-rise method. *Rev. Sci. Instrum.* **86**, 093108 (2015).
78. Makhalov, V. B., Martiyanov, K. A. & Turlapov, A. V. Primary vacuumeter based on an ultracold gas in a shallow optical dipole trap. *Metrologia* **53**, 1287 (2016).
79. Calder, R., Physics, G. L.-B. J. of A. & 1967, undefined. Reduction of stainless-steel outgassing in ultra-high vacuum. *iopscience.iop.org* **18**, (1967).
80. Rezaie-Serej, S. & Outlaw, R. A. Thermal desorption of CO and H<sub>2</sub> from degassed 304 and 347 stainless steel. *J. Vac. Sci. Technol. A Vacuum, Surfaces, Film.* **12**, 2814 (1998).
81. Ishikawa, Y. & Nemanič, V. An overview of methods to suppress hydrogen outgassing rate from austenitic stainless steel with reference to UHV and EXV. *Vacuum* **69**, 501–512 (2003).
82. Li, M. & Dylla, H. F. Model for the outgassing of water from metal surfaces. *J. Vac. Sci. Technol. A Vacuum, Surfaces, Film.* **11**, 1702–1707 (1993).
83. Sefa, M., Fedchak, J. A. & Scherschligt, J. Investigations of medium-temperature heat treatments to achieve low outgassing rates in stainless steel ultrahigh vacuum chambers. *J. Vac. Sci. Technol. A Vacuum, Surfaces, Film.* **35**, 041601 (2017).
84. K. Jousten, E. *Handbook of Vacuum Technology*. (Wiley-VCH Verlag, 2008).
85. Grant, D. M., Cummings, D. L. & Blackburn, D. A. Hydrogen in 304 steel: Diffusion, permeation and surface reaction. *J. Nucl. Mater.* **149**, 180–191 (1987).
86. Berg, R. F. Hydrogen traps in the outgassing model of a stainless steel vacuum chamber. *J. Vac. Sci. Technol. A Vacuum, Surfaces, Film.* **32**, 031604 (2014).

87. Jousten, K. Dependence of the outgassing rate of a “vacuum fired” 316LN stainless steel chamber on bake-out temperature. *Vacuum* **49**, 359–360 (1998).
88. Yoshimura, N., Hirano, H., Sato, T., Ando, I. & Adachi, S. Outgassing characteristics and microstructure of a “vacuum fired” (1050 °C) stainless steel surface. *J. Vac. Sci. Technol. A Vacuum, Surfaces, Film.* **9**, 2326–2330 (1991).
89. Westerberg, L., Hjärvansson, B., Wallén, E. & Mathewson, A. Hydrogen content and outgassing of air-baked and vacuum-fired stainless steel. *Vacuum* **48**, 771–773 (1997).
90. Marin, P. *et al.* Outgassing performances of an industrial prototype tube for the Virgo antenna. *Elsevier*.
91. Sasaki, Y. T. Reducing SS 304/316 hydrogen outgassing to  $2 \times 10^{-15}$  torr·l/cm<sup>2</sup>·s. *J. Vac. Sci. Technol. A Vacuum, Surfaces, Film.* **25**, 1309 (2007).
92. Park, C. D., Chung, S. M., Liu, X. & Li, Y. Reduction in hydrogen outgassing from stainless steels by a medium-temperature heat treatment. *J. Vac. Sci. Technol. A Vacuum, Surfaces, Film.* **26**, 1166 (2008).
93. Mamun, M. A. A., Elmustafa, A. A., Stutzman, M. L., Adderley, P. A. & Poelker, M. Effect of heat treatments and coatings on the outgassing rate of stainless steel chambers. *J. Vac. Sci. Technol. A Vacuum, Surfaces, Film.* **32**, 021604 (2013).
94. Battes, K., Day, C. & Hauer, V. Outgassing rate measurements of stainless steel and polymers using the difference method. *J. Vac. Sci. Technol. A Vacuum, Surfaces, Film.* **33**, 021603 (2015).
95. Odaka, K., Ishikawa, Y. & Furuse, M. Effect of baking temperature and air exposure on the outgassing rate of type 316L stainless steel. *J. Vac. Sci. Technol. A*

- Vacuum, Surfaces, Film.* **5**, 2902–2906 (1987).
96. Ishikawa, Y., Yoshimura, T., Vacuum, M. A.- & 1996, undefined. Effect of surface oxides on the permeation of deuterium through stainless steel. *Elsevier*.
  97. Nemanič, V. & Šetina, J. Outgassing in thin wall stainless steel cells. *J. Vac. Sci. Technol. A Vacuum, Surfaces, Film.* **17**, 1040–1046 (1999).
  98. Bernardini, M. *et al.* Air bake-out to reduce hydrogen outgassing from stainless steel. *J. Vac. Sci. Technol. A Vacuum, Surfaces, Film.* **16**, 188–193 (1998).
  99. Fedchak, J. A. *et al.* Vacuum furnace for degassing stainless-steel vacuum components. *J. Vac. Sci. Technol. A Vacuum, Surfaces, Film.* **36**, 023201 (2018).
  100. Fedchak, J. A. *et al.* Outgassing rate comparison of seven geometrically similar vacuum chambers of different materials and heat treatments. *J. Vac. Sci. Technol. B* **39**, 024201 (2021).
  101. Battes, K., Day, C. & Hauer, V. Outgassing rate measurements of stainless steel and polymers using the difference method Outgassing in thin wall stainless steel cells Outgassing rate measurements of stainless steel and polymers using the difference method. *J. Vac. Sci. Technol. A J. Vac. Sci. Technol. A J. Vac. Sci. Technol. A* **33**, 21603–1166 (2015).
  102. Young, J. R. Outgassing Characteristics of Stainless Steel and Aluminum with Different Surface Treatments. *J. Vac. Sci. Technol.* **6**, 398–400 (1969).
  103. Chen, J. R., Huang, J. R., Hsiung, G. Y., Wu, T. Y. & Liu, Y. C. Outgassing behavior on aluminum surfaces: Water in vacuum systems. *J. Vac. Sci. Technol. A Vacuum, Surfaces, Film.* **12**,.
  104. Dobrozemsky, R., Menhart, S. & Buchtela, K. Residence times of water molecules

- on stainless steel and aluminum surfaces in vacuum and atmosphere. **25**, 551 (2007).
105. Takeda, M., Kurisu, H., Yamamoto, S. & Nakagawa, H. Hydrogen distribution in titanium materials with low outgassing property. *Vacuum* **84**, 352–356 (2009).
  106. Ishizawa, K., Kurisu, H., Yamamoto, S., Nomura, T. & Murashige, N. Effect of chemical polishing in titanium materials for low outgassing. *J. Phys. Conf. Ser.* **100**, (2008).
  107. Minato, M. & Itoh, Y. Vacuum characteristics of titanium. *J. Vac. Sci. Technol. A Vacuum, Surfaces, Film.* **13**, (1995).
  108. Takeda, M., Kurisu, H., Yamamoto, S., Nakagawa, H. & Ishizawa, K. Hydrogen outgassing mechanism in titanium materials. *Appl. Surf. Sci.* **258**, 1405–1411 (2011).
  109. Dittmann, S., Lindenau, B. E. & Tilford, C. R. The molecular drag gauge as a calibration standard. *J. Vac. Sci. Technol. A Vacuum, Surfaces, Film.* **7**, 3356 (1998).
  110. Fedchak, J. A., Arai, K., Jousten, K., Setina, J. & Yoshida, H. Recommended practices for the use of spinning rotor gauges in inter-laboratory comparisons. *Meas. J. Int. Meas. Confed.* **66**, 176–183 (2015).
  111. Grant, D. M., Cummings, D. L. & Blackburn, D. A. Hydrogen in 316 steel — diffusion, permeation and surface reaction. *J. Nucl. Mater.* **152**, 139–145 (1988).
  112. Kurisu, H., Ishizawa, K., Yamamoto, S., Hesaka, M. & Saito, Y. Application of titanium materials to vacuum chambers and components. *J. Phys. Conf. Ser.* **100**, 092002 (2008).

113. Foot, C. J. Atomic Physics. in 178–217 (Oxford U.P., 2005).
114. Bali, S., O'hara, K. M., Gehm, M. E., Granade, S. R. & Thomas, J. E. Quantum-diffractive background gas collisions in atom-trap heating and loss. **60**, (1999).
115. Eckel, S. *et al.* Challenges to miniaturizing cold atom technology for deployable vacuum metrology. *Metrologia* **55**, S182–S193 (2018).
116. Zhu, C., Dalgarno, A. & Derevianko, A. van der Waals interactions between molecular hydrogen and alkali-metal atoms. *Phys. Rev. A* **65**, 034708 (2002).
117. Jiang, J., Mitroy, J., Cheng, Y. & Bromley, M. W. J. Effective oscillator strength distributions of spherically symmetric atoms for calculating polarizabilities and long-range atom–atom interactions. *At. Data Nucl. Data Tables* **101**, 158–186 (2015).
118. Tao, J., Perdew, J. P. & Ruzsinszky, A. Accurate van der Waals coefficients from density functional theory. *Proc. Natl. Acad. Sci. U. S. A.* **109**, 18–21 (2012).
119. Petrich, W., Anderson, M. H., Ensher, J. R. & Cornell, E. A. Stable, Tightly Confining Magnetic Trap for Evaporative Cooling of Neutral Atoms. *Phys. Rev. Lett.* **74**, 3352 (1995).
120. Alcock, C. B., Itkin, V. P. & Horrigan, M. K. Vapour pressure equations for the metallic elements: 298-2500k. *Can. Metall. Q.* **23**, 309–313 (1984).
121. Migdall, A. L., Prodan, J. V., Phillips, W. D., Bergeman, T. H. & Metcalf, H. J. First Observation of Magnetically Trapped Neutral Atoms. **54**, (1985).
122. Pritchard, D. E. Cooling Neutral Atoms in a Magnetic Trap for Precision Spectroscopy.
123. Bagnato, V. S. *et al.* Continuous Stopping and Trapping of Neutral Atoms. **58**,.

124. Schmidt, P. O. *et al.* Continuous loading of cold atoms into a Ioffe–Pritchard magnetic trap. *J. Opt. B Quantum Semiclassical Opt.* **5**, S170 (2003).
125. Siegel, J. L., Barker, D. S., Fedchak, J. A., Scherschligt, J. & Eckel, S. A Bitter-type electromagnet for complex atomic trapping and manipulation. *Rev. Sci. Instrum.* **92**, (2021).
126. Barker, D. S., Restelli, A., Fedchak, J. A., Scherschligt, J. & Eckel, S. A radiofrequency voltage-controlled current source for quantum spin manipulation. *Rev. Sci. Instrum.* **91**, (2020).
127. Norrgard, E. B. *et al.* Note: A 3D-printed alkali metal dispenser. *Rev. Sci. Instrum.* **89**, 056101 (2018).
128. Su, S. H., Hou, C. C., Shieh, R. S. & Yokoyama, M. Enhancing efficiency of organic light-emitting diodes using lithium-doped electron transport layer. *Jpn. J. Appl. Phys.* **47**, 3193–3195 (2008).
129. Abramova, I., Aleksandrov, E., Bonch-Bruevich, A. & Khromov, V. Photostimulated desorption of metal atoms from surfaces of transparent insulators. *Sov. J. Exp. Theor. Phys. Lett.* **39**, 203 (1984).
130. Gozzini, A. *et al.* Light-induced ejection of alkali atoms in polysiloxane coated cells. *Nuovo Cim. D* **15**, 709–722 (1993).
131. Barker, D. S., Norrgard, E. B., Scherschligt, J., Fedchak, J. A. & Eckel, S. Light-induced atomic desorption of lithium. *Phys. Rev. A* **98**, 1–6 (2018).
132. Makrides, C. *et al.* Elastic rate coefficients for Li+ H<sub>2</sub> collisions in the calibration of a cold-atom vacuum standard. *Phys. Rev. A* **99**, (2019).
133. Makrides, C. *et al.* Collisions of room-temperature helium with ultracold lithium

- and the van der Waals bound state of HeLi. *Phys. Rev. A* **101**, 12702 (2020).
134. Niewiński, M., Szwemin, P., Calcatelli, A. & Bergoglio, M. Evaluation of the conductance of the orifice of the new CNR-IMGC dynamic expander. *Metrologia* **36**, 555–559 (1999).
  135. Poulter, K. F. The calibration of vacuum gauges. *J. Phys. E Sci. Instrum.* **10**, (1977).
  136. Edwards, J. G. & Gilles, P. W. Effusion from Spherical Orifices. I. Transmission by Molecular Flow. *J. Chem. Phys* **44**, 4426 (1966).
  137. Eckel, S. *et al.* A constant pressure flowmeter for extremely high vacuum. *Metrologia* **59**, 045014 (2022).
  138. Hicks, W. T. Cite as. *Bismuth J. Chem. Phys.* **38**, 15 (1963).
  139. Anderson, B. P. & Kasevich, M. A. Loading a vapor-cell magneto-optic trap using light-induced atom desorption. doi:10.1103/PhysRevA.63.023404.
  140. Telles, G., Ishikawa, T., Gibbs, M. & Raman, C. Light-induced atomic desorption for loading a sodium magneto-optical trap. *Phys. Rev. A* **81**, 32710 (2010).
  141. Nshii, C. C. *et al.* A surface-patterned chip as a strong source of ultracold atoms for quantum technologies. *Nat. Nanotechnol.* **8**, 321–324 (2013).
  142. Paul Eckel, S. *et al.* Uniaxial counter-propagating monolaser atom trap. (2022).
  143. Hoffmann, D., Bali, S. & Walker, T. Trap-depth measurements using ultracold collisions. **54**, 54 (1996).
  144. Dongen, J. Van *et al.* Trap-depth determination from residual gas collisions. *Phys. Rev. A* **84**, 22708 (2011).
  145. Ritchie, N., Abraham, E., & Hulet, R., Trap loss collisions of <sup>7</sup>Li: The role of trap

- depth. *Laser Phys*, 4, **5**, 1066 (1994).
146. Makrides, C. *et al.* Erratum: Elastic rate coefficients for Li+ H<sub>2</sub> collisions in the calibration of a cold-atom vacuum standard (Physical Review A (2019) 99 (042704) DOI: 10.1103/PhysRevA.99.042704). *Phys. Rev. A* **105**, 039903 (2022).
147. Ehinger, L. H. *et al.* Comparison of two multiplexed portable cold-atom vacuum standards. *AVS Quantum Sci.* **4**, 034403 (2022).